Technical University of Denmark

DTU

Extending the Versatility of Chemical Microchips by Improved Integration of Functional Elements

Snakenborg, Detlef; Kutter, Jörg Peter; Hübner, Jörg; Klank, Henning

[Link back to DTU Orbit](#)

DTU Library
Technical Information Center of Denmark

Extending the versatility of bio-chemical microchips by improved integration of functional elements

Detlef Snakenborg

November 1, 2006

Abstract

The idea of lab-on-a-chip systems is to integrate all necessary functions to perform bio-chemical analyses onto a single device. After almost two decades of research, however, the number of available platforms that unite the key functions - *microfluidic handling*, *bio-chemical processes* and *detection* - is negligible. It is widely accepted that microtechnology has shown its feasibility in the field of biology and chemistry. The circumstance that research mainly focuses on single functions and phenomena, however, results in incompatibilities of materials and fabrication processes and prevents a higher degree of integration. Further, a trend towards single-use devices is evident necessitating economic production, i.e., polymer mass fabrication. Consequently, the development of new approaches, which can be realized using these mass fabrication methods rather than relying on conventional MEMS technology is required.

This work presents the effort to develop components that fulfil all requirements to establish a complete μTAS platform. New elements were developed and new fabrication methods were investigated.

A novel check valve, that, apart from a superior diodicity, also has tunable properties, was invented. Furthermore, a micropump was realized utilizing these check valves and offering good performance. Additionally, simplifying fluidic handling on the chip level, a new active valve principle was developed, showing promising results.

New methods to fabricate polymer-based optical waveguides allow mass production in addition to simple integration and ensure furthermore excellent transmission of the waveguides in the VIS range. Combined with integrated optical components, detection on chips was optimized.

All components were designed considering potential fabrication methods. The option to be able to produce devices using economic fabrication was accommodated as well as the possibility for rapid prototyping. Various techniques, e.g. micromilling or molding, were applied and investigated. Bonding methods were compared, characterized and optimized to achieve easy assembly. Finally, newly developed fluidic interconnections represent a simple method to package microfluidic devices.

The achieved results allow to combine the individual components and offer a highly flexible toolbox for microfluidic applications that shows the potential for development of stand-alone lab-on-a-chip systems.

Resumé (in Danish)

Ideen bag Lab-on-a-chip systemer er at integrere alle nødvendige funktioner for udførelsen af en komplet biokemisk analyse i et enkelt apparat. Efter næsten to årtiers forskning er antallet af tilgængelige teknologier der kombinerer de forskellige kerne funktioner, såsom mikrofluid håndtering, processering og detektion, stadig meget begrænset. Det er alment kendt at mikroteknologi har vist sin berettigelse inden for biologi og kemi, men da forskningen hovedsageligt fokuserer på enkelte funktioner eller fænomener, løses problemer med inkompatible materiale- og fabrikationsprocesser ikke, hvilket forhindrer en højere grad af integration. Derudover er der et stort behov for engangsanalyser, hvilket nødvendiggør udvikling af billige produktionsteknikker, såsom massefremstilling i plastik. Derfor er det nødvendigt at udvikle nye massefremstillingsmetoder, som alternativ til den traditionelle MEMS fabrikationsteknologi.

Denne rapport beskriver bestræbelserne på at udvikle komponenter der opfylder kravene til en komplet μTAS platform. Nye elementer blev udviklet og nye fremstillingsmetoder blev undersøgt.

En ny form for variabel passiv ventil med meget gode diode egenskaber blev udviklet og disse blev brugt i en effektiv mikropumpe. Derudover blev et nyt aktivt ventil princip opfundet, som baseres på en simplificering af den mikrofluide væskehåndtering på chip niveau.

Udvikling af alternative massefabrikationsmetoder til integrerede planare bølgeleder som er transparente i hele det visuelle spektrum er beskrevet. Disse blev kombineret med andre optiske komponenter for at muliggøre detektion på chippen.

Alle komponenter blev designet med massefremstilling og hurtig prototypefremstilling for øje, for at kunne holde komponentprisen og udviklingsomkostningerne nede. Diverse teknikker, såsom mikrofræsning og støbning blev ligeledes undersøgt og forskellige bondemetoder blev sammenlignet for at opnå en effektiv chip produktion. Derudover blev der udviklet en metode til effektivt at forbinde chippen til omverdenen ved hjælp af små rør brugt som væske tilslutninger.

De opnåede resultater kan ses som en værktøjskasse der gør os I stand til at kombinere de forskellige delkomponenter for at realisere et funktionsdygtigt lab-on-a-chip system.

Contents

Chapter 1

Introduction

1.1 Motivation

Since the idea of an integrated chemical laboratory was created in the early 1990s [1], research groups have put a lot of effort into the attempt to scale down a bio-chemical laboratory to the size of a chip. Motivated by the fast growing computer chip industry, which gained success from repeated miniaturization, the aim was to design a device that included all necessary components to perform bio-chemical analyses. While in conventional laboratories specialized equipment is used to perform single analysis steps, lap-on-a-chip systems accomplish all these functions in a small portable unit. Analysis can be performed close to the location where it is required. Hence, transportation of samples to the laboratory is not necessary anymore. Thus, micro-total-analysis-systems (μTAS) bring detection close to the customer and render specialized equipment or personnel redundant. Another aspect of miniaturization is the reduction of sample and reagent volume, which, on the one hand, increases the efficiency, and, on the other hand, also reduces costs. Portability facilitates the possibility of continuous monitoring. Offering a wide variety of potential applications these systems can, for instance, remain in the environment in a self-sustaining manner to log environmental data, or can be worn attached to the human body while monitoring medical parameters.

Now, almost two decades later, micro-total-analysis-systems that fulfill all these requirements are far from being standard devices. In an ongoing process, research groups concentrate either on the development of individual components for lab-on-a-chip systems, such as micropumps [2,3], valves [4], separation mechanisms [5] or miniaturized optical components [6] or on the advancement of fabrication technologies [7–9]. The many principles invoked and the different technologies applied, however, have so far prevented the components from being combined and a fully integrated platform from being developed. The reason for that can, on the one hand, be seen in the

incompatibility of fabrication techniques or materials. Instead, a trend towards hybrid devices became apparent where individual functional elements were connected instead of integrating them into a single chip. On the other hand, however, high integration often increased complexity, which can lead to failure and increases the costs. A balance between the necessary grade of integration and its benefits compared to a less integrated devices has to be found.

Although a completely integrated platform is still missing, many phenomena have been investigated and a range of principles were developed applying the individual components to actually perform analyses on the chip level. In various research branches, as, for instance, in cellomics [10], proteomics [11, 12], biochemical analysis [13, 14] or in chemical microreactors [15], miniaturized devices offer superiority in comparison to conventional analytical methods and equipment. These modules, however, do not yet fully realize the idea of small portable devices, but, in fact, still require a surrounding laboratory environment for connection, feed and control purposes.

1.2 The Aim of this Work

The aim of this work is to provide the necessary components to realize an integrated micro total analysis system. A μTAS basically requires four functions, namely sample pretreatment, fluidic handling, detection and electronic control [16]. Since fluidic handling and detection can be seen as core functions and usually generate the most challenges this work focuses on these two.

Developing isolated elements that fulfill single functions and combining them in the next iteration, is certainly a good strategy. However, the goal is not to build a hybrid device, with several discrete elements connected and working together next to each other, but instead to develop a design and fabrication rationale towards monolithic systems. Therefore, it is advantageous to develop various principles using the same fabrication methods and to decide in good time, which fabrication methods can be combined and are compatible.

The demand for single-use devices in the life sciences further necessitates economic production and bio-compatibility of materials and devices. Conventional techniques [17, 18], adapted from the area of micro-electro-mechanical-systems (MEMS), are thus more and more substituted by polymer microfabrication [19–21], which provides the possibility of mass production. Once a design is determined, it can be reproduced in large numbers, which, next to cost reduction, also makes parallel or high throughput analyses possible. Furthermore, a number of polymer machining techniques can be employed as rapid prototyping methods, which allow fast design changes

at low costs, a feature especially interesting in the research and development field. However, due to the different properties MEMS materials and polymers possess, it is not possible to directly transfer neither commonly used principles nor fabrication methods. In fact, novel concepts have to be developed to achieve the required functionality and newly invented processes must be applied for fabrication. Since the high precision of cleanroom processes is not available using conventional polymer machining, the design and fabrication of microdevices that are produced with these technologies while still offering the required capabilities represent quite a challenge.

Optical detection methods are widely used in chemical analysis systems. The development of integrated optical elements based on the use of polymer fabrication technologies is one issue that is highlighted in this thesis. Furthermore, the challenges of integrated optical elements, such as high coupling or propagation losses, have to be addressed properly.

Fluidic handling includes passive elements such as microfluidic channels or check valves, and active elements as, for instance, active valves and micropumps. To establish a monolithically integrated device, all these components have to be developed with respect to compatibility and the least complex design in order to alleviate the combination of the individual elements.

Another aspect of microfluidic systems is packaging, such as fluidic interconnections that allow to interface the chip with the outside world. Although packaging is not directly related to integration, it is an important element on the path to a complete system and, hence, has to be considered.

1.3 Structure of this Thesis

The methods and components developed in this work range from polymer fabrication, such as bonding, casting or micromilling, over optical waveguiding structures and fluidic interconnections to active components, such as microvalves and pumps. The great individuality of the covered research fields requires dedicated chapters, which each contain an introduction with a literature overview, a part that describes the fabrication, and a result section. In order to summarize and discuss future approaches, a conclusion and an outlook are added to each chapter. It has to be noted, however, that all chapters have to be seen as part of the overall striving for integrateability and simplified fabrication.

At the start of this project, the main effort was put into the optimization of an ammonia detection device with integrated polymer-based waveguides. Here, the focus was the integration of optical elements to optimize the incoupling of the light into the on-chip absorbance cell, as described in Ch. (5). Further progress was made with the development of a novel fabrication method for polymer-based optical waveguides. Here, another fo-

cus was put on the extended wavelength region where the waveguides were transparent, as shown in Ch. (6).

The development of fluidic handling components represents another aspect of this work. Beginning with the characterization of a novel passive valve principle (Ch. (2)), this valve was then applied to a micropump design (Ch. (3)). The issues within microfluidics were completed with the presentation of an active valve design, whose working principle was proven (Ch. (4)).

The need for packaging and interconnections was present during the entire project and the development and optimization of a tube connector (Ch. (8)) as well as investigations on bonding methods (Ch. (7)) were thus conducted in parallel.

During the last year of the work, a newly started project was joined aiming to analyze protein structures using a combination of microfluidics and small angle x-ray scattering methods, as mentioned in Ch. (9). This project allowed to apply various techniques developed during the earlier part of the PhD period and also represents an application that greatly benefits from integration.

Chapter 2

Passive Microvalves

2.1 Introduction

The purpose of a check valve is to allow a fluid to flow in one direction (forward direction) while preventing its flow in the backward direction. This rectifying feature, that is not unlike a diode in electronics, can directly be used in microfluidic channels to handle liquids.

Already since the early days of microsystem engineering, microfluidics played a major role in this field. Controlling the flow in fluidic microsystems is one of the main issues and micropumps and microvalves are its key elements [4, 22].

The demand for single-use devices, for instance in the life sciences, is increasing. However, microfluidic components fabricated with conventional MEMS technologies often require multiple step fabrication processes in cleanroom environments. Therefore, microvalve components as essential elements of these devices have so far often represented a barrier, not only from the technological but also from the economical point of view.

Although many different principles have been utilized to develop microvalves, almost all of these realizations have in common that they have been developed isolated from other functional elements focusing just on the valve issue or on the valve as a component on a micropump. Very rarely has the integrational aspect been highlighted. In lab-on-a-chip devices, where various functions are combined, it is important, however, to consider the compatibility of the individual fabrication methods and materials.

In this work, we present a novel valve approach that allows easy integration and compatibility with other components used in microfluidic devices. The principle can be applied to a great choice of different materials and requires only a few fabrication steps. Additionally, conventional polymer fabrication methods can be used and ensure fast and economical production. The developed valve further allows the combination of a check valve's rectifying properties with the possibility to actively control the flow rate in

the forward (open) direction.

2.2 State of the Art

It is far beyond the scope of this work to give a complete overview of all existing valve principles applied to microtechnology. A brief comparison to existing devices, however, is helpful to understand the purpose of the approach presented in this work. A recent review on microvalves was published by Kwang and Chong [4].

The number of journal articles on microvalves has almost constantly been increasing since the early 1990, as Fig. (2.1) shows.
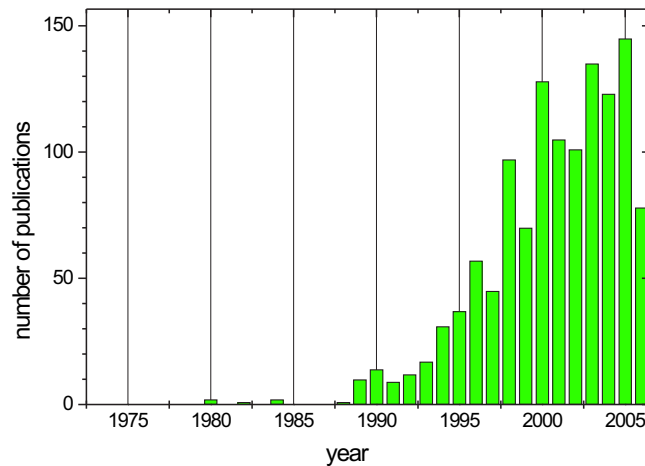
Figure 2.1: The number of publications is the sum of hits on "microvalve" and "microvalves" (article database service, Technical Knowledge Center of Denmark). The first mentioning of a microvalve was found for the year 1979. The rightmost column represents the number of papers published in 2006 until August.

Microvalves can be divided into passive and active microvalves whereof the latter will be discussed in Ch. (4). A further common division of passive microvalves is to group them into valves containing mechanical and non mechanical parts [4].

A different way to classify microvalves is according to their fabrication methods and the materials they are fabricated in. As mentioned above, a large number of microvalves were developed using MEMS technologies. Due to the thin film capabilities of these technologies, a common approach was to fabricate membrane or flap valves, as for instance presented in [23–25].

Although considerable efforts have been made to establish polymers instead of silicon or glass, the fabrication methods were still mainly dependent on cleanroom processes [26–28]. Miniaturizing valve principles from the macro world led for example to micro ball valves [29], and variations of this principle that use mobile inline structures [30, 31]. Alternative fabrication methods, such as molding, casting and the use of adhesives, were reported in [32–34]. While the use of elastomer membranes as functional elements were applied to active valves [35, 36] (see Ch. (4) for further details) no work could be found that utilizes elastomers in check valves.

2.3 Design and fabrication

The principle of the valve is depicted in Fig. (4.1). Between two rigid substrates (PMMA) an elastomer membrane (PDMS) is clamped. The membrane is provided with an incision (without removing material) using a custom-made tool. This slit is centered over a cavity, which is fabricated into the lower substrate. Applying a pressure from the top allows the membrane to expand into the cavity, which results in an opening of the incision (Fig. (4.1)a). The geometry of the upper substrate prevents the membrane to expand if pressure is applied from the bottom and therefore inhibits flow in the other direction (Fig. (4.1)b). To support this effect, the fluidic through-hole in the upper structure is moved off-center with respect to the slit.
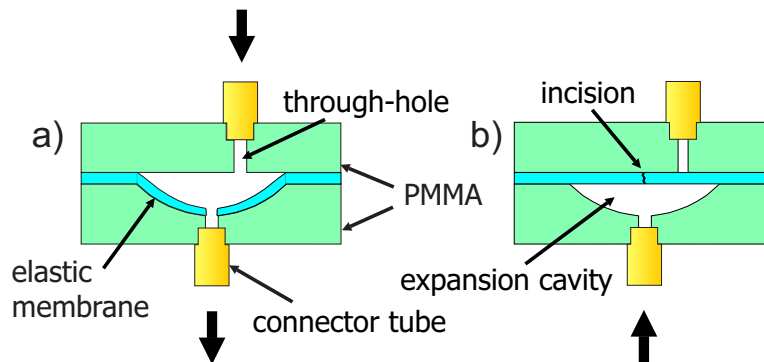
Figure 2.2: Working principle of the valve: an elastomer membrane is clamped between two rigid polymer substrates. A cavity in the bottom substrate allows the membrane to deflect, which results in an expansion of the slit (a). The off-center through-hole in the top substrate prevents the membrane to deflect if a pressure is applied from the bottom (b).

As mentioned above, the valve consists of an elastic membrane that is embedded between two polymer substrates. In this work, as substrate material polymethylmethacrylate (PMMA) was used, which was structured

using micromilling and -drilling.

The expansion cavity was fabricated by milling perpendicularly $200\,\mu$m into the material using a ball-end milling tool. The diameter of the achieved cavity was $800\,\mu$m. The through-holes in the center of the cavity and in the top substrate were drilled with a $100\,\mu$m drill-bit. The connection holes in both substrates had a diameter of $800\,\mu$m and were also drilled. Thin-wall metal (OD $900\,\mu$m) tubes were pressed into the connector holes and ensured sealing without support of any adhesive.

The valve membranes were fabricated by spin-coating PDMS (Sylgaard 184, Dow Corning) onto PMMA slides and curing them for two hours at 60°C. In this work, membranes with thicknesses between 40 and $70\,\mu$m were used, that were realized following the pre-established speed-thickness relationship shown in Fig. (2.3).
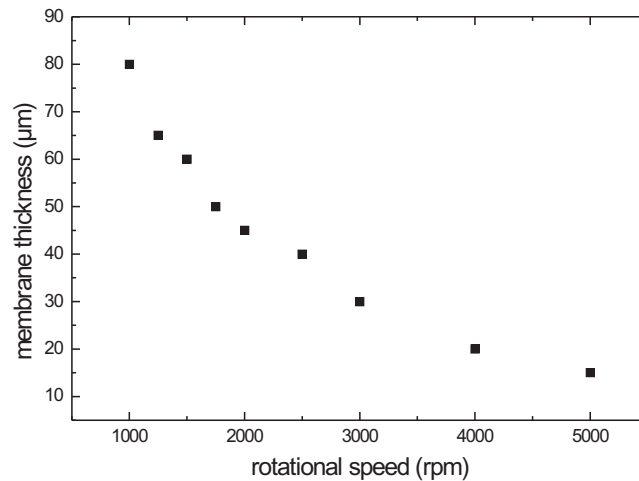
Figure 2.3: The graph shows the membrane thickness that is achieved at different spinning speeds.

A custom-made tool was used to create the incision. The tool consisted of a short piece of spring wire cut from a spring that was sharpened at one end (see Fig. (2.4)). The wire was fixed by simply sticking it into a short teflon rod with the not grinded end. Three different tools with diameters between 250 and $800\,\mu$m were fabricated to produce different slit lengths. The teflon rod was then fit into a collet and attached to the milling machine. Placing the PMMA slide with the cured PDMS layer onto the x-y stage of the milling machine the tip of the tool was aligned to the PDMS surface. With a fixed spindle (to prevent rotation) the tip was moved down a defined distance along the z-axis, according to the thickness of the PDMS layer.
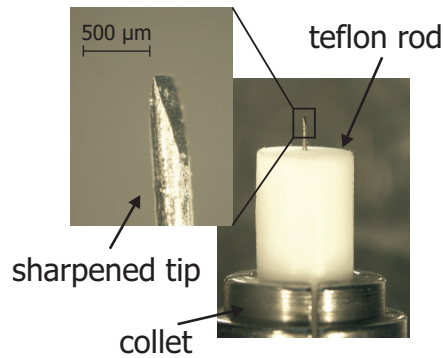
Figure 2.4: The picture shows the tip of a custom-made 250μm stencil tool to fabricate the slit. As material spring wire was cut from a spring and grinded to achieve a sharp tip. The wire was then fixed by simply sticking it into a teflon rod that fit into a milling-tool collet.
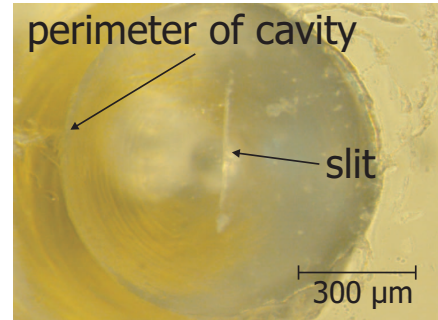
Figure 2.5: The membrane was placed onto the structured substrate centering the incision to the cavity's perimeter. A soap-water solution was used to wet the the contact area to ease the alignment procedure. After evaporation of the water, the membranes stuck to the PMMA, which prevented unintended displacement.

This method ensured reproducible slit geometries and allowed furthermore an automatic slit fabrication.

Subsequently, a scalpel was used to manually cut around the slit to obtain membrane pieces with sizes of $\approx 7\,\text{mm} \times 7\,\text{mm}$. The membranes were then placed onto the structured PMMA plate that contained the expansion cavity centering the slit with respect to the cavity's perimeter using a microscope for optical inspection. To allow easy positioning of the PDMS the surface of the valve seat was wetted with a drop of soap-water. After evaporation of the soap-water the membrane stuck to the PMMA surface and allowed movement of the valve without changing the position of the membrane.

2.4 Theory

A microvalve for integration into bio-chemical microsystems should be small in size, have a small dead volume and a good diodicity. One parameter to characterize a passive valve is its opening or critical pressure, which is defined by the pressure that is needed to establish a flow through the valve.

In the case of the valve presented here, its membrane has to expand to establish a flow through the incision. The membrane's deflection therefore has a major impact on the flow. Based on the theory of thin plates, the correlation between the applied pressure and the center deflection d_{center} of

a circular thin membrane is [37]:

$$d_{center} = 0.662 r_m \sqrt[3]{\frac{pr_m}{Et_m}}. \tag{2.1}$$

with p the applied pressure, r_m the radius and t_m the thickness of the membrane and E Young's modulus. Eq. (2.1) is valid for large deflections.

If the deflection becomes larger than approximately half the membrane thickness, strain occurs inside the membrane and the so-called direct stress cannot be ignored [37]. The incision in the valves's membrane, however, prevents this direct stress to a certain extent. Hence, the equation can only give an estimation of the real deflection.
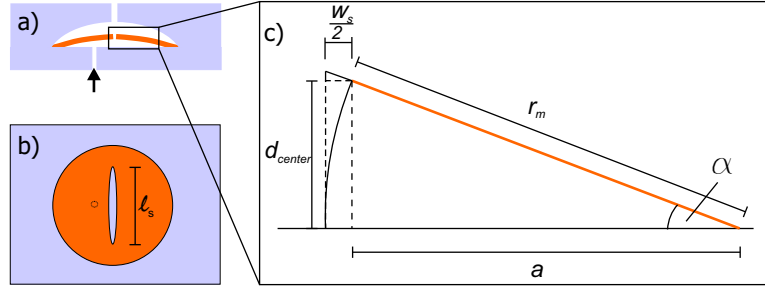
Figure 2.6: The center slit width is obtained by applying simple geometric relations.

The expansion of the membrane results in an opening of the incision. Fig. (2.6)a and Fig. (2.6)b show a cross-sectional and top view sketch of the opened valve. To determine the maximum width of the slit a linear deflection of the membrane was assumed, as sketched in Fig. (2.6)c. The center slit width w_s can then be derived from the deflection d_{center} by simple geometric relations:

$$w = r_m - a = r_m - \sqrt{r_m^2 - d_{center}^2} \tag{2.2}$$

with r_m the radius of the membrane and a as displayed in Fig. (2.6)c.

To estimate the fluidic resistance of the slit another simplification has been made: a rectangular geometry was assumed, as depicted in Fig. (2.7). The fluidic resistance for a rectangular channel profile is

$$R_{fl} = \frac{12\eta t_m}{l_s w_s^3}, \tag{2.3}$$

with η the dynamic viscosity of water, l_s the slit length and w_s the slit width.
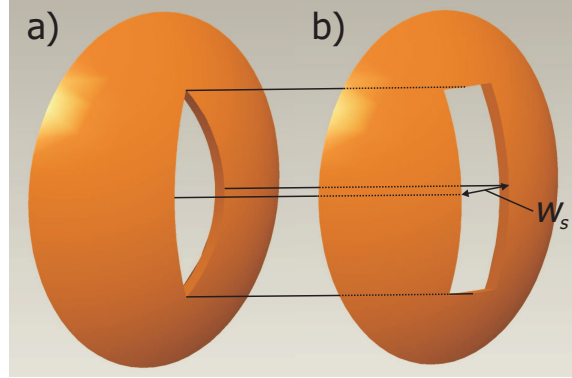
Figure 2.7: The real shape of the slit was transformed to a rectangular geometry with the slit's length and width as side lengths.

The flow rate Q can then be obtained by:

$$Q = \frac{p}{R_{fl}} = \frac{p l_s w_s^3}{12 \eta t_m} \tag{2.4}$$

To estimate the error that occurs assuming a rectangular slit geometry, the difference in fluidic resistance R_{fl} of the two forms were determined. Formula (2) of the Tas *et al.* paper [38] is used as basis and is here repeated as

$$R = \frac{2 f \mathrm{Re} L \mu}{D_\mathrm{h}^2 A}, \tag{2.5}$$

where f is the Fanning friction factor, L is channel length, μ the viscosity of the liquid, D_h is the hydrodynamic diameter and A the cross sectional area.

The ratio between two forms is given by

$$\frac{R_\mathrm{m}}{Rr} = \frac{D_\mathrm{r}^2 A_\mathrm{r}}{D_\mathrm{m}^2 A_\mathrm{m}}, \tag{2.6}$$

where R_m is for the rectangular slit form and Rr signifies the rounded slit form. The general hydraulic diameter D_h is given by

$$D_\mathrm{h} = \frac{4A}{U}, \tag{2.7}$$

where U is the wetted perimeter. Therefore we find the ratio as

$$\frac{R_\mathrm{m}}{Rr} = \frac{A_\mathrm{r}^3 U_\mathrm{m}^2}{A_\mathrm{m}^3 U_\mathrm{r}^2}, \tag{2.8}$$

To find the perimeter and the area for the rounded form, some arithmetic is necessary, as described in the next section.

2.4.1   Rounded Form

The rounded form can be calculated with a circle segment and a right angle triangle to

$$r = \frac{1}{4}(w + \frac{l^2}{w}) \tag{2.9}$$

with r in mm.

Half the opening angle $\alpha/2$ can be calculated from the right triangle as

$$\sin\frac{\alpha}{2} = \frac{2}{\frac{w}{l} + \frac{l}{w}}. \tag{2.10}$$

The segment of the circle can be used to calculate half the cross sectional area and is given by

$$A = r^2(x - \sin x), \tag{2.11}$$

where x is the opening angle in rad and r is from Eq. (2.9).

The wetted perimeter U_r is calculated from the arc and is

$$U_r = 2rx. \tag{2.12}$$

2.4.2   Ratio

To estimate the error depending on the slit geometry, the applied pressures were used, ranging between $p = 1.3$ and $7.4\,\text{kPa}$. From these pressure differences we calculated the corresponding large deflections (Eq. (2.1)) d_s and then plotted the ratio in dependence on the deflection as seen in Fig. (2.8). The figure shows, that the fluidic resistance for the rounded slit form is about 3 times larger than for the rectangular slit form.

2.4.3   Influence of Stress

The novelty compared to common check valves is the use of an elastic material as membrane. Clamping this membrane between two rigid substrates leads to deformation of the membrane, which influences its deflection behavior and therefore the fluidic resistance of the valve.

Applying a stress σ to a membrane with a thickness t_m, as depicted in Fig. (2.9)a results in negative normal strain ε. Stress and normal strain are related by:

$$-\varepsilon = \frac{\Delta t_m}{t_m} = \frac{\sigma}{E}. \tag{2.13}$$

Due to the incompressibility of the elastomer, the decrease of the thickness comes along with an increase of the width of the membrane, the lateral strain ε_l.
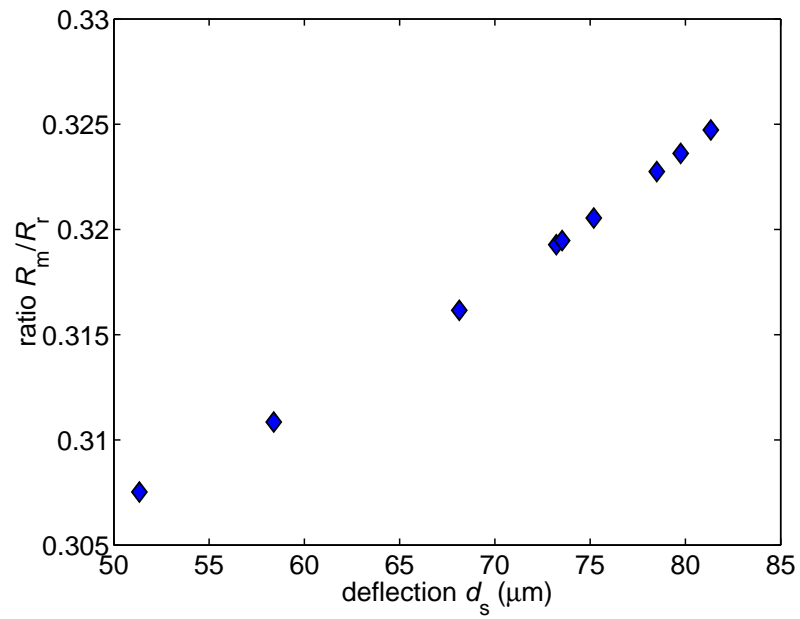
Figure 2.8: The graph shows the ratio of the fluidic resistances, when the membrane is deflected with actual measured pressure differences. The made error, when using the rectangular slit form is $\approx 30\,\%$, compared to the rounded slit form. The opening angle was $\alpha = 10.9\,°$ and the area was $A = 0.0039\,\text{mm}^2$, both for the largest deflection.

(Normal) strain and lateral strain are related by

$$\varepsilon_l = -\nu\varepsilon, \tag{2.14}$$

with ν Poisson's ratio.

Applying the stress locally, e.g. using an annular load as shown in Fig. (2.9)b, results in bulging of the membrane. Thus, reduction of the membrane thickness at the area of applied stress not only increases the membrane width (lateral strain) but also its thickness in the center of the ring load (positive normal strain). As mentioned above, the membrane thickness has a great impact on the pressure that is needed to deflect the membrane. Hence, it is necessary to consider the force that is used to clamp the membrane between the two layers. However, more importantly, the applied stress can be used to actively control the behavior of the membrane.
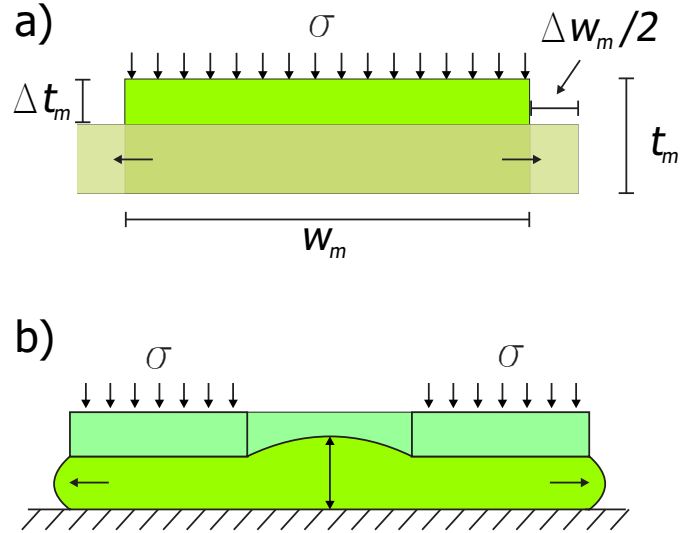
Figure 2.9: a) a uniform load is applied to the elastic membrane and resulting in negative normal strain (reduction of thickness) and lateral strain (increase of width). b) an annular load, on the other hand, results in bulging or positive normal strain in the center of the ring in addition to the lateral strain.

2.5 Experiments

To open the valve and enable flow, a certain pressure is required. The constriction of the flow, the opening pressure and, if open, the valve's resistance in the forward direction should be minimized. On the other hand, flow in the backward direction should be prevented. In this section, the influence of

the membrane thickness, the slit length and the applied stress on the opening pressure are investigated. Additionally, the influence of the slit length and the eccentricity on the backward flow is examined.

To determine the valve's opening pressure, the externally applied pressure was increased until a flow could be measured. However, to avoid influences of the physical work the pressure performs on the membrane, i.e. by deflecting it, the pressure had to be increased gradually and was kept constant during a short interval. An automated setup was built, schematically shown in Fig. (2.10), to be able to characterize a large number of valves under repeatable conditions.
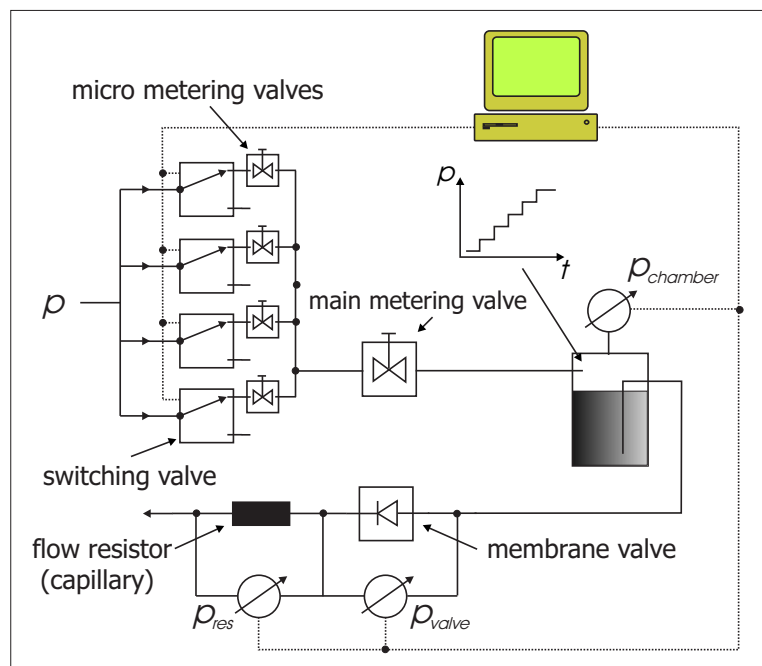
Figure 2.10: Schematic of the measurement setup: the pressure in the chamber can be adjusted using the micro metering valves. Variation of the valve apertures in combination with computer controlled switching valves results in 16 different pressures (as sketched in the inserted p-t graph) and thereby 16 different flow rates in the fluidic system. The flow through both the membrane valve and the fluidic resistor generates a pressure drop that is measured and stored in a computer.

To achieve different pressures, metering valves were adjusted individually, which resulted in different resistances. Four computer controlled switching valves that each were connected in series with the metering valves, allowed to combine various resistances and to generate 16 different pressures at the inlet of a main metering valve. To determine the opening pressure accurately, the individual pressure steps were chosen to be small. The main

metering valve, which was connected to a pressurizable chamber, additionally enabled fine adjustment of the total pressure range. Due to the high impact that the variation of all these parameters has on the opening pressure, the suitable pressure range had to be obtained for every single membrane valve before the measurements. This was done by manually adjusting the main metering valve to a point where a flow just could be detected (at highest resistance of the four metering valves). Then, the main metering valve was closed cautiously until the flow stopped. Starting the measurement increased the pressure gradually by controlled opening of a combination of switching valves.

Generating a pressure in the chamber, the liquid inside the chamber was pushed into the tube connected to the microvalve. The pressure drop across the valve was determined using a differential pressure gauge. Once the valve opens, the liquid flows through a capillary whose resistance could be calculated from its defined inner diameter and length. By measuring the pressure drop p_{res} across the resistor $R_{fluidic}$ it was possible to determine the flow-rate Q:

$$Q = \frac{p_{res}}{R_{fluidic}}. \tag{2.15}$$

As resistors, two different capillaries were used that had a hydraulic resistance of $1.369 \ 10^{14} \ \mathrm{Pa \cdot s \cdot m^{-3}}$ and $1.1131 \ 10^{13} \ \mathrm{Pa \cdot s \cdot m^{-3}}$, respectively. In combination with a second differential pressure sensor it was possible to measure flow-rates as low as $0.05 \ \mu\mathrm{l/s}$ with an accuracy better than 10% and $0.005 \ \mu\mathrm{l/s}$ with an accuracy of 20% (determination of accuracy, see App. (A.1)). For monitoring purposes, the pressure inside the chamber was measured additionally. Since the liquid was flowing into ambient pressure the pressure in the chamber had to be equal to the sum of both measured pressure drops across valve and resistor. This can be used as a fail-check since a deviation in this case indicates a failure of the system, e.g. air bubbles.

Various membrane thicknesses were tested with the above described setup. A further examined parameter was the eccentricity of the through-hole with respect to the slit. Since the membrane is prevented to deflect in the backward direction and flow is inhibited due to the off-centered through-hole, the eccentricity is expected to have a great influence on the backward flow. While the eccentricity was kept constant at $100 \ \mu\mathrm{m}$ for the variation of the membrane thicknesses, it was varied between 50 and $200 \ \mu\mathrm{m}$ for estimating its influence on the backward flow.

To obtain information about the impact of the mechanical stress applied to the membrane on the characteristics of the valve, the stress had to be quantified. Fig. (2.11) illustrates how the membrane was clamped between the top and bottom part of the valve, while simultaneously measuring the
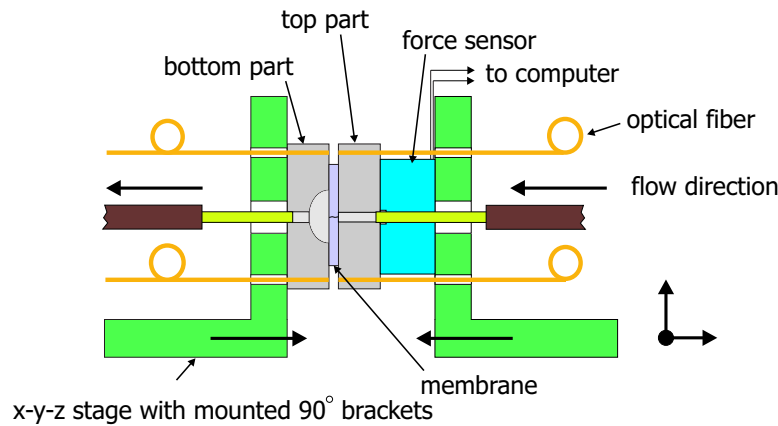
Figure 2.11: The bottom and the top part of the valve are mounted on separate x-y-z stages using 90°brackets. While the membrane is placed on the bottom part, the top part is additionally attached to a force sensor. Further, two optical fibers are embedded in each part. This allows to precisely align both parts controlling their relative position using optical readout.

force. The bottom part of the valve was mounted onto a x-y-z stage containing the aligned membrane using a 90°bracket. The top part was attached to a force sensor and correspondingly mounted onto a second stage. This allowed precise alignment of both parts relative to each other. Since the force measurements should be as accurate as possible, mechanical guidance was not feasible in this case due to friction. To be able to align both parts, two optical fibers were integrated into each part. While light was coupled into the fibers of the bottom part, the fibers of the top part were coupled to a two-channel detector. After alignment, top and bottom part could be joined using the stages and monitoring the force.

The force that is applied acts on the surface of the membrane and results in a stress. Thus, to be able to compare the results, the contact surface should be constant if different membranes are investigated. Instead of focusing on cutting out equal membrane dimensions, this was achieved by adding an elevation (like a mesa) to the top part's surface, as depicted in Fig. (2.12). An accurate cutout of the membranes is therefore not necessary as long as they are slightly larger than the area of the elevation.

To be able to avoid large forces and to investigate the influence of a locally applied stress the geometry of the valve seat was modified by adding a concentric ridge around the cavity, as shown in Fig. (2.13)

To estimate the influence of the observable adhesion between PMMA and PDMS on the opening pressure, the order of magnitude of this adhesion was determined. Test structures were fabricated casting PDMS around screws, as the magnification in Fig. (2.14) shows. The screws were attached to a holder that could be moved up and down with a z-stage (see Fig. (2.14)). Onto a
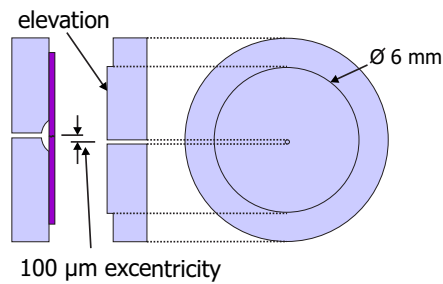
Figure 2.12: An elevation as part of the valve's top substrate ensures a constant stress when characterizing different membranes.
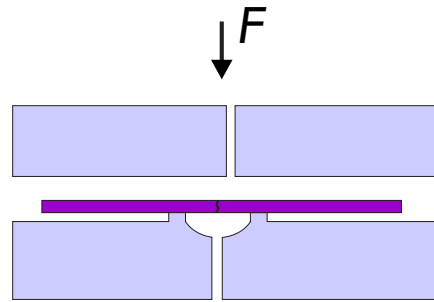
Figure 2.13: Modified valve seat geometry: a concentric ridge around the cavity allows to apply a local stress to the membrane.

balance, that could be read out with a computer, a PMMA substrate was placed. The PDMS sample was then brought into contact with the PMMA. Careful moving up the PDMS resulted in lifting of the PMMA, which could be detected with the balance to give a quantitative estimate of the adhesion. Additionally, the PMMA surface was wetted prior to the experiment, which allowed to compare the adhesion of PDMS to dry and wet PMMA surfaces.
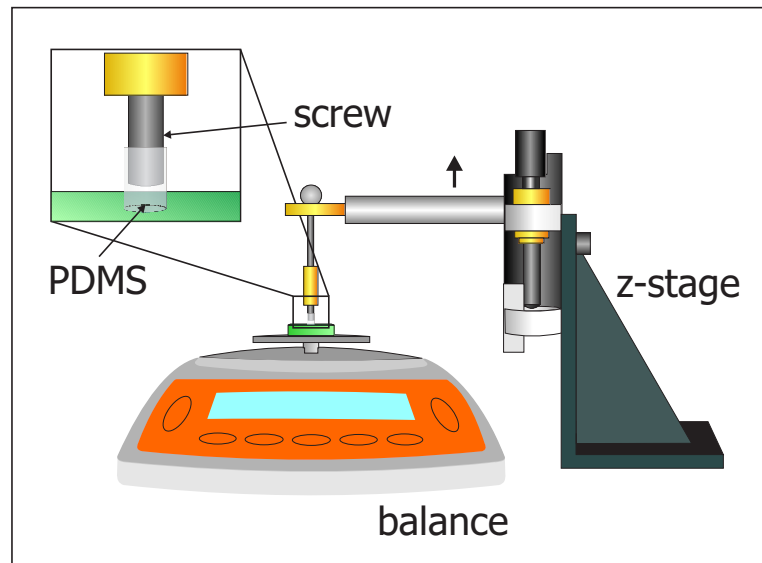
Figure 2.14: A screw was cast into a cylindrical PDMS test structure. On a balance, a PMMA plate was placed. The PDMS was brought into contact with the PMMA and subsequently, the PDMS test structure was lifted up using a z-stage. The adhesion of the PDMS to the PMMA also lifted up the PMMA, which was monitored with the balance.
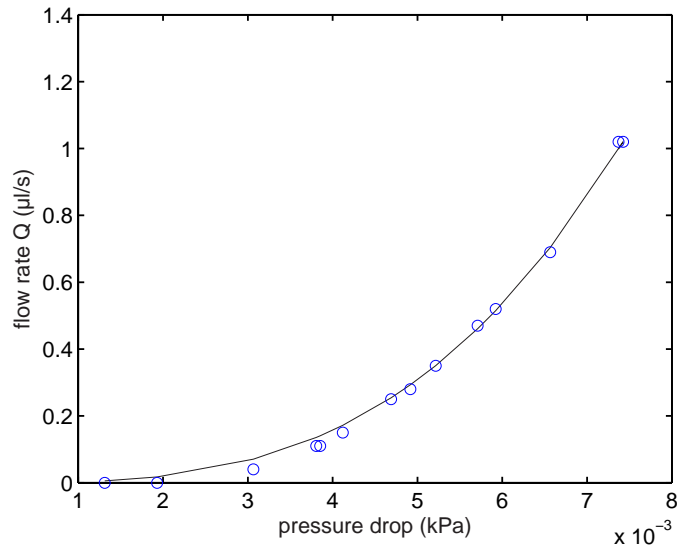
Figure 2.15: The circles represent the experimental data, which are compared to the theoretical model based on the equation for large deflection

2.6   Results and discussion

The results of the flow measurements recorded with the setup described above are shown in Fig. (2.15). Additionally, a plot derived from the theoretical model is displayed as well and shows excellent qualitative agreement with the measured values. To properly scale the model, a correction factor of 0.2 was used. As mentioned in Sec. (2.4), the applied equation is valid for large deflections of thin circular membranes. The deviation of the model from the measured data can be explained by the incision, which prevents the membrane to expand. Furthermore, the model does not consider a saturation of the membrane deflection, which was observed in the experiments, as can evidenced in Fig. (2.18). The expansion cavity only allows a certain expansion of the valve's membrane. Hence, starting from a certain pressure value, a further increase of the applied pressure leads to a linear rise of the flow-rate due to the constant slit width.

From measurements such as shown in Fig. (2.15) the opening pressure of the membrane was defined as the point where the tangent of the graphs linear part cuts the abscissa.

Fig. (2.16) and Fig. (2.17) show the valve's opening pressure dependent on the membrane thickness and the slit length, respectively. In accordance with Eq. (2.1) the membrane deflection is decreasing and thus the opening pressure of the valve is increasing with the membrane thickness. Also, the slit length has a great impact on the opening pressure, as can be seen from
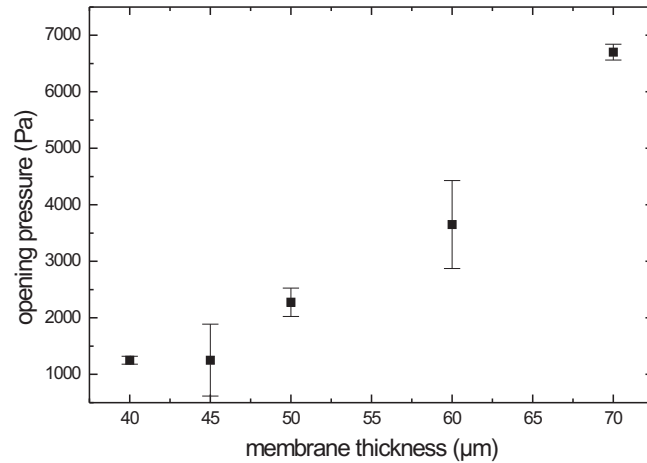
Figure 2.16: The maximum deflection of the membrane at a certain pressure, and consequently also the opening pressure, depend on the thickness of the membrane. While the deflection decreases the opening pressure increases with the membrane thickness.

Fig. (2.17). Since no backward flow was observed for any of the investigated slit lengths, the length of the slit should be maximized to the entire valve diameter to decrease the opening pressure.

To estimate the influence of an externally applied stress on the flow rate in open direction a set of flow-pressure characteristics for a test-valve at varying stresses was determined, as depicted in Fig. (2.18). It can be seen that the achievable flow rate at a certain pressure decreases as a result of increasing mechanical stress. Consequently, also the opening pressure of the valve is increased at elevated stress, as is documented in Fig. (2.19). Additionally, Fig. (2.19) shows the flow rate in the opening direction for increasing stresses recorded at a constant hydraulic pressure. Increasing the applied stress from, e.g., $0.8\,\mathrm{N/mm^2}$ to $1.2\,\mathrm{N/mm^2}$ can significantly reduce the flow rate, from $0.6\,\mu\mathrm{l/s}$ to $0.2\,\mu\mathrm{l/s}$. Entirely stopping the flow is also possible.

Swelling of the PDMS membrane, as reported in [39] did not seem to be a problem. In some cases, mainly when a large stress was applied to the membrane, after approximately one day a permanently opened valve was observed as depicted in Fig. (2.20).

To prevent swelling, exchange of the PDMS with a different elastomer should be considered. The commercially available elastomer membranes (vinyl, latex) had a thickness larger that $100\,\mu\mathrm{m}$. Experiments with custom made latex membranes were interrupted due to difficulties in achieving a
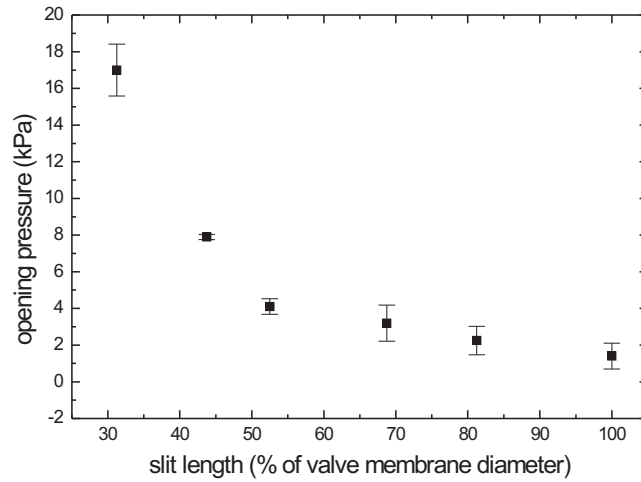
Figure 2.17: The opening pressure dependent on the slit length was determined using a membrane thickness of $70\,\mu$m. Slit lengths of $250\,\mu$m, $350\,\mu$m, $420\,\mu$m, $550\,\mu$m, $650\,\mu$m and $800\,\mu$m, respectively, were produced.
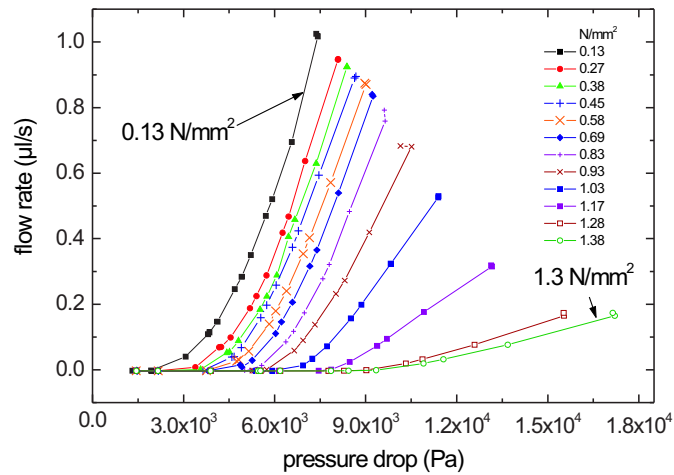
Figure 2.18: Measured flow rate data vs. applied pressure for a valve with an $800\,\mu$m cavity diameter using a $70\,\mu$m thick membrane with a $600\,\mu$m long slit. The set of curves shows the flow-pressure characteristics for different applied mechanical stresses.
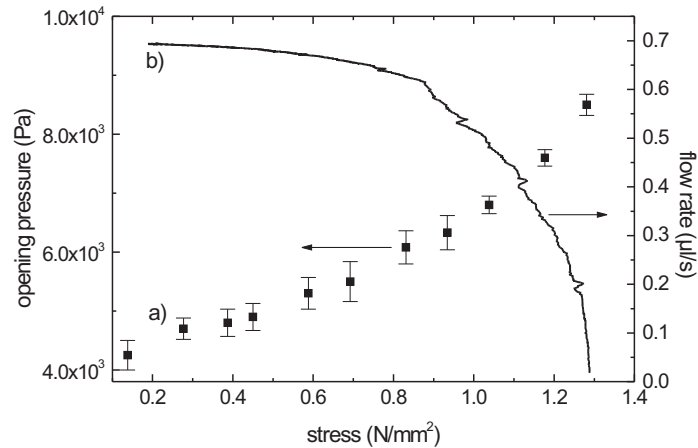
Figure 2.19: a) the opening pressure of the valve increases with increasing stress, b) as a result of increasing stress the flow rate at a constant applied pressure decreases.

homogeneous thickness. Further, wrinkling of thin latex membranes led to problems during assembly. Hence, further experiments are necessary to test latex as alternative membrane material.

Fig. (2.21) illustrates a more often observed problem that led to failure of the valve: debris was caught in the slit and prevented closing.

2.7 Conclusion

In this chapter, a novel check valve principle was presented. In contrast to various other passive valves, the membrane valve shows simple fabrication feasibility and can easily be integrated into microfluidic devices. Fabricating the valve using micromilling is only one example of various applicable fabrication methods, which additionally shows the valve's compatibility to the other elements presented in this work.

However, the simple fabrication is not the only novelty the check valve offers. Low opening pressure and zero flow in the backward direction emphasize the outstanding performance of the membrane valve principle. The compatibility of the used materials to a large variety of substances, for instance, biological samples, represents another important factor when dealing with the integration into bio-chemical microsystems.

A simple theoretical model was derived that showed good conformity to the experimental data and allows, to a certain extend, to predict the flow-rate in the forward direction depending on different valve membrane

parameters.

The dependence of the valve's opening characteristic on the stress that is applied to the membrane enables to actively control this characteristic. Hence, easy adaption of the valve to individual applications is possible. It was furthermore shown that totally suppressing the flow was possible. This allows to use the membrane valve as check valve that additionally has active valve capabilities. Since tuning of the valve is based on volume displacement inside the elastomeric membrane, it is possible to achieve sufficient characteristic changes already with small actuation. This makes it possible to use various actuation principles and thus, again, ensures the compatibility.

2.8 Outlook

The described tunability of the valve will be subject of further investigations. In a first approach, the focus will be put on the development of a discrete device that allows active control of the flow with combined check valve functionality. The possibility of applying different actuation principles allows, for instance, continuous tuning and therefore the development of a proportional valve. The properties of this valve will be investigated under different conditions.

Another focus will be the further miniaturization of the valve while considering the disadvantages smaller dimensions could have on the simplicity of the fabrication.

The use of different elastomers is a further step towards more compatibility and will be investigated in more detail in the near future.

The theoretical model has to be extended to explain the impact the mechanical stress has on the flow. Additionally, further experiments are necessary to investigate this phenomena in more detail.
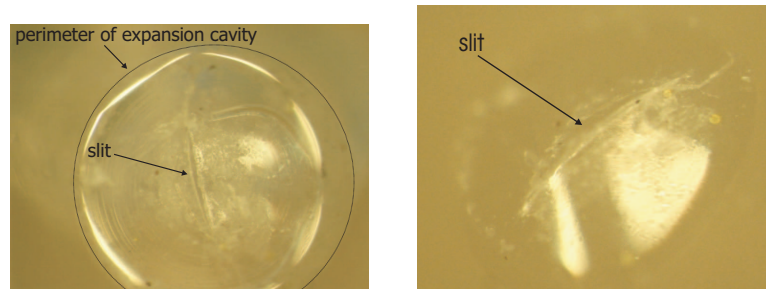
Figure 2.20: Swelling of the PDMS can lead to permanently open valves. However, this was only observed in very few cases.

Figure 2.21: Debris caught inside the incision prevented complete closing of the membrane and led to failure of the valve.

Chapter 3

Micropump

3.1 Introduction

Microfluidics offer the capabilities to distribute liquids, perform mixing or allow reactions to take place. The principles that are used to drive the liquid inside the channels can basically be divided into pressure-driven flow, on which this work will focus, and non pressure-driven flow. The pressure source can be a pressurized chamber, a pump, or even a vacuum applied from the outlet.

A pressurized vessel can only provide a limited volume that depends on the size of the vessel and the pressure inside. When a sufficient runtime of the microsystem is an important requirement, miniaturization using a pressurized source is only suitable for a limited number of applications. Thus, from the integrational point of view, a micropump represents a more flexible solution. Of course, a micropump also needs a power source to be driven, but the storage of, for instance, electrical energy is more convenient.

There is a very large number of publications on micropumps available in the literature, not least because of the almost infinite possibilities to combine valve principles and actuation mechanisms. It is beyond the scope of this work to give a complete overview of the many existing solutions. A recent review on micropumps was published by Laser and Santiago [2].

In fact, the aim of this work is to develop a device that is capable of pumping a fluid and which, on the one hand, can easily be integrated into a lab-on-a-chip system but, on the other hand, also be operated as a discrete device. As mentioned earlier, the demand for economic units that are fabricated in polymers and intended for single use is increasing. Integration in this context means not only combination of individual components but instead a fabrication towards monolithic systems. Hence, the compatibility of materials and fabrication processes between pump and lab-on-a-chip systems is of major importance. To fulfil these requirements, the pump in this work is entirely produced in polymer allowing mass production methods to
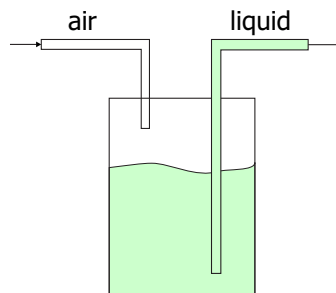
Figure 3.1: Principle of indirect pumping: air is pumped into the chamber and presses the liquid out.

be emplyed. Further, as actuator, piezo disk benders are used that allow easy control at low power consumption.

Work related to the approach presented in this chapter was, for instance, published by Truong and Nguyen [28,40], who laminated thin polymer discs to construct a micropump, which also contained spring check valves. A similar approach, albeit using conventional MEMS technology and materials for fabrication, was published by Meng *et al.* [41]. While Meng also used check valves, Schabmüller *et al.* [42] utilized diffuser valves to rectify the flow. However, both groups used cleanroom methods to process the valve elements, which complicated the fabrication and increased the costs. Kamper *et al.* [43] applied injection molding and laser ablation instead and presented an economic alternative. Böhm *et al.* [34] also renounced expensive materials and methods and described a plastic micropump fabricated with conventional techniques and materials.

Micropumps can be used to *directly* pump liquid through the channels of a microfluidic device. Since micropumps are often realized as diaphragm pumps, the resulting flow rate is pulsating. These peaks can be smoothened adding air-filled chambers, not unlike capacitors in electronic circuits [44]. However, the efficiency of liquid pumps decreases if air-bubbles are present, as discussed in Sec. (3.2).

Another approach is *indirect* pumping, as depicted in Fig. (3.1). Here, an (miniaturized) air pump generates a pressure inside a chamber that also contains the liquid, similar to the pressure source mentioned in the beginning. Since the air volume represents a large compliance, this method allows to achieve a smooth flow. Precise control of the flow rate, however, is a challenge and might require a feedback loop.

In this work, the focus is put on the direct pumping approach.
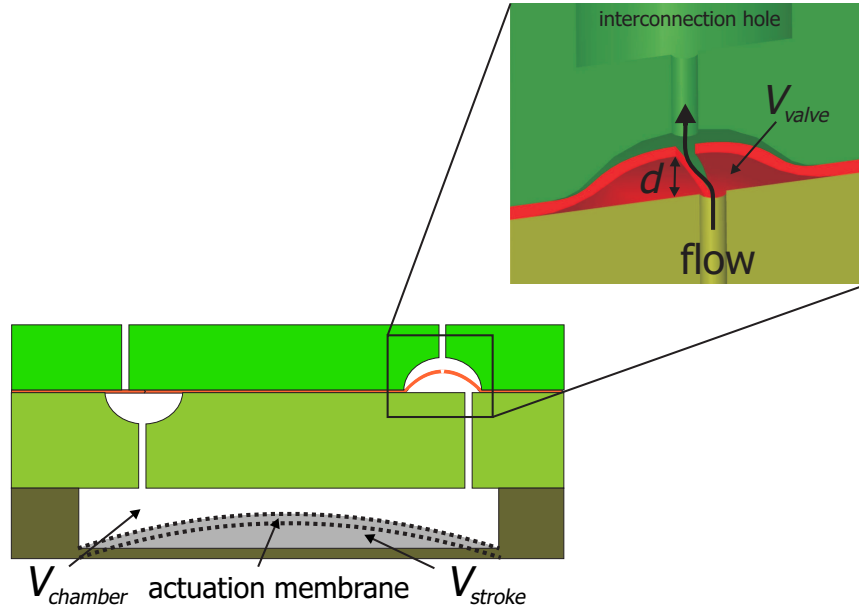
Figure 3.2: If the actuation membrane is deflected it displaces a volume V_{stroke} inside the pump chamber. This results in a deflection of the membrane valve, consuming the dead volume V_{valve}.

3.2 Theory

The basic working principle of a micropump is rather simple. Two check valves are connected in opposite directions to an actuation chamber. A partial vacuum generated in the chamber opens check-valve 1 and allows the fluid to enter the chamber. A subsequent overpressure closes check-valve 1 and opens valve 2 instead and allows the fluid to flow through valve 2. Hence, an alternating deflection of the actuator will generate a directed flow. Therefore, beside the actuator, the valves play a major role in the function of the pump.

The dead volume V_{valve} is defined as the volume that is accumulated inside a microvalve before a flow is obtained.

Considering the actuation chamber with the volume $V_{chamber}$ we can define the volume V_{stroke} that is displaced by the deflection of the actuator (see also Fig. (3.2)). The ratio between the displaced volume and the chamber volume is called compression ratio ε [45]:

$$\varepsilon = \frac{V_{stroke}}{V_{chamber}}. \tag{3.1}$$

Compressing the chamber volume increases the pressure inside the chamber, expressed by $\Delta p_{chamber}$. To obtain an opening of the valve a threshold pressure p_{thres} is necessary (see Ch. (2), opening pressure). Hence, a flow

can only be established if the compression is larger than the valve's opening pressure:

$$|\Delta p_{chamber}| > p_{thres} \qquad (3.2)$$

Compressing the medium inside the pump chamber requires a compressible fluid. If liquids are pumped directly, the medium can, due to the low compressibility of liquids, be considered as non-compressible. Hence, the pressure generated by the actuator is directly transmitted to the membrane valve, thereby satisfying Eq. (3.2) already at small actuations. However, a pump chamber entirely filled with incompressible liquid is not a realistic estimate. A major problem of micropumps are gas-bubbles that are trapped inside the pump chamber. The origin of the bubbles can be gas that is dissolved in the liquid and outgasses during pumping or simply gas that is transported with the flow and trapped inside the chamber. It is therefore advantageous to assume a compressible medium to ensure working of the pump. The compressibility of the medium hereby varies with the amount of gas inside the chamber. Thus, an air pump represents the extreme condition of an entirely gas filled pump chamber.

Design criteria for micropumps were derived in [45]. For gas pumps the compression ratio should be:

$$\varepsilon_{gas} = \frac{1}{\gamma}\frac{|p_{thres}|}{p_0}, \qquad (3.3)$$

where γ is the adiabatic coefficient and p_0 is the atmospheric pressure, and for liquid pumps

$$\varepsilon_{liquid} > \kappa \mid p_{thres} \mid, \qquad (3.4)$$

with κ the compressibility of the liquid.

Only an infinitely rigid pump pumping an incompressible medium transduces the input signal applied to the actuator without distortion or loss and results in a corresponding flow. Despite the small compressibility of the liquid the mentioned gas bubbles will add compliances to the system. Furthermore, the check valves of the presented pump consist of elastic membranes and can be considered hydraulic capacitors. Hence, apart from the above mentioned design criteria representing the static behavior of the pump, its dynamic properties have also to be considered. As check valves for the pump, the membrane valves presented in Ch. (??) were integrated. The compliance of these valves can be estimated calculating the pressure dependent volume deformation [46]:

$$C_{fluidic} = \rho \frac{dV}{dp} \qquad (3.5)$$

3.3   Design and Fabrication

According to the requirements mentioned above, the micropump is, with the exception of the actuator, entirely fabricated in plastics. For actuation of the micropump presented in this work, a piezo disk-bender is used, as can be seen in the cross sectional view of the micropump depicted in Fig. (3.3). Actuating the piezo leads to a deflection and results in volume displacement and compression of the fluid inside the pump chamber. As a consequence of the increased pressure, the membrane of the outlet valve deflects, its incision opens and fluid can pass through the valve. Subsequently, the pressure inside the pump chamber decreases and the outlet valve closes. Then, the actuator is relaxed, which leads to a vacuum inside the pump chamber and results in an opening of the inlet valve. Fluid is drawn into the pump chamber until the pressures are balanced. Now, a new cycle starts.

In contrast to other pumps utilizing disk benders, the piezo in our approach can only bend in one direction. As a consequence, the stroke is reduced to 50% of the possible actuation volume. This is, however, acceptable because it allows an easy mounting of the piezo inside the pump and the use of elastomeric material as actuation membrane. Normally, piezo disks are glued onto a rigid but flexible actuation membrane [29, 43, 47], which is deflected by the piezo. One the one hand, monolithically integrated polymer membranes are difficult to achieve with conventional polymer fabrication technologies. Using foils in combination with bonding techniques, on the other hand, increases the risk of leakage due to failure of the bonding caused by the continuous bending. An elastomer instead provides good sealing capabilities, high durability and easy fabrication. Furthermore, the efficiency of the pump is increased since less energy is consumed by the deflection of a comparable polymer membrane.

The micropump is assembled of three individual layers, which are described separately in the following paragraphs:

bottom layer   The bottom layer houses the piezo disk, which is cast into PDMS. First, a $3\,\mathrm{mm}$ thick PMMA plate is structured by micromilling to achieve a geometry as depicted in Fig. (3.4). A centered circular cavity ($400\,\mu\mathrm{m}$ deep) acts as a seat for the disk-bender ($400\,\mu\mathrm{m}$ thick). To connect the piezo, wires are soldered onto both of its surfaces. While the wire from the top surface is conducted to the outside via a wire channel, the bottom connection is made via a through hole that additionally acts as a vent for the disk-bender.

To assemble the bottom layer and piezo, the piezo is positioned into the seat and connected with the wires. PDMS is subsequently poured onto the piezo surface and bottom structure. A glass slide is then clamped onto the bottom structure to seal the piezo. The mesas act as spacers, which define the thickness of the PDMS layer above the piezo. With a height of
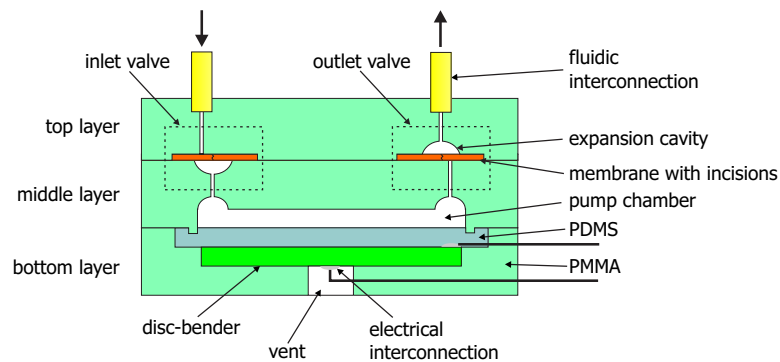
Figure 3.3: Functional cross-sectional sketch of the micropump: when the disk-bender is actuated, the volume in the pump chamber is compressed. As a result, the membrane of the outlet valve is deflected, its incision is opened and fluid can pass through the valve. Relaxing the disk-bender closes the outlet valve and generates a low pressure, which opens the inlet valve and draws fluid into the pump chamber.
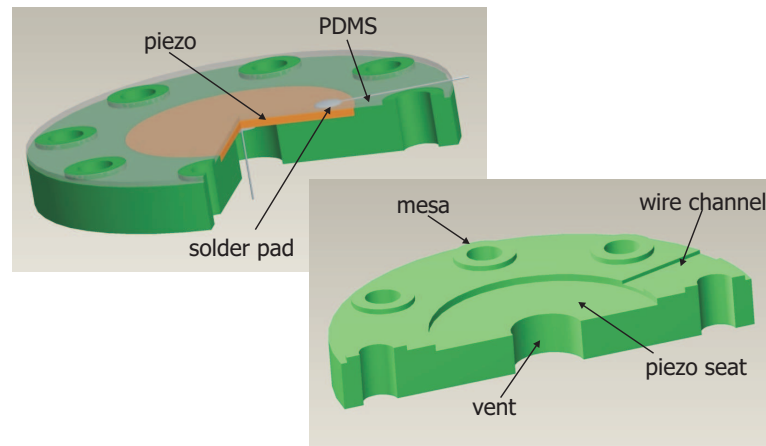
Figure 3.4: The topology of the bottom layer was realized by micromilling and drilling. The cavity acts as a seat for the piezo disk. To connect the piezo, wires are soldered to its surfaces that are conducted to the outside via a wire channel and a vent, respectively. A PDMS layer is cast onto the piezo as the inset Figure shows, with its thickness defined by the height of the mesas.

$200\,\mu$m a thin elastomer membrane is achieved that acts as a gasket for the pump chamber as well as an insulation for the piezo. The setup is then put into an oven at 60°C for 2 hours. It could be observed that sometimes curing of the PDMS was partly inhibited above the piezo. Even thorough cleaning to avoid any influences of soldering flux residuals gave no satisfying results. Therefore, prior to applying the PDMS to the piezo, its surface was

lubricated with cure accelerator (DowCorning® Q3-6559), which ensured an optimal curing. To prevent the glass slide sticking to the PDMS after curing, a thin PMMA foil was put in between as an intermediate layer. This could be peeled of the PDMS surface without destruction of the membrane. Casting the piezo into PDMS has additionally the advantage to avoid any mechanical tolerances or space between the actuator and the attached structure. Thus, the entire deflection is transmitted to the valve chamber.

middle layer   Structuring the middle layer, as shown in Fig. (3.5), is performed by double-sided milling. This can be achieved by turning around the substrate using dowel pins for alignment (see App. (B)). Preferably, the top surface is structured first, which allows a planar support after the structure is turned around and before the ridge is fabricated.
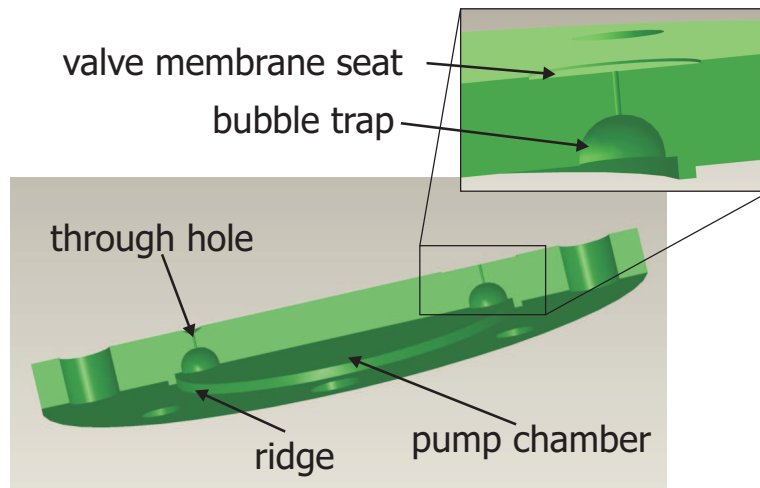
Figure 3.5: A concentric ridge around the pump chamber ensures proper sealing when the middle layer is pressed onto the PDMS of the bottom layer. Hemispheric cavities, that are connected via through holes to the top surface, trap potential bubbles and allow to remove them easily. While one of the through-holes connects the pump chamber to an expansion cavity of a membrane valve (inlet valve), the other through-hole is connected to the seat for the other valve's membrane (outlet valve).

Focusing in a first attempt on a liquid pump, small cavities were added to the through holes that connect bottom and top layer. These cavities act as bubble traps and allow to remove bubbles more easily during operation of the pump. In an air pump design, however, they should be omitted.

top layer   Corresponding to the middle layer, the top layer contains the respective counterparts of the microvalves. For a prototype, additionally,

connection hole

expansion cavity   membrane seat
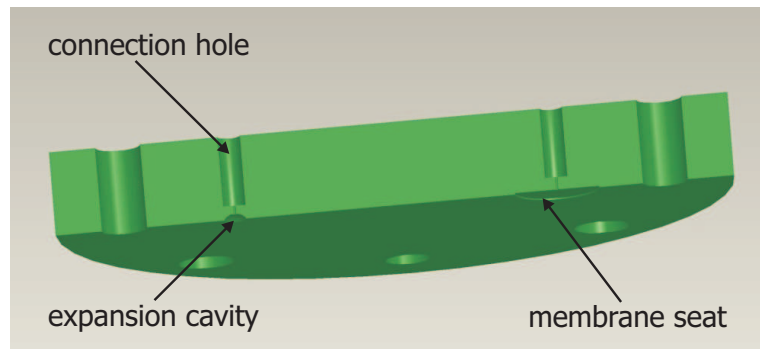
Figure 3.6: The top layer contains the corresponding counterparts of the pump's microvalves. Additionally, through-holes allow easy interconnection of the pump to tubes

two connections holes were drilled into the substrate as Fig. (3.6) shows. Thin-walled metal tubes were press-fitted into these holes and provide a sealed fast interconnection for a discrete device.

After fabrication of the individual layers, the pump was assembled as depicted in Fig. (3.7). First, bottom and middle layer are joined using four screws. The concentric ridge at the edge of the pump chamber that is machined into the middle layer is thus pressed onto the PDMS of the bottom layer and seals the chamber. To avoid seize of the piezo due to the high mechanical stress resulting from the ridge, the diameter of the ridge is slightly larger than the piezo's diameter. As mentioned, the thickness of the PDMS layer is $200\,\mu$m, while the height if the ridge is $75\,\mu$m.

Membranes, prepared with an incision (as described in Ch. (2)), were then placed into the membrane seat of the middle and top layer. The membrane seats has the purpose to limit the strain that is created by pressing the elastomer together. The total strain is thereby limited to the difference between the membrane thickness and the depth of the membrane seat (see Ch. (2) for further details). Finally, the top layer was attached to the middle layer using four screws.

While a certain stress is necessary to seal the pump chamber, the stress to the membrane valves has to be applied with care. Consequently, both stresses should be adjustable independently. The middle layer as well as the top layer are equipped with eight through holes. Four holes on each layer are provided with a thread, staggered to the threads of the corresponding layer, as shown in Fig. (3.8). This makes it possible to apply different stresses between the middle and the bottom or the top and the bottom layer, respectively. The membrane seat additionally prevents exceeding a maximum stress that could lead to failure of the valve due to deformation.
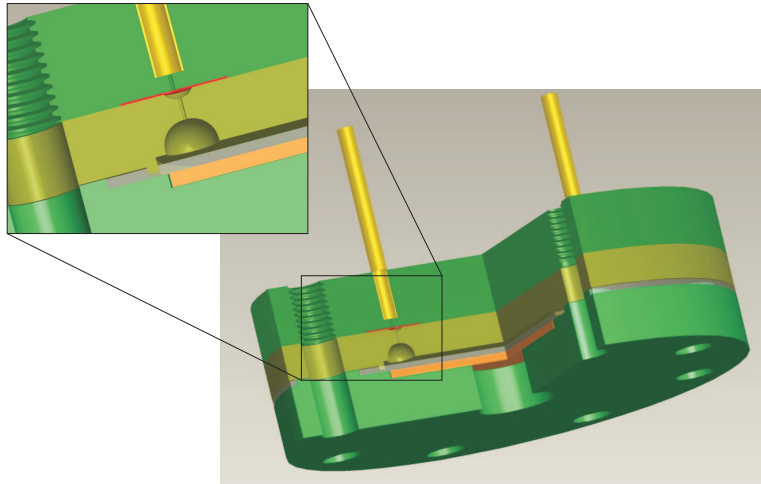
Figure 3.7: Assembled view of the pump. For simplicity, the piezo contact wires are not displayed. The inset shows a magnification of the check valve configuration.
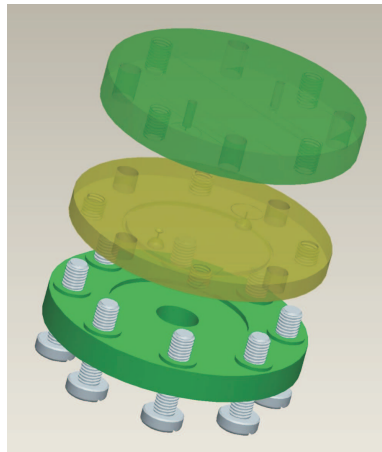
Figure 3.8: Screws were used to assemble the pump. To be able to apply individual stress between bottom and middle layer on the one hand, and middle and top layer on the other hand, two groups of four screws each were used.

3.4   Measurements and Experiments

For characterization of a micropump, the maximum and minimum achievable flow and pressure are important features. Furthermore, depending on the actuation principle, the flow is related to the frequency the actuator is triggered with.

As mentioned, in this work a piezo disk-bender is used for actuation. Limiting values are therefore given by the characteristics of this element.
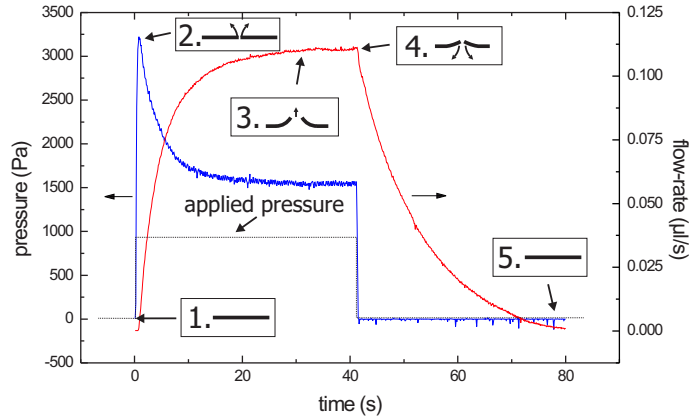
Figure 3.9: Characteristics of the flow-rate and the pressure drop over the valve when a pressure impulse is applied: (1) external pressure is applied, the pressure drop over the valve increases; (2) the valve starts to open, the flow begins to increase, the pressure drop decreases; (3) the valve is open and the maximum flow-rate is achieved, the pressure drop is constant; (4) application of external pressure is stopped, the valve closes, while the pressure drop over the valve immediately stops, the flow-rate decreases slowly; (5) flow-rate and pressure drop converge to their initial level.

The blocking force of the piezo is specified to $2.4\,\mathrm{N}$ at an applied voltage of $170\,\mathrm{V}$, which results in a maximum pressure of $19\,\mathrm{kPa}$ considering its diameter of $12.4\,\mathrm{mm}$. The maximum stroke volume of $1.074\,\mu l$ can be derived from the piezo's free center deflection of $19.1\,\mu\mathrm{m}$.

In contrast to Ch. (2), in which the static properties of the membrane valve were discussed, here, their dynamic behavior is more interesting. The alternating actuation of the piezo is translated to a pulsing expansion of the valve's membrane. As also mentioned in Ch. (2), the resistance of the valve depends on the membrane's expansion.

To determine the dynamic behavior of the membrane, an external pressure impulse is applied to the valve. The reactions of the flow-rate and the pressure that is measured across the valve (pressure drop) are depicted in Fig. (3.9). Five characteristic sections can be identified: (1) an external pressure is applied and the valve remains closed until a threshold pressure is achieved in (2), which expands the membrane so the valve starts to open and the flow-rate increases. As a result, the pressure drop decreases until the valve is opened completely in (3). In (4), the external pressure is turned off and the pressure drop decreases immediately, while the flow-rate decreases slowly until both reach their initial level (5).
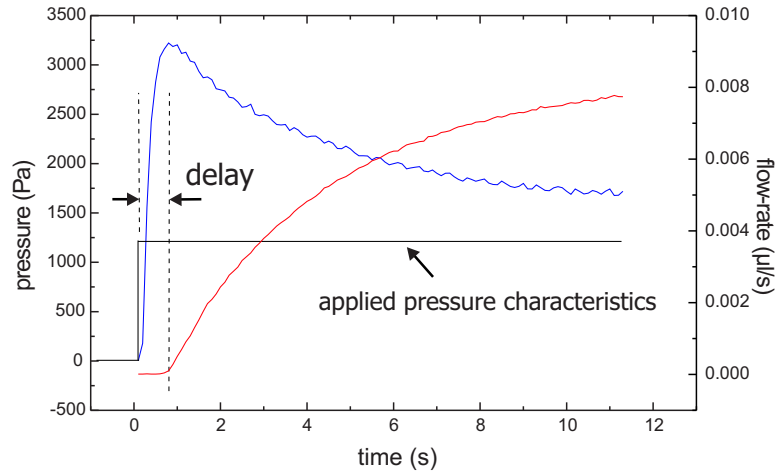
Figure 3.10: Zoom-in of the characteristics in Fig. (3.9): opening period of the valve after application of the external pressure. The flow through the valve first begins when a threshold pressure drop at the valve is reached. This threshold pressure is equal to the opening pressure described in Ch. (2).

The time that is necessary to open the valve at a certain applied pressure (see Fig. (3.10)) is important for determining the optimum actuation frequency of the micropump. If the periodic time of a pump cycle is too short, i.e. the frequency is too high, the valve does not open completely, which results in a low or no flow rate. A low frequency, on the other hand, the relaxing time of the membrane can be shorter than the actuation time, which leads to single strokes but no continuous flow.

In analogy to electronics, this can be described by the time constant τ, which is determined as shown in Fig. (3.11) [48]. The tangent at the zero point of the flow rate characteristics cuts the asymptote $Q = Q_{max}$ in $t = \tau$.

A square wave signal with frequencies between 1 and 30 Hz and an amplitude of 170 V was applied to the actuator to determine the flow-rate depending on the actuation frequency. The frequency at which the maximum flow-rate was measured was further used to estimate the maximum achievable pressure. The outlet of the pump was connected to a vertically mounted tube and the maximum height of the liquid column relative to the pump outlet was measured.

3.5 Results and Discussion

The deflection of the valve membrane depending on the applied pressure determines the compliance of the valve, as mentioned earlier in Sec. (3.2). Parameters influencing the deflection therefore also have an impact on the compliance. The time constant of the membrane valve was obtained for the
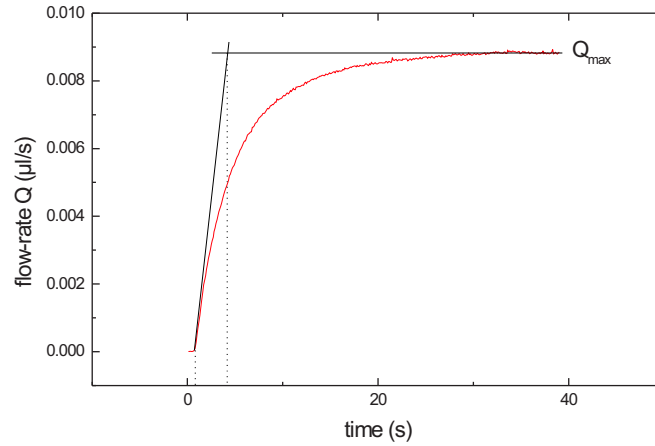
Figure 3.11: The time constant τ was determined from the flow rate's response on the applied pressure step function: the tangent to the point of zero flow cuts the asymptote at $t = \tau$.

applied external stresses and the membrane thickness as two selected influencing parameters. Fig. (3.12) shows an increase of τ with increasing stress. As a consequence of the experiments described in Ch. (2), however, the opening pressure and thus the deflection of the membrane were decreasing with increasing stress. Based on that, the compliance should decrease with increasing stress. Thus, both results seem to contradict each other and are not understood in detail yet. The characteristics of τ in dependence of the membrane thickness, on the other hand, is consistent with the assumption that a smaller membrane deflection caused by a thicker membrane results in a decrease of the compliance, as depicted in Fig. (3.13).

The determination of τ delivers a characteristic value for the check valve that has to be seen isolated from the micropump. However, the pump not only contains the valves but, for instance, additionally an actuator and a pump chamber that influence the pump's overall characteristics. As mentioned further above, one estimate of its performance is the flow-rate the pump can deliver. Fig. (3.14) shows the flow-rate at varying pump frequencies. Increasing rapidly from $21\,\mu$l/s at $1\,$Hz a maximum at approximately $5\,$Hz can clearly be observed before the flow-rate decreases continuously with increasing frequency.

The maximum back-pressure of the pump was found to be $12.4\,$kPa using the method described above, which equals $65.2\,\%$ of the maximum achievable theoretical pressure.
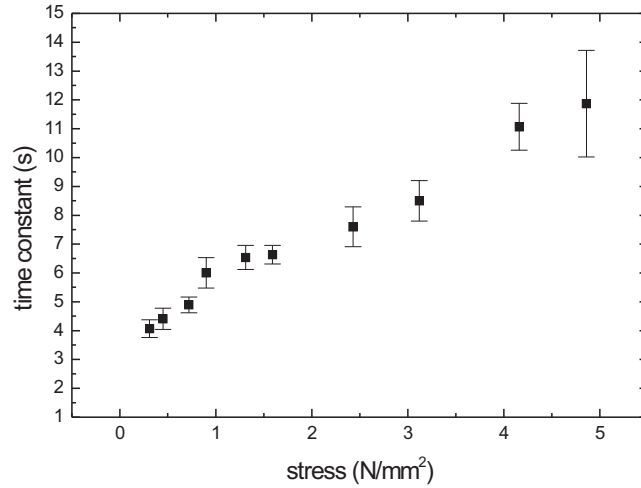
Figure 3.12: The graph shows an apparent linear relation between the time constant τ and the applied mechanical stress. τ was determined with the method described above.
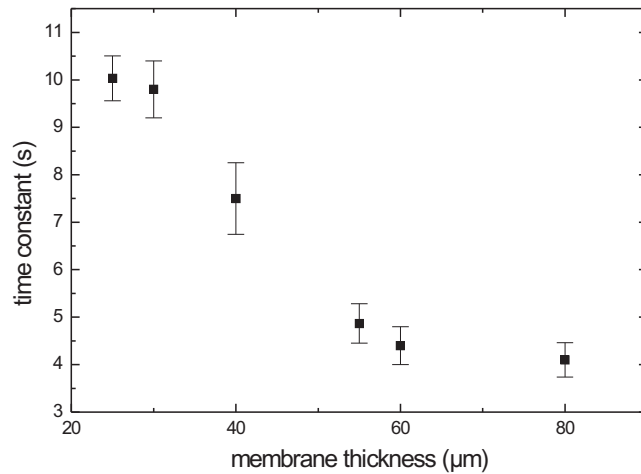
Figure 3.13: With increasing membrane thickness the deflection of the membrane at constant pressure and consequently the time constant are decreased.
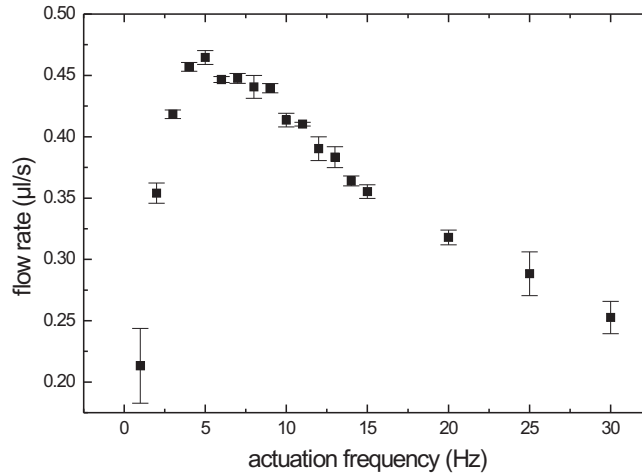
Figure 3.14: The dependence of the flow rate on the actuation frequency can be clearly seen from this graph. A maximum flow rate can be observed at $\approx 5\,\mathrm{Hz}$. The membranes of the tested pump had a thickness of $30\,\mu\mathrm{m}$.

3.6   Conclusion

First and foremost it has to be noted that the presented pump was designed to demonstrate an easy to fabricate pressure source. The multi-layer construction allows easy assembly and, if required, easy disassembly of the pump. Apart from that, the structuring of individual layers makes the combination with other components presented in this work possible, that additionally are fabricated onto the layers. Compatibility is therefore ensured. A good performance of the micropump could be verified. Even though no optimization was conducted yet, the pump delivered a maximum pressure that was larger than 65 % of the theoretically possible pressure. Also, the achieved flow-rates were in a range that can be used for applications, for instance, for the bioXtas chip, presented in Ch. (9).

From the constructive point of view, the mounting of the piezo as an embedded element represents a method that can compensate for fabrication tolerances. The gaps that would lead to clearance between actuator and actuation membrane are avoided by directly casting the piezo into the membrane material. Furthermore, the elastomeric membrane material acts as sealing and, again, simplifies the fabrication procedure.

3.7 Outlook

After the working principle was proven, the pump has to be optimized. In order to reduce the dimension of the pump itself, the compliance of the membrane valves should be minimized keeping the opening pressure low. Since the volume displacement of the actuator drastically decreases with smaller radius, further miniaturization of the microvalves is a major issue.

To utilize both deflection directions of the piezo, its mounting principle should be modified. Moreover, the necessary voltage should be reduced.

To allow more economical assembly, an alternative to the used screws should be investigated.

Chapter 4

Active microvalves

4.1 Introduction

The backbone of lab-on-a-chip devices is their microfluidic network, which for instance allows transport of liquid between different areas of the chip. To control the flow, microvalves are necessary. While passive valves are widely used to realize micropumps, active valves are the preferable choice for the distribution of fluids in a μTAS.

This project investigates a novel method for a microvalve exploiting the hydraulic principle. In contrast to earlier studies, which mainly describe solutions for specific applications, this work attempts to develop a device, that can operate as a stand-alone component as well as be integrated into existing systems. It has to be emphasized that, next to the realization of a working device, a major focus of this project is the simplification of the fabrication process.

As mentioned in Ch. (2), at present a substantial body of research on microvalves exists that was recently reviewed by Kwang and Ahn [4]. In contrast to check valves, active valves need to be actuated to provide a valve function and are therefore often grouped with regard to their actuation principle. More fundamentally, active valves can be divided into valves exploiting integrated or external actuation [4]. Since in this study the focus is put on active valves that use flexible membranes as functional parts, the review of earlier publications is limited to those using elastic materials.

For some years now, an increasing amount of literature is devoted to elastomeric materials in microfluidics [9]. The advantages of these rubber-like materials, such as silicone, are, on the one hand, their sealing capabilities, which are also known in everyday life. On the other hand, their flexibility allows easy deflection of thin diaphragms due to the low Young modulus [49]. Among others, these properties make elastomers a suitable material for microfluidic systems.

Quake *et al.* demonstrated the impressive potential soft elastomers offer

and built multilayer devices including pumps and valves using soft lithography [9, 50]. Baek *et al.* achieved a valving function utilizing a structured PDMS membrane embedded in silicone [51], while Öhmann and Young used conventional MEMS fabrication in combination with a silicone membrane to seal a channel [52, 53]. However, the above mentioned applications exploit the capability of large deflection and flexible conformation of elastomer membranes by using external pressure for actuation. Although the microvalve itself has small dimensions, a large pressure source and additional external valves have to be used to control the microvalve. The advantages of a highly integrated fluidic network as described in [50] needs therefore be considered in the context of the required large control units.

The small strokes microactuators usually provide complicate the fabrication of entirely integrated devices. However, various types of integrated active microvalves were developed that use, for instance, magnetic [54], electrostatic [55] or thermal [56] elements for actuation. Using piezo disk benders necessitates an amplification of their deflection to achieve useful stroke magnitudes. Rogge *et al.* presented in [57] a hydraulic transmission that translated the small piezo deflection to a larger movement of a valve membrane. Since the principle was based on sealing the face side of through holes, the dead volume of this valve was relatively large. Furthermore, this configuration does not lend itself for high density fluidic networks.

This work describes the effort to combine the direct in-line sealing of microchannels, which offers low dead volumes, as shown in the approaches by Unger and Quake, with the a piezo driven actuation mechanism. Integrational aspects as well as the common problem to fill a closed chamber with liquid have been given proper attention.

4.2 Working Principle
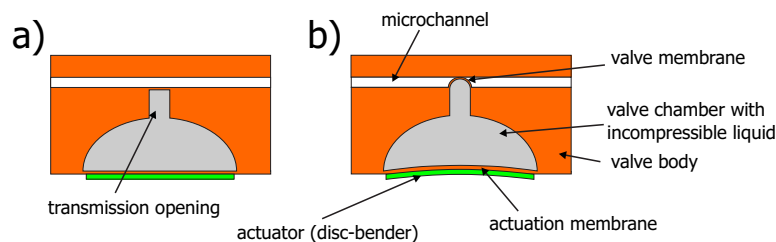
Figure 4.1: Working principle of the active valve: a small deflection of the actuator transmitted to the actuation membrane displaces a certain amount of fluid inside the valve body and leads to a deflection of the valve membrane. Allowing the valve membrane to expand into a microchannel can be utilized as valve function.

As figure 4.1 shows, the device basically consists of a cavity machined

into a substrate that has a large opening on the bottom side and a pin-hole opening at the opposite side. Both openings are covered with membranes and the cavity is filled with an incompressible liquid, the transmission liquid. A small deflection of the large area bottom membrane (actuator membrane) displaces a certain volume of liquid, which leads to a large deflection of the small area top membrane (valve membrane). If the elastomeric valve membrane is allowed to expand into a microfluidic channel, it clogs the channel and a valve effect can be achieved. By directly clogging a microfluidic channel instead of designing a designated valve seat the disruption of the flow inside the channel and the dead volume can be minimized.

The circumstance that a small deflection is amplified to a large stroke offers the possibility to use piezo ceramics as actuators. In this work, bimorph actuators in disc form, so-called 'disc-benders' are used to generate the deflection. In contrast to 'stack-actuators', which can generate high forces, bimorphs produce larger deflections at smaller footprints, which makes them suitable for integration. Another aspect is the price of disc-benders, which is a fraction of the price of stack-actuators and allows therefore a more economical production.

The application of the hydraulic principle requires a chamber entirely filled with liquid. The presence of gas bubbles leads to compression of the gas during actuation and hence to failure of the device. Filling of chambers represents an often described problem in microfluidics [58]. Not only the filling itself, but also the closing of the chamber represents a challenge. Any residual liquid that lubricates the surfaces prevents a simple covering of the filling openings and subsequent bonding. This issue was accommodated by using a simple but effective filling method.

Since the amplification of deflection is based on volume displacement, the valve not only amplifies the actuation of the piezo but is rather sensitive to any volume change of the liquid, which can, for instance, been caused by thermal expansion. Thus, differences in expansion coefficients between the transmission liquid and the valve body have to be minimized to avoid failure of the valve due to temperature influences. To circumvent this problem, the entire valve, except the actuator, was fabricated in silicone and as transmission liquid silicone oil was used, which reduced the mismatch in thermal expansion to $\approx 1\,\%$.

4.3   Theory

Since disc-benders deflect in and out like a drum head, the displaced volume V can be described by

$$V = \frac{1}{6}\pi h(3a^2 + h^2), \tag{4.1}$$

where h is the center deflection and a the radius of the disc. Equation 4.1 can be transformed to

$$h = \sqrt[3]{\frac{3V}{\pi} + \sqrt{\frac{9V^2}{\pi^2} + a^6}} + \sqrt[3]{\frac{3V}{\pi} - \sqrt{\frac{9V^2}{\pi^2} + a^6}} \tag{4.2}$$

to determine the maximum height.

Equation 4.2 shows, that the membrane radius has a great impact on the deflection at certain applied pressures. At this point, a consideration has to be made between miniaturization and necessary deflection. In this project, commercially available discs with a diameter of 6.4 mm were used (Piezo Systems, Inc., Cambridge, MA USA). The maximum free deflection of these discs is 4.7 μm and the blocked force is 2.4 N, which equals a max. applicable pressure of 74,063 Pa. Transferring this to the bottom membrane of the device, a volume of 0.075 mm^3 is displaced, which, theoretically, leads to 480 μm center deflection of the top membrane (6.4 mm bottom membrane diameter, 300 μm top membrane diameter).

However, deflection of the elastomeric membrane requires a certain force. Based on the theory of thin plates, the deflection can be approximated for uniformly loaded circular plates. The max. deflection h_{max} can be described by

$$h_{max} = 0.29a \sqrt[3]{\frac{pa^4}{tE}}, \tag{4.3}$$

where a is the radius, p the pressure drop, t the thickness, and E Young's modulus.

While the pressure is given and the Young modulus can only be slightly adjusted, the membrane radius and its thickness are design parameters. Eq. (4.3) shows that with increasing radius and decreasing thickness the membrane deflection rises. The radius of the valve membrane is determined by the channel width and can, to a certain extent, be adapted to the requirements. In most cases, however, the channel width should be minimized, which only leaves room for variation of the membrane thickness. Eq. (4.3) can be transformed to obtain the maximum membrane thickness t_{max} to achieve a certain deflection h:

$$t_{max} = \frac{0.24pa^4}{Eh^3}. \tag{4.4}$$

Assuming Young's modulus to be 1.0 MPa and an actuation pressure of 70 kPa, Tab. (4.1) shows maximum membrane thicknesses for different channel dimensions.

Eq. (4.4) only refers to the pressure that is necessary to deflect the membrane. Proper sealing of the channel, however, additionally requires to

channel width in μm	channel height in μm	deflection volume in mm^3	max. membrane thickness in μm
100	100	0.00092	0.14
200	100	0.00209	2.18
200	200	0.00733	0.27
300	100	0.00406	11.02
300	200	0.01126	1.38
300	300	0.02474	0.41
400	100	0.00681	34.81
400	200	0.01676	4.35
400	300	0.03299	1.29
400	400	0.05864	0.54

Table 4.1: To seal a channel using an in-line sealing approach requires filling out its entire cross sectional profile with the deflected membrane. Assuming a hemispheric channel cross section, the maximum allowed membrane thickness is calculated depending on the channel width and height applying the maximum applicable pressure of the piezo. Additionally the deflection volume is shown, which must not exceed the piezo's displacement volume of $0.075\,\text{mm}^3$

consider the hydraulic pressure inside the fluidic channel , which depends on the individual application.

As a conclusion from Tab. (4.1), a major effort has been put on the fabrication of thin elastic membranes. The integration of a valve seat, and thus allowing a larger membrane diameter, was not considered to be an option in the first approach due to the increase of dead volume.

4.4 Fabrication

To seal the microchannel with the expanded membrane a large deflection is necessary that is accompanied by direct stress inside the membrane itself, as discussed in Ch. (2). The membrane attached to the valve body exposes that junction to stress and strain and requires a strong bond. To circumvent this problem, instead of fabricating valve body and membrane separately and, subsequently, bond both components together, a mold was developed that allowed to cast the valve body including valve membrane in a single casting step.

The mold, as depicted in Fig. (4.2) consisted of six individual layers that were structured by micromilling. The bottom, middle and top layer together with an o-ring formed the actual negative for the valve body. A vertical pin that was inserted into the bottom layer's center hole was fixed by a tight fit in the clamping layer. The purpose of the pin was to define the membrane
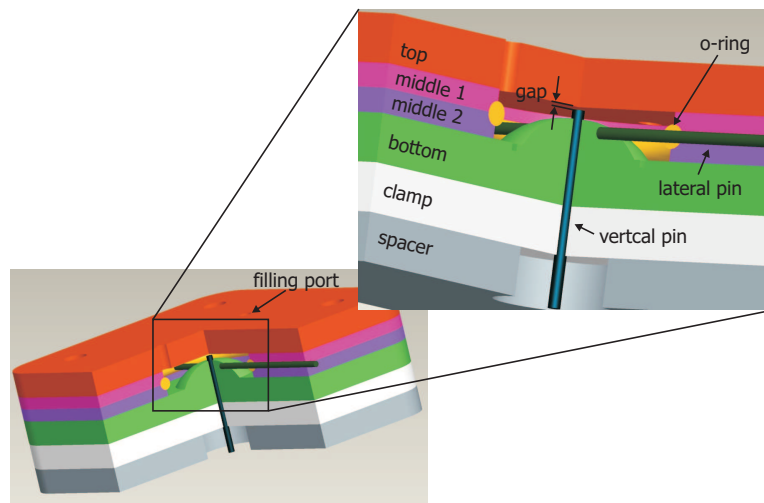
Figure 4.2: The negative mold for the valve body was achieved by mounting the bottom, middle and top layer on top of each other. Into a center hole of the bottom and clamp layer, a pin was inserted that defined the membrane thickness by its distance to the top layer (gap). To fix the pin in position, the hole in the clamp layer was smaller than the pin's diameter, which resulted in a tight fit. The spacer prevented movement of the pin during handling of the mold. The top layer contained two through-holes as filling port and vent.

by a gap that was established between the pin's top end surface and the top layer. The clamping layer was manufactured from teflon which allowed, on the one hand, a fixed position of the pin but, on the other hand, to adjust the pin manually. To create a gap with a sufficient size, two methods were tested. The first approach used a small foil with a thickness of the designated membrane thickness and a diameter smaller than the valve's body diameter. The foil was placed onto the bottom surface of the top layer before this was mounted. After assembly of the mold, the pin was inserted until it touched the foil. Subsequently, the foil was removed by de- and remounting the top layer. This method allowed to precisely generate a gap corresponding to the size of the foil thickness.

Applying the second method, the mold was completely assembled and the pin was inserted until it touched the top layer. By pressing onto the top layer with a sufficient force, the top layer bent and the pin was slightly pressed down. After releasing the load, the top layer relaxed while the pin was kept in position, and a gap was established. Although this method necessitates calibration of the force-gap relation to achieve reproducible results, it represents a fast and easy to handle solution.

Two equally formed middle layers were inversely mounted on top of each other to yield a hemispheric groove that housed an o-ring. The o-ring was mounted prior to casting creating an annual groove in the valve body.

A syringe was used to fill the mold by carefully injecting the previously mixed and degassed PDMS, as depicted in Fig. (4.3). A second through-hole in the top layer acted as vent and allowed air to escape. The PDMS was then cured at ambient temperature for six hours to prevent stress and geometry changes due to expansion of the mold during heating. To decrease the curing time, a cure accelerator (DowCorning® Q3-6559) was added.

Fig. (4.4) shows a cross-sectional picture from a cured valve body with cast membrane. Careful removal of air is important to avoid bubbles as shown in Fig. (4.5). Further problems occurred during filling of the mold: it could be observed that, due to the high viscosity, the gap between pin and top layer was not sufficiently filled with PDMS. Increasing the gap by pulling the pin slightly out and subsequent re-adjustment using the "load"-approach as described above, helped to circumvent this problem. Removing the pin too fast after curing generated a vacuum below the thin membrane that drew the membrane down and led to destruction. Thus, de-molding of the device had to be conducted carefully.

In contrast to the valve membrane, the actuation membrane was, subsequently to the casting process, bonded to the valve body. Since its deflection was small in comparison to the valve membrane's expansion the resulting stress exposed to the bond was also small. The achievable bonding strength was hence considered to be sufficient. The actuation membrane itself was produced by spinning liquid PDMS onto a PMMA plate and subsequently curing at $70\,^{\circ}$C. Due to the small deflection and large diameter the thickness
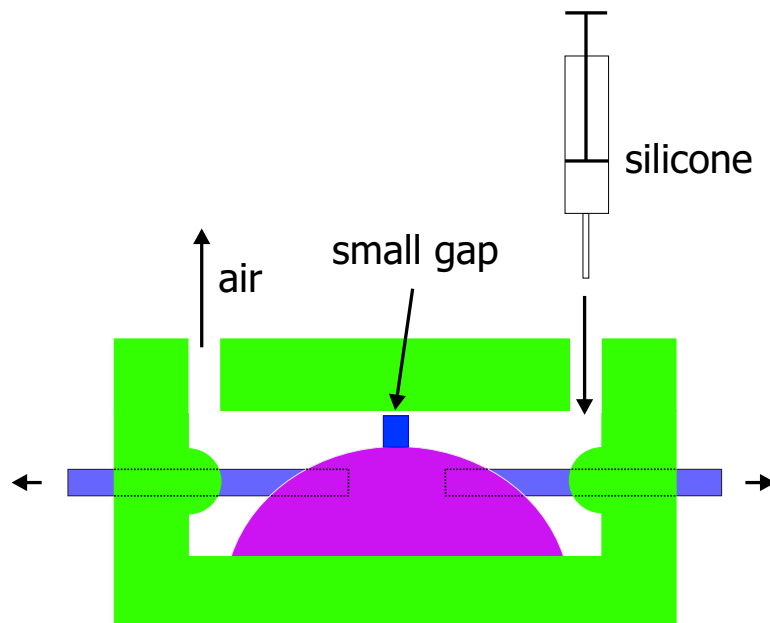
Figure 4.3: Simple fabrication process for silicone valve. The small gap between the pin and the top cover represents the thickness of the valve membrane. To define the gap, two methods were applied as specified in the text. While the lateral pins created the filling openings an o-ring established an annual groove around the valve body.

of the actuation membrane was not critical and was chosen to be ≈30 μm, which allowed easy handling. To join membrane and valve body, a plasma bonding (as described in Ch. (7)) was used. The depicted transmission opening (Fig. (4.1)), which was a result of the valve body's wall thickness, connected valve chamber and valve membrane and was necessary to avoid deflection of the valve body. Since the hydraulic pressure inside the valve chamber also acts on the valve body, and, additionally, the surface of the valve chamber is large in comparison to the area of the valve membrane, a small deflection of the valve body 'consumes' a relatively large displaced volume. The walls of the valve body therefore were thick in comparison to the membrane thickness. A tight fit of the valve inside a rigid structure to minimize any deflection of the valve body has to be avoided for the benefit of possible thermal expansion.

As mentioned above, the cavity is filled with an incompressible liquid that transduces the action of the actuation membrane to the valve membrane. Filling the cavity without encapsulating air bubbles constitutes another major challenge of this project. Fig. (4.6) shows a cast valve fabricated with the described mold. Two side holes allowed manual filling with a syringe or filling by immersing the valve into a container that was entirely
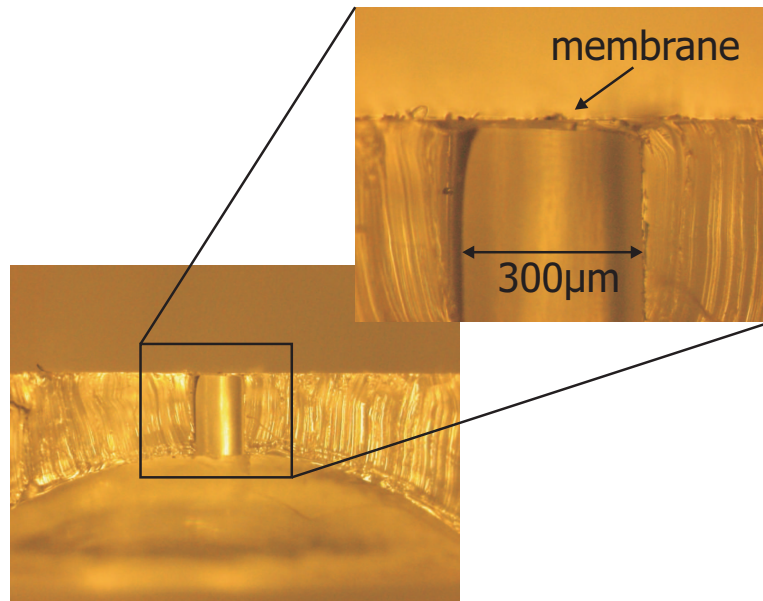
Figure 4.4: By using a flat-ended pin as casting core, a thin membrane could be fabricated using a single cast step.
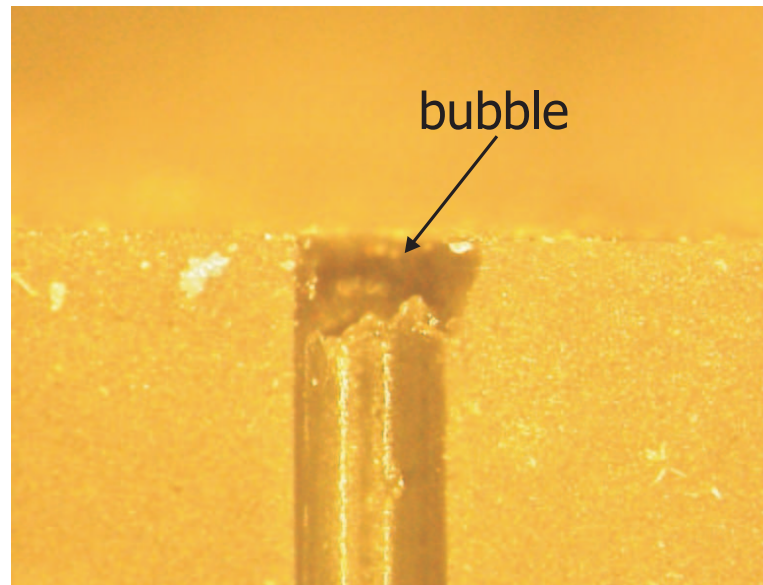
Figure 4.5: Encapsulated air led to bubbles, so called bubbles, inside the valve body material and led to failure of the casting process.

filled with silicone oil. The latter method could be supported by stirring and applying ultrasound to the liquid and offers the potential for an automated filling approach. An o-ring was used so seal the side holes and could

be mounted while the valve still was covered with liquid to avoid any intake of air. This method represents an effective filling approach and addresses the simplicity of the fabrication process. Cured silicone gel as transmission medium, as mentioned in [57], was considered but turned out to be too tough for deflection.
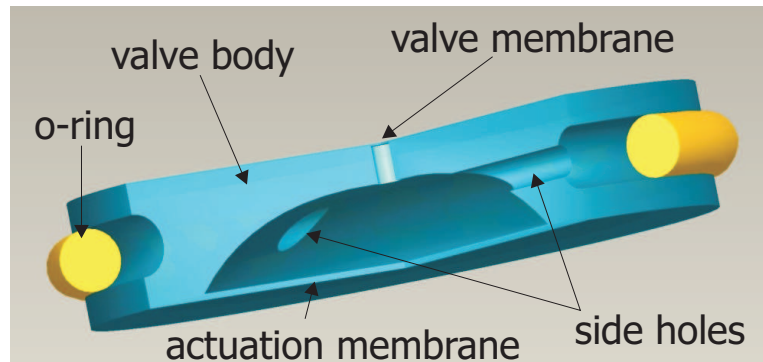
Figure 4.6: Two side holes allowed to fill the cast valve body with attached actuation membrane. Immersing the device enabled bubble free filling and subsequent mounting an o-ring sealed the chamber and prevented air to be intaken.

To operate the valve, it has to be connected to an actuator and a structure that contains the microchannel. The idea is to insert the silicone element into a multilayer device as described further below.

4.5 Experiments

For testing the valve, a setup was built that was housing the valve body as PDMS inlay and additionally contained the piezo disk bender and a microchannel. Actuating the piezo induces the valve membrane to expand into the channel and seal it. Similar to the assembly of the micropump described in Ch. (3), a multi-layer structure was fabricated into which the valve body was integrated. The bottom layer contained the piezo actuator that was sealed and insulated by a PDMS membrane, as depicted in Fig. (4.7). Fig. (4.8) shows the middle layer that was mounted onto the bottom layer and that contained a 10 mm center hole to house the valve body. Into the top layer, a channel with hemispherical cross section was machined. This allowed the expanding valve membrane to entirely seal the channel (see Fig. (4.9)). An assembled prototype of the valve is depicted in Fig. (4.10).

To estimate the deflection of the valve membrane depending on the applied pressure, a test valve without actuation membrane was used, as depicted in Fig. (4.11). Pneumatic pressure is applied to the valve chamber
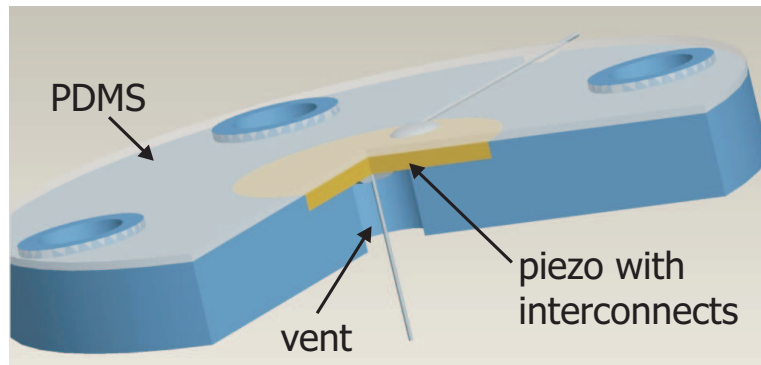
Figure 4.7: Similar to the micropump described in Ch. (3), the bottom layer contained the disk bender and was fitted with a thin PDMS layer that was cast onto the bottom layer's surface. The thickness was, again, determined by annular elevations around the screw holes. The PDMS ensured proper sealing of the valve body and insulation of the piezo.
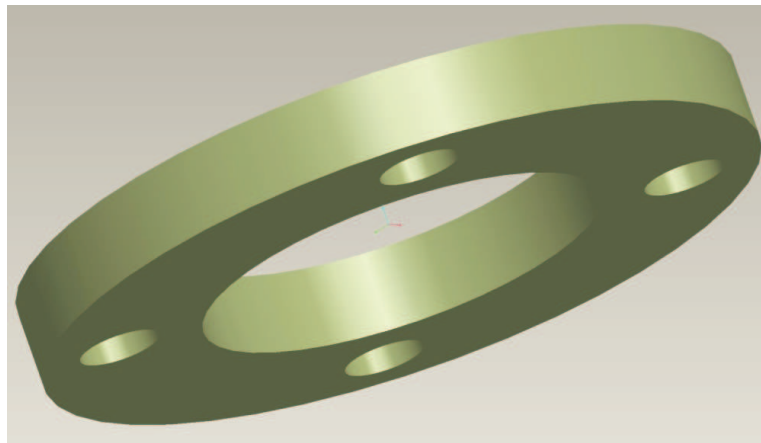
Figure 4.8: The middle layer contains a center hole that matches the dimensions of the valve body.

to deflect the membrane. Simultaneously, liquid flows through a microchannel that is fabricated into the top part of the holder while the flow rate is determined using the principle described in Ch. (2).

4.6 Preliminary Results and Conclusion

In the course of the project, only preliminary measurements could be conducted giving an estimation of the achievable membrane deflection depending on the applied hydraulic pressure. Even though a complete working device can not been shown at this point in time, the measurements show
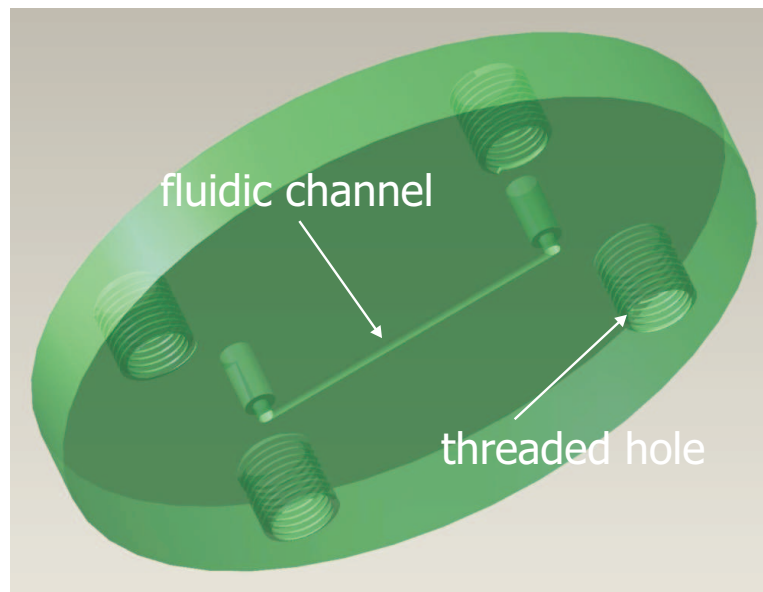
Figure 4.9: A microchannel was machined into the top layer and allowed the valve membrane to expand. To ensure proper sealing of the channel, its cross-sectional geometry was hemispherical. The threaded holes furthermore allowed easy assembly of the three layers using screws.
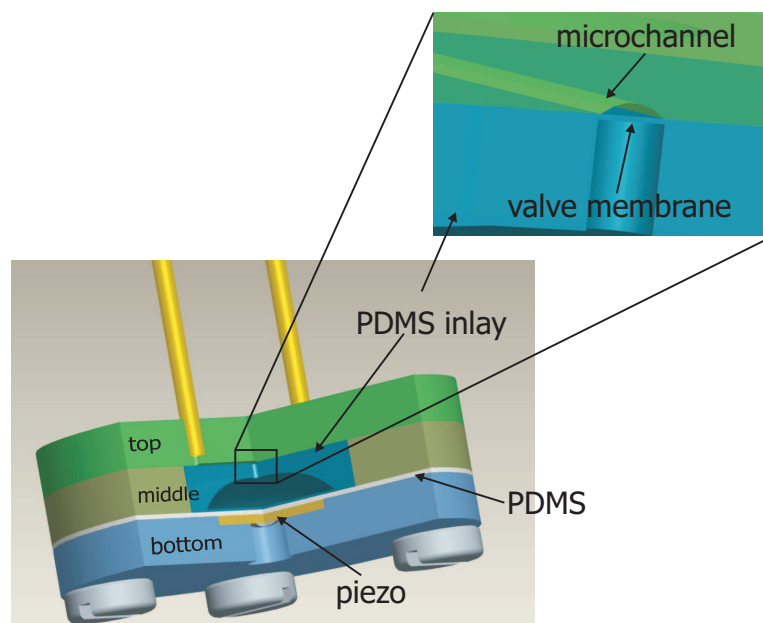
Figure 4.10: Fully assembled test setup for the active valve approach.
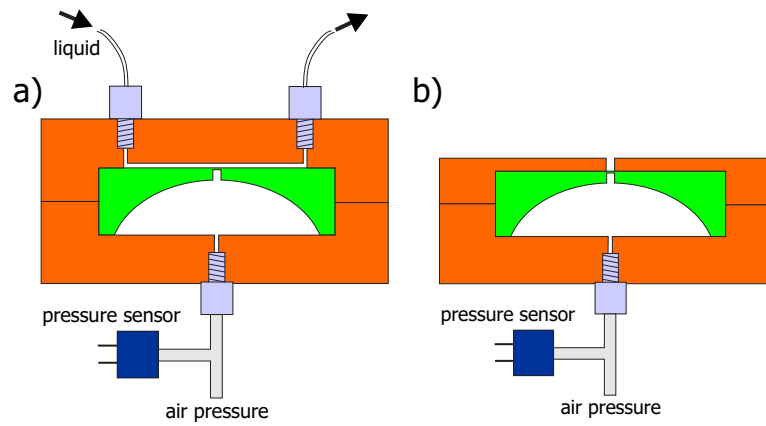
Figure 4.11: Test setups for determination of the flow rate (a) and membrane deflection (b) vs. applied pneumatic pressure.

promising results and prove the concept of the design. Fig. (4.12) shows the flow rate decreasing with increasing pneumatic pressure. A complete blocking of the channel could first be achieved using a pressure of 1.45 bar. This pressure cannot be generated using the designated piezo elements. Hence, further decrease of the valve membrane thickness is necessary. Another option is a wider channel or a channel containing a local recess.
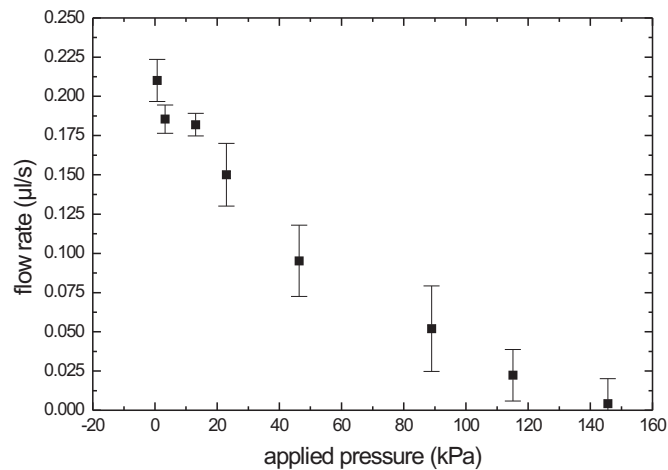
Figure 4.12: With increasing pneumatic pressure, the valve membrane expands and closes the channel successively. However, a pressure of 1.45 bar was necessary to close the valve and completely stop the flow.

Although the project could not be concluded, an active valve was designed that has the capability of direct integration of multilayer devices. The focus was put on simplification of the fabrication process, which was achieved using a one-step casting process in combination with a simple bonding method. Furthermore, an approach was developed allowing bubble-free filling of a closed chamber that represents a major problem in microfluidics.

4.7 Outlook

The proof of the working principle of the presented active valve approach is the base for further experiments. In this context, the novel filling attempt represents an important step towards a discrete device including actuator, valve body and microchannel. Subsequently, the combination with other elements to a more complex system will be performed to investigate its amenability for higher integration.

In analogy to a proportional valve, this active valve solution allows continuous closing, which means that the hydraulic resistance can be increased until the valve is completely closed. This will allow enhanced flow control in microfluidic systems and represents a major improvement of actively controlled lab-on-a-chip devices. Thus, future investigations will also focus on this challenge.

Chapter 5

Micro-optical elements

5.1 Introduction to Optical Waveguides

5.1.1 Basics

When light travels between two materials with different refractive indices, the beam is refracted due to Snell's law [59]:

$$n_1 \sin \theta_1 = n_2 \sin \theta_2, \tag{5.1}$$

with θ_1 the incident and θ_2 the refraction angle of the refracted beam and n_1, n_2 the refractive indices of the different materials.
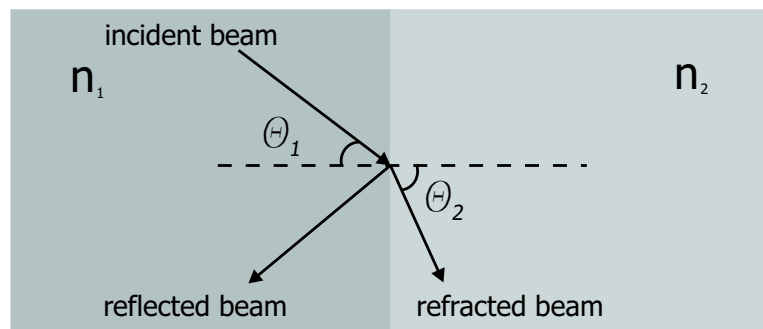
Figure 5.1: Behavior of light at the interface between two media of different refractive indices. If $n_1 < n_2$, the incident beam is refracted into the optical denser material. If $n_1 > n_2$ and θ is larger than the critical angle, the beam is reflected back.

When moving from a dense to a less dense medium (i.e. $n_1 > n_2$), it is easily verified that the above equation has no solution when θ_1 exceeds a value known as the critical angle θ_c.

The critical angle and Snell's law further determine the max. incident angle θ_{max} at which light can be coupled into a fiber to ensure total in-
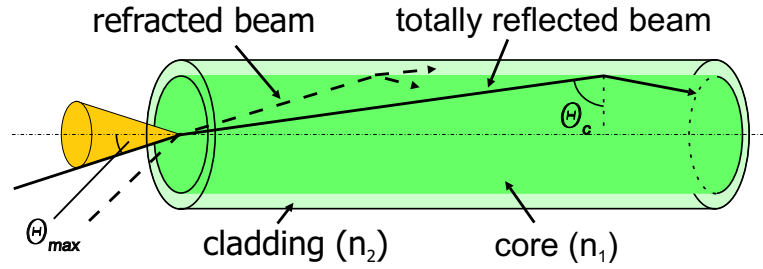
Figure 5.2: The critical angle that results from the refractive index difference of the core and cladding of an optical fiber determines the maximum incident angle, which with light can be coupled into the fiber to satisfy the conditions for total inner reflection.

ner reflection and thereby waveguiding properties, the so called numerical aperture, as illustrated in Fig. (5.2).

The critical angle θ_c is defined as

$$\theta_c = \arcsin \frac{n_2}{n_1}, \tag{5.2}$$

with n_1 the refractive index of the core and n_2 the refractive index of the cladding.

Using Eq. (5.1) and Eq. (5.2) together with geometrical relations, the numerical aperture of an optical fiber can be derived to be [59]:

$$N.A. \equiv n_0 \sin \theta_a = n_1 \cos \theta_c = \sqrt{n_1^2 - n_2^2}. \tag{5.3}$$

Above, the waveguiding properties have been explained by means of an optical fiber. To apply the principle to the area of microtechnology, planar waveguides were developed that can be integrated into microdevices and be fabricated using MEMS technologies. Fig. (5.3) shows schematically three different principles of planar waveguides.

5.1.2   Losses in Waveguides

Propagation of light in waveguides is always accompanied by losses. These losses can be grouped into intrinsic and extrinsic losses, respectively. Extrinsic losses are, for instance, inhomogeneities or geometrical effects. Inhomogeneities that are considerably larger than the wavelength of the propagating light can, for example, originate from the fabrication process. Buckling and bending with small radii, on the other hand, can lead to failure since the conditions for total inner reflection are not accomplished anymore. Losses due to inadequate coupling, maladjusted numerical apertures and reflections at phase boundaries are also among the extrinsic losses.

Intrinsic losses are caused by absorption in the core material, impurity or inhomogeneities that are smaller than the wavelength of the propagated
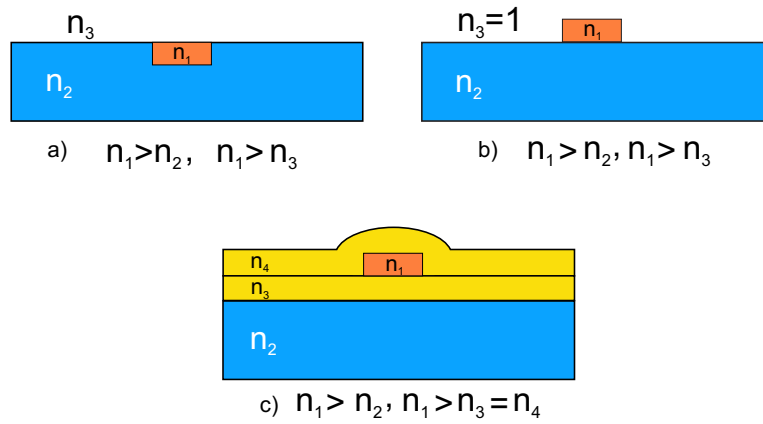
Figure 5.3: schematic cross-sectional view of planar waveguides: a) embedded, b) ridge and c) buried channel waveguide. To ensure waveguiding properties, the waveguide's core has to have a higher refractive index that the surrounding material.
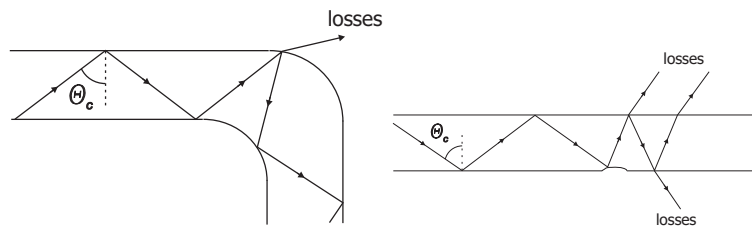
Figure 5.4: Losses occurring an a curved waveguide (left) and losses due to micro defects or roughness at the waveguide surface (right).

light. To describe the losses quantitatively, for waveguides an absorption coefficient is defined in dB:

$$\alpha_{dB} = 10 \log \left(\frac{P_{in}}{P_{out}} \right),$$ (5.4)

with P_{in} the incoupled optical power and P_{out} the outcoupled optical power.

5.1.3 Taper
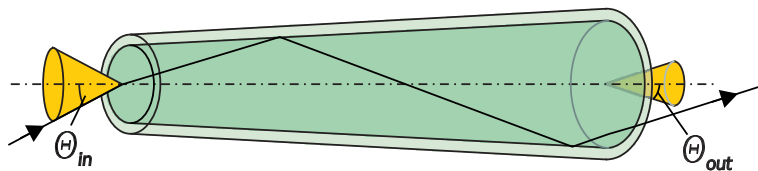
Figure 5.5: Working principle of a taper

In Fig. (5.5) a conical fiber is shown. Similar to a straight fiber, an incident beam is refracted at the phase boundary. Following the propagation inside the conical fiber, the angle with which the ray is reflected becomes smaller after every reflection and results in a collimated beam. Consequently, the input and output numerical apertures are different.

If r_{in} is the smaller radius at the input and r_{out} the larger radius at the output, we can assume [60]:

$$r_{in}^2 \sin^2 \theta_{in} = r_{out}^2 \sin^2 \theta_{out} \Leftrightarrow \sin \theta_{out} = \frac{d_{in}}{d_{out}} \sin \theta_{in} \qquad (5.5)$$

and the numerical aperture:

$$N.A._{out} = \frac{d_{in}}{d_{out}} N.A._{in}. \qquad (5.6)$$

Important parameters for the design of a tapered fiber or waveguide are the minimum length $L_{taper,min}$ and the taper angle Ω. In the literature, a maximum angle of 2° is described [61]. For linear tapers, the minimum length can be derived from

$$L_{taper,min} = \frac{r_{in} - r_{out}}{\tan \Omega}. \qquad (5.7)$$

Apart from linear tapers, various geometries for different applications were developed, as described in more detail in [61].

5.2 Aim of Integrated Optical Elements

Bio-chemical microsystems usually contain fluidic and often optical networks. In particular, fluorescence measurements and absorbance detection play a great role. The fluidic network, for instance, allows transport and mixing or even reactions of liquids. The optical network consists of waveguides that guide the light to areas on the chip where detection takes place.

One example are absorbance measurements where waveguides shine the light into an absorbance channel. The not absorbed fraction is coupled out on the opposite channel side and is guided to the detector.

Fig. (5.6) shows the design of a single absorbance cell of a microdevice. The cell consists of a microchannel and two oppositely positioned waveguides. To couple light from an external light source into the waveguides waveguide-to-fiber couplers were used [62].

Light is coupled into the channel and the beam spreads over the channel before the light reaches the second waveguide at the detection side. It is obvious that just a fraction of the light can be absorbed by the second waveguide and therefore be used for detection.
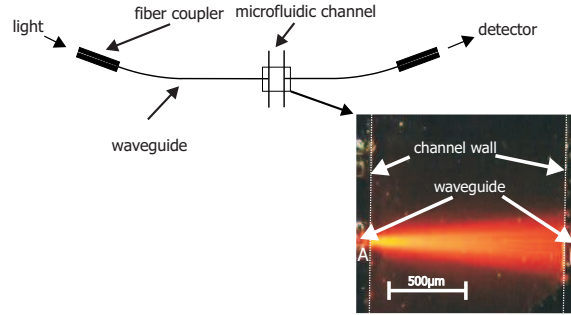
Figure 5.6: Design of a micro absorbance cell. The inset visualizes spreading of the light over the fluidic channel and shows that only a fraction of the light is coupled into the waveguide on the detection side.

Integrated waveguides combined with microfluidic channels offer the possibility of measuring the absorbance along a channel segment. The absorbance is proportional to the optical pathlength in the absorbance channel, as will be discussed in more detail later. Hence, increasing the sensitivity in absorbance measurements was in the past mainly done by increasing the optical path length [62, 63]. However, sensitivity is not the only important factor for detection but has to be seen in context with the signal-to-noise-ratio (SNR).

The improvement of the coupling efficiency in this work is done by an integration of optical elements, namely collimators and 2D-lenses, at the face of the individual waveguides.

5.3 Theory

A common model for the absorption of light is the assumption that the absorption is caused by the matter inside the medium and depends on the concentration c of the absorptive matter and the path length b through the medium. The relation between the absorbance and the irradiances is given by Lambert Beer's law [64]:

$$\mathrm{d}I = -aI\mathrm{d}b \Rightarrow \int_{I_0}^{I} \frac{\mathrm{d}I}{I} = -\int_0^b a\mathrm{d}b \Rightarrow \ln I - \ln I_0 = \ln \frac{I}{I_0} = -ab \quad (5.8)$$

$$I(b) = I_0 e^{-ab} = I_0 e^{-c\sigma b} \tag{5.9}$$

$$A = \log \frac{I_0}{I} = \varepsilon bc, \tag{5.10}$$

with I_0 the initial irradiance, I the irradiance after absorption, a = absorption coefficient, c = concentration, σ = cross sectional area, ε = molar absorption coefficient, b optical path length.

Eq. (5.10) leads to the conclusion that the sensitivity of a detection can be increased by an increase of the optical path length. The absorption, however, is calculated from the measured irradiance I and the reference irradiance I_0. To estimate the signal-to-noise-ratio, error propagation can be used that determines the variation of the baseline signal (i.e. the noise):

$$\sigma_A^2 = \sigma_I^2 \left(\frac{\partial A}{\partial I} \right)^2 + \sigma_{I_0}^2 \left(\frac{\partial A}{\partial I_0} \right)^2, \tag{5.11}$$

with σ_I and σ_{I_0} the noise of the measured irradiances I and I_0.

Eq. (5.11) leads to

$$\sigma_A = \Delta A = \frac{1}{\ln 10} \sqrt{\left(\frac{\sigma_I^2}{I^2} + \frac{\sigma_{I_0}^2}{I_0^2} \right)} \tag{5.12}$$

with σ_A the standard deviation, which, in absorption units, equals ΔA.

Considering equation Eq. (5.12) shows that the transmitted irradiance (I) is inversely proportional to the standard deviation of the baseline signal whereas the noise (σ_I) and the standard deviation show direct proportionality.

The SNR expressed in absorption units, $A/\Delta A$, can now be found from Eq. (5.10) and Eq. (5.12) to be [64–66]:

$$\frac{A}{\Delta A} = \varepsilon b c \ln 10 \sqrt{\left(\frac{\sigma_I}{I} \right)^2 + \left(\frac{\sigma_{I_0}}{I_0} \right)^2}. \tag{5.13}$$

When dealing with low concentrations we can further assume

$$I \approx I_0, \tag{5.14}$$

which simplifies equation Eq. (5.13) to

$$\frac{A}{\Delta A} = \sqrt{2} \varepsilon b c \ln 10 \frac{I}{\Delta I}. \tag{5.15}$$

For high concentrations we can assume that $I \ll I_0$, which would eliminate the factor of $\sqrt{2}$ in Eq. (5.15) and result in a even more simplified equation [65].

From equation Eq. (5.13) it can be derived that a reduction in the relative error of the measured light intensities ($\Delta I/I$ and $\Delta I_0/I_0$) is equally important as an increase in the sensitivity (ϵb) in terms of SNR.

While, on the on hand, the absorption length should be large, optimizing the light propagation and minimizing the losses, on the other hand, is vital to be able to determine low sample concentrations.

5.4   Design and Fabrication

To optimize the guidance of light three different approaches were examined.

In the first approach, microlenses were integrated at the interfaces waveguide-channel and channel-waveguide as shown in Fig. (5.7)a). The aim is to focus the light and thereby minimize spreading of light. While in the second attempt a tapered waveguide is added to the straight part to collimate the light and to improve the coupling into the channel (Fig. (5.7)b), a third approach combines both taper and lens (Fig. (5.7)c).
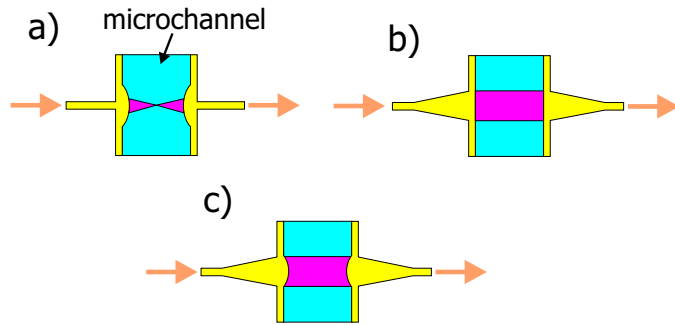
Figure 5.7: Sketch of three methods to optimize the light guidance: a) integrated microlenses, b) integrated taper, c) combination of integrated lenses and tapers

The design parameters for the lens are its radius R and the length of the lens-segment $l_{segment}$, as illustrated in Fig. (5.8). To minimize the influence of the protruding lens on the flow protruding, namely causing velocity changes, the lens segment should be as small as possible. While the lens radius is determined by the refractive indices of the used materials and the desired focal length f_i, the segment length can be obtained from the critical angle of the waveguide and the width of the channel wall. For symmetrical reasons, the lenses were designed to focus the light in the middle of the fluidic channel. Assuming a refractive index of $n_{liquid} = 1.33$ for aqueous solutions the lens radius can be calculated:

$$R = \frac{f_i(n_{liquid} - n_{SU-8})}{n_{liquid}} \tag{5.16}$$

Assuming further a refractive index of $n_{SU-8} = 1.59$ for the waveguide material and $n_{air} = 1$ for air as the lateral cladding, the critical angle can be calculated to be $36.15\,^{\circ}$. Accordingly, using geometric relations, the minimum segment length is approximately $105\,\mu m$ (see Fig. (5.8)). Consequently, a minimum channel width of $520\,\mu m$ can be derived from Eq. (5.16) (assuming the focal point in the middle of the channel). Tab. (5.4) gives an overview of the fabricated channel widths and the corresponding lens radii
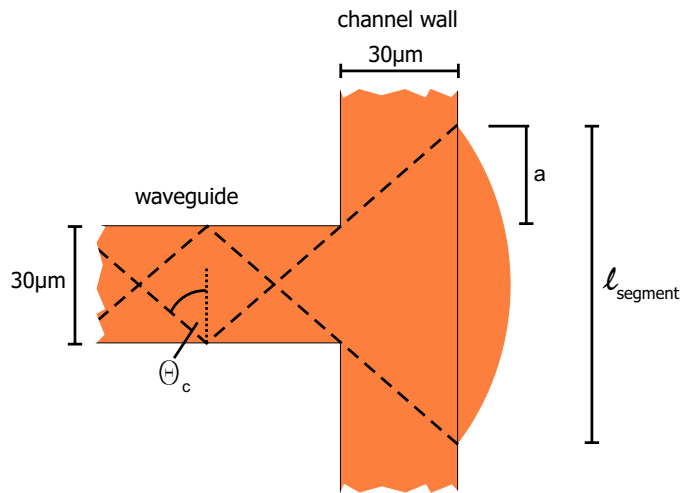
Figure 5.8: Illustration of the design parameters for an integrated lens
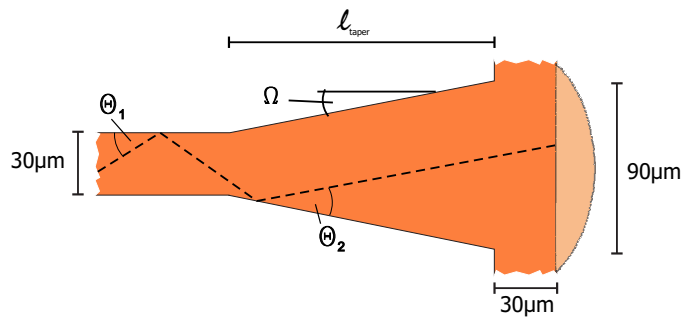
Figure 5.9: Illustration of the design parameters for a tapered waveguide. The indicated lens section in with its $105\,\mu$m slightly larger than the taper to collect all light exiting the taper.

used in this work. For comparable results, the segment length was kept constant for all channel widths.

The integrated linear taper enlarged the $30\,\mu$m wide straight waveguide to $90\,\mu$m in width at a lope angle of $2\,°$, which further allowed to combine lens and taper ensuring all collimated light propagating through the $105\,\mu$m wide lens-segment (see also Fig. (5.9)).

To investigate the influence of the channel width and the different geometries four testchips as seen in Fig. (5.10) were designed. While chip 1-3 contained the described integrated elements, as a reference chip 4 did not include any additional structures.

The channel width on each chip varied from $400\,\mu$m to $4000\,\mu$m. Three identical absorbance cells constitute a group at the same channel width to allow for multiple measurements and to compensate for tolerances. Addi-

channel width [μm]	lens radius [μm]
400	40,6
800	81,2
1000	101,5
1200	121,8
1600	162,4
2000	203
3000	304,5
4000	406

Table 5.1: Channel widths and corresponding lens radii. Although the minimum channel width was $520\,\mu$m, $400\,\mu$m wide channels were fabricated additionally to investigate the influence of the optical elements at small optical path lengths.

tionally, each chip contained two reference waveguides.
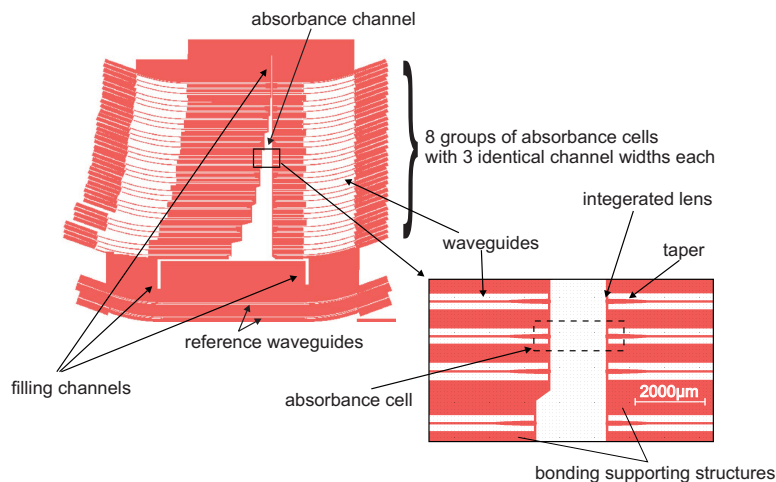
Figure 5.10: Design of the test-chip. It contains 24 absorbance cells with 8 different channel widths and two reference waveguides.

The fabrication of the chips was done by a single step lithographic process [67]. Wet oxidizing 4 inch wafers 16 hours at 1100°C resulted in an oxide layer of approximately $2.5\,\mu$m thickness, which served as a bottom cladding for the waveguides. Subsequently the wafers were coated with SU-8-2075. To be able to insert a fiber later into the coupling structures, while also considering tolerances of the film thickness, the thickness of the SU-8 layer had to be in the range of 90-100 μm. According to its data sheet [68] the resist was spun on with 1800 rpm using a spread cycle at 500 rpm. After spinning, the wafers were pre-baked at 95°C for 25 minutes with an overall ramp time of 8 min and an intermediate temperature step at 60°C for 5 min.
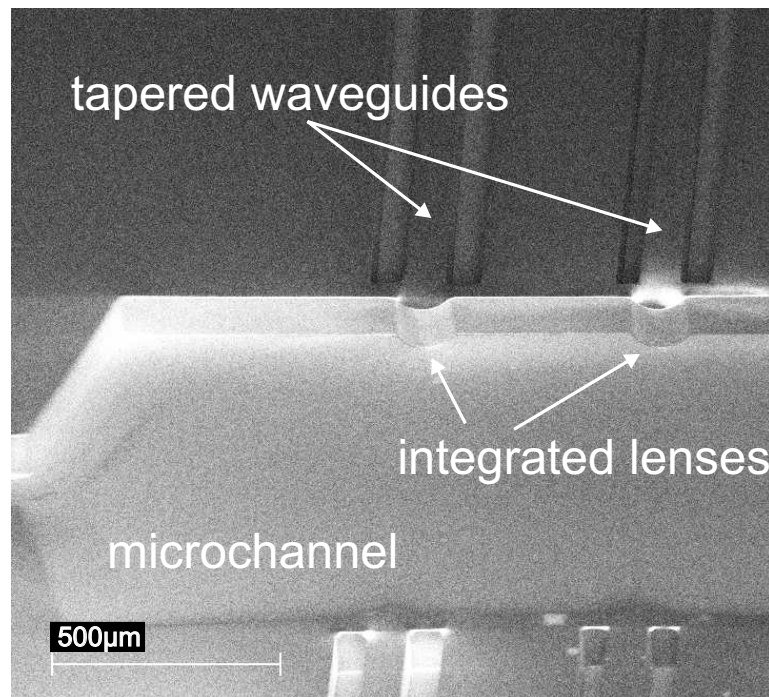
Figure 5.11: SEM picture of a microstructure for absorbance measurements fabricated by structuring a single SU-8 layer.

Afterwards, the resist was multi exposed five times for $20\,\mathrm{s}$ each with $10\,\mathrm{s}$ intermediate waiting time. A following soft-bake had the same settings as the pre-bake. Finally, the wafers were developed in a two step development bath with $8\,\mathrm{min}$ duration each. The wafers were not hardbaked during the processing.

Fig. (5.11) shows a SEM picture of two absorbance cells with integrated lenses and tapers. The individual chips were sealed using the adhesive bonding approach described in Ch. (7).

5.5 Simulations

To be able to evaluate how the integration of the lenses and the tapered waveguides affects the system, the different geometries were simulated. A simple BPM (Beam Propagation Method) model was developed using the program Prometheus (BBV Software bv, Enschede, The Netherlands). The model consisted of two symmetric, $15000\,\mu\mathrm{m}$ long waveguides ($100\,\mu\mathrm{m}$ high and $30\,\mu\mathrm{m}$ wide) with a refractive index of $n = 1.59$. Between these waveguides a rectangle with a refractive index of $n = 1.33$ was placed that represented the fluidic channel. The width of the rectangle was varied from $400\,\mu\mathrm{m}$ up to $4000\,\mu\mathrm{m}$ according to the different channel widths of the real

chip.

The program calculated the output field using a Gaussian-shaped E-field as a starting condition. Fig. (5.12) shows a view of a calculated field and a sketch of the simulated geometry.
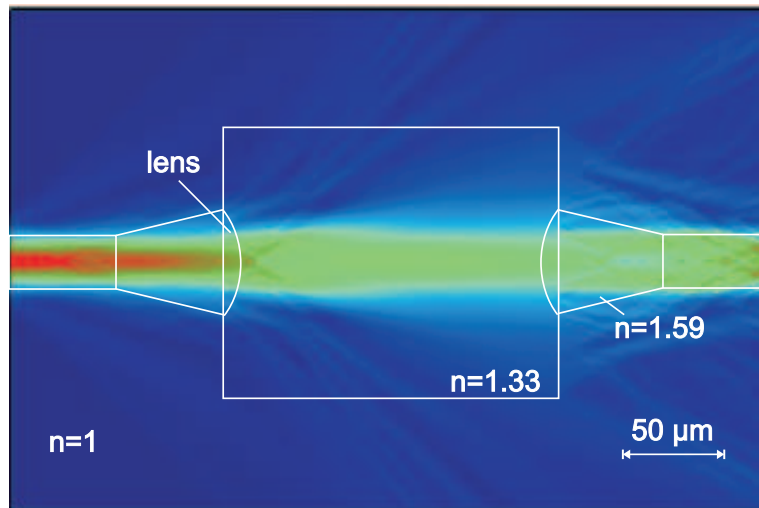
Figure 5.12: Visualization of a simulated field and drawing of the simulated geometry using the BPM-software Prometheus.

The simulated end-fields for the four considered cases can be seen in the graph of Fig. (5.13). The curves show the calculated distribution of the power over the width of the outgoing waveguide. It turned out that the structure with the integrated lenses had the highest peak. The combination of taper and lens had two peaks just below the lens peak. While structures without supporting geometry had one peak below the lens-taper combination the taper-only waveguide delivered four peaks at even lower level.

To have the ability to compare the overall irradiance the end-field function has to be integrated over the waveguide width.

Fig. (5.14) shows the results of all integrated end-fields for different channel widths and the different designs. One can see that the graphs for the structure with the straight waveguide, the tapered waveguide, and the waveguide with integrated lenses have the same shape and similar magnitudes. Significantly lower losses are seen for the structure with combination of taper and lens. Its magnitude is on average half as high as the other three curves at channel widths wider than $1000\,\mu$m. The difference at shorter channel widths is smaller.

It has to be noted that some limitations were set to simplify the model. Simulation of multiple modes require a lot of computional power and the applied Gaussian field can therefore just be seen as an approximation of the incident beam.
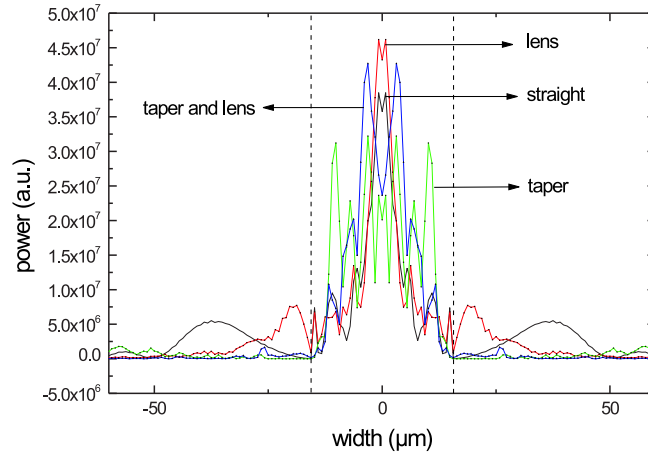
Figure 5.13: Simulated end-fields for the different integrated structures at a 1000 μm wide channel
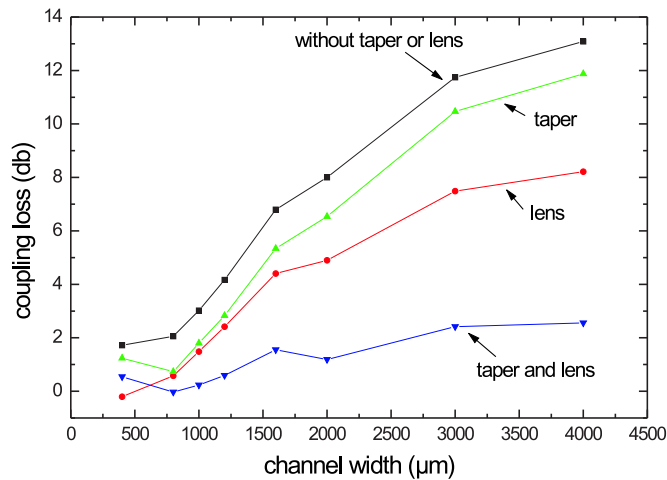
Figure 5.14: The end-fields of all simulated structures were integrated and the coupling losses were calculated

5.6 Measurements

Light was directly coupled into an optical fiber from a temperature controlled diode laser (10 mW, λ_{peak}=635 nm). As mentioned earlier, the fiber was inserted manually into the chip using coupling structures. As detector, a

photodiode (HP81533B in combination with HP8153A) was used, which was also connected to the chip through a fiber. The fibers were inserted pairwise into the different couplers that belonged to the individual absorbance cells. The power of the emitted light was then measured for $10\,\mathrm{s}$ at a sample rate of $250\,s^{-1}$. As mentioned, each chip contained three identical absorbance cells for each specific channel width, thus the measurements of the set were averaged and the standard deviation was calculated. Similarly to the propagation losses defined by Eq. (5.4), the coupling losses over the fluidic channel can be determined by

$$\alpha_{dB} = 10 \log \left(\frac{P_{\text{reference}}}{P_{\text{absorption}}} \right). \tag{5.17}$$

As liquid inside the channel DI-water and $50\,\mu\mathrm{M}$ bromothymol blue solution (absorbance peak $\approx$ at $610\,\mathrm{nm}$) was used.

5.7 Results and Discussion

The aim of the experiments was to be able to reveal the affect of integrated optical elements on the efficiency of absorbance measurements. Fig. (5.15) shows the coupling losses of the different principles for channel widths between 400 - 4000 μm. Increasing the channel width leads to a rapid rise in losses for the structures without additional beam shaping elements, as well as for those with integrated lens or taper. Only the combination of integrated tapers and lenses ensured the coupling loss of these structures to remain at a comparatively low level. From a channel width of $1200\,\mu$m a continuing order in coupling losses for the different principles can be found, which is kept up to the $4000\,\mu$m wide channel. It emphasizes, that the structure with the combination of elements has on average a lower coupling loss of about $4\,\mathrm{dB}$ between channel widths of $800\,\mu$m and $3000\,\mu$m, which corresponds to more than a doubling in intensity. The graphs for the structures with integrated taper and for those with integrated lenses show a similar characteristic, the former one, however, has a $2\,\mathrm{dB}$ lower coupling loss.

The effects of the different integrated elements on beam shaping are depicted in Fig. (5.16). The light inside the channel was visualized by a fluorescence dye (bodipy650/665-x, $75\,\mu$M). Clearly, the collimating properties of the tapered waveguide can be observed in Fig. (5.16)b.

Comparing the results from the simulations it can be seen that the order of the simulated geometries and the real structures is the same. There are, however, quantitative differences. This can be explained by the limitations in the simulation model as mentioned earlier.

Apart from using the described optical elements to increase the transduced optical power, this approach was also employed in a micro flow cytometer collecting scattered light [69].
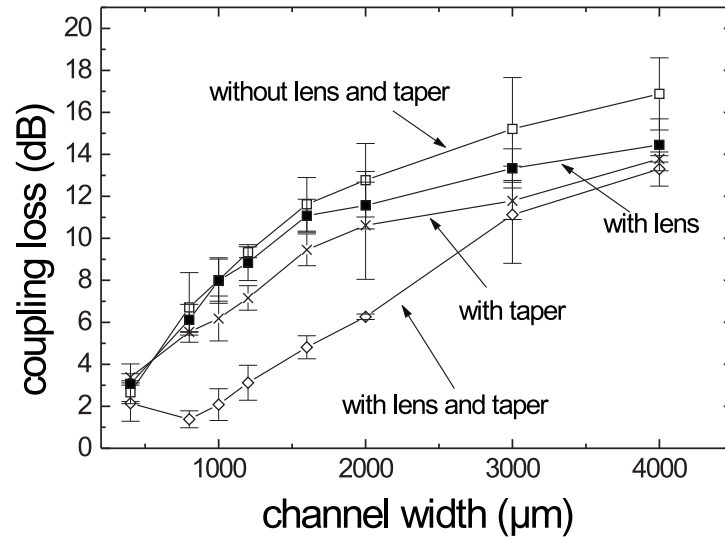
Figure 5.15: The coupling losses were calculated using the reference waveguides and equation Eq. (5.17). In average the structures with integrated taper-lens combination showed $3\,\mathrm{dB}$ lower coupling losses.

5.8 Outlook

The promising results presented in this chapter allow speculations on future applications using integrated beam shaping elements. The mentioned cytometer is a first example of the functionality this approach shows. Focusing of light at different focal points in laminated flow can allow distinguished detection of species and will be subject of ongoing experiments. Different taper geometries and elliptical lenses will be furthermore subject of additional research on this topic. However, deeper investigations are necessary to allow, for instance, the fabrication with alternative processes and materials.

a) without lenses and tapers

b) with taper

c) with lens

d) with combination of lenses and tapers
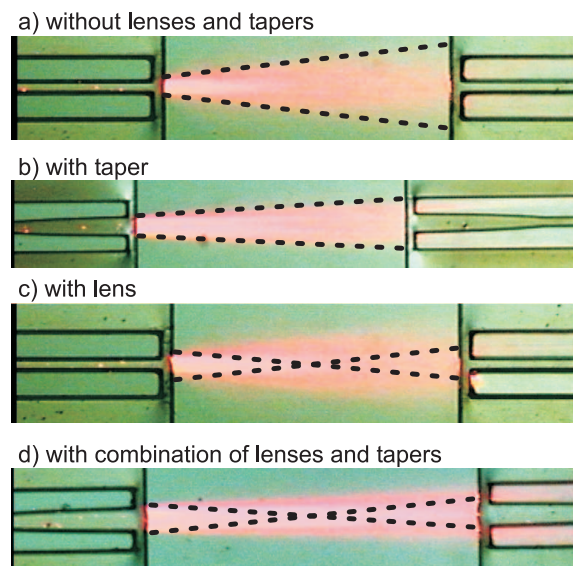
Figure 5.16: Emission patterns for (a) wave guides without lenses and tapers, (b) tapered waveguides, (c) waveguides with lenses and (d) waveguides with taper-lens combination.

Chapter 6

Direct Milling of Optical Waveguides

6.1 Introduction

Optical detection methods are widely used in miniaturized analysis systems [70]. Especially the integration of optical waveguides into microsystems allows the design and fabrication of complex and compact devices, which are, in contrast to systems that use bulk optics, robust and insensitive to vibrations [71].

Conventionally used materials for the fabrication of microsystems are glass and silicon. In this case, the microsystems are often fabricated using time consuming and expensive MEMS technology. The integration of optical components complicates the processing, since a difference in the refractive index between the waveguiding layer and the surrounding material is necessary to achieve waveguiding properties. In the case of silicon microsystems, this typically results in extra fabrications steps for the waveguide buffer and cladding layers [72].

Using polymers instead of conventional MEMS materials opens room for a variety of new fabrication methods [19, 73, 74]. Flexible fabrication methods that are often used in research laboratories include photolithography, laser machining and micromilling. Injection molding and hot embossing, on the other hand, are well known as high number production methods [75, 76]. Feature sizes in the sub-micrometer range can be achieved by injection molding, mainly limited by the accuracy of the master tool [77]. Master tools can be fabricated using a variety of different methods such as silicon micromachining or micromilling [78, 79].

It is also possible to use polymer materials to guide light within a microsystem device. For example, a high refractive index photoresist ($n = 1.59$) has first been spin-coated onto a silicon substrate with a thin oxide layer ($n_{\text{SiO}_2} = 1.46$) and then structured with a photolithography

step [80–82]. Other groups have used microchannels filled with higher refractive index materials to achieve waveguiding properties [83–85]. Using photocurable resins as the core material, however, limits the transparency of the waveguides, especially towards the UV region of the spectrum due to absorption from the added photosensitizers.

To produce microsystems with integrated optical waveguides of high transparency, we investigated several other polymer fabrication methods that do not rely on photolithography. Laser ablation offers the possibility to directly write structures into various materials. CO_2-laser machining, for instance, is a fast and powerful tool for fabrication of microfluidic devices in polymer substrates [86]. However, the achieved geometry tolerances are limited due to melting effects of the polymer. Decreasing the wavelength of the laser and using UV direct-writing of waveguides for glass or polymer substrates, on the other hand, produces better structural quality, but does not lend itself to integrate microfluidic networks.

Another versatile tool is micromilling. Micromilling can be used for direct structuring as well as for fabrication of tools for casting or molding processes [87, 88]. Although micromilling is a relatively time consuming process, its advantage lies in the high flexibility, the option to change the design rapidly and the feasibility of direct three-dimensional structuring. With respect to transparency, micromilling has the advantage of a rather broad material selection, so that a highly transparent polymer can be chosen as a basis material.

In this work, we demonstrate a novel method that combines the flexibility of micromilling with the possibility of direct fabrication of optical waveguides. A polymer with high refractive index is spin-coated onto a polymer substrate with low refractive index. Subsequently, the spin-coated layer is structured using micromilling and finally covered with another low refractive index PMMA lid.

A particular promising field for microsystems are medical applications. Here, microsystems that are portable and inexpensive enjoy a great advantage over more conventional systems in that they do not need to be used more than once. To arrive at inexpensive, one-time-use devices, high number fabrication methods and polymer materials appear to be the best strategy.

Molding techniques are considered the most suitable for high number production. However, it is not straightforward to combine the integration of microoptical components such as waveguides with the injection molding process, since the essential difference in refractive indices requires local variation of material properties. One example of varying the refractive index while using a molding technique is microtransfer molding as described by Zhao *et al.* [89] to form polymer waveguides on a silicon substrate. After curing with UV light and removing the mold, polymer of the same type was poured over the waveguides and subsequently cured to act as a cladding. The difference in refractive index was achieved by a difference in the curing

time.

As an alternative to the technique presented by Zhao *et al.*, we demonstrate a technique that allows casting of waveguides in a single step, again using polymers with different refractive indices. The PDMS mold that is used for this process can be formed from micromilled structures as well as from conventionally fabricated substrates. This process allows the integration of waveguides and microfluidics into microsystems and is suitable for high number production.

6.2 Design and Fabrication

To achieve waveguidance, the refractive index of the waveguide core has to be higher than the refractive index of the surrounding material, which acts as a cladding layer. PMMA was chosen as the substrate material, since this material is widely used in microtechnology applications due to its ease of fabrication, its favorable optical properties and the feasibility of thermal bonding [19, 22].

Onto the PMMA substrate a $90\,\mu$m thick layer of PMMA with higher refractive index was spin-coated. To modify the refractive index we doped the PMMA with styrene-acrylonitrile copolymer (SAN). This method allows the refractive index to be varied between 1.49 (100% PMMA) and 1.56 (100% SAN) ($\lambda = 632$ nm) [90]. For all fabricated devices in this work we used a ratio of 80% PMMA and 20% SAN (see Sec. (6.3)). The fabrication process is sketched out in Fig. (6.1).
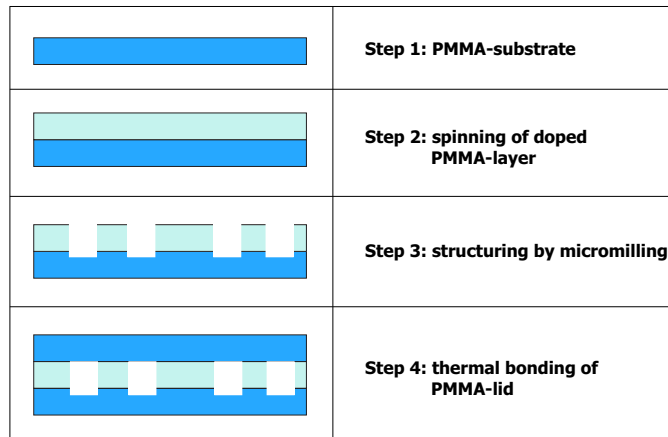
Figure 6.1: Principle of fabrication process: a) native PMMA as substrate material b) spinning a 'doped' PMMA layer with higher refractive index onto the substrate c) structuring the spun on layer by micromilling d) thermal bonding of a second native PMMA layer onto the structured layer

An alternative to 'doping' is variation of the molecular weight, which

also makes it possible to change the refractive index, albeit only between 1.47 and 1.49. However, the approach was not optimal for our purposes, because while decreasing the molecular weight leads to a higher refractive index, it also decreases the glass transition temperature (T_g). A decrease in T_g is associated with a decrease of Young's modulus, which means that the material becomes softer and yields during the milling process. In combination with the heat that is produced by the rotation of the milling tool, this results in higher surface roughness, which increases the scattering losses of the waveguides.

To investigate the optical properties of waveguides that were produced with our new methods, a test-structure was designed (see Fig. (6.2)). The
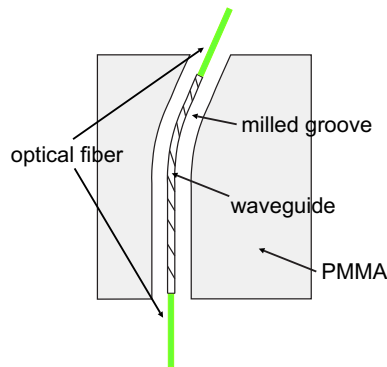
Figure 6.2:   Design of one test waveguide fabricated by micromilling. Two parallel $100\,\mu$m deep grooves are milled to obtain a waveguide.

structure consists of 5 waveguides, with different lengths ($20\,$mm, $25\,$mm, $30\,$mm, $35\,$mm, and $40\,$mm), which were fabricated by milling two parallel grooves of $100\,\mu$m depth with a distance of $100\,\mu$m using a $400\,\mu$m tool. This allows air to act as cladding at the sides of the waveguides. To avoid direct coupling of light from the input fiber into the detection fiber, the waveguides were slightly bent.

This test structure was milled into the $90\,\mu$m thick spin-coated layer of SAN-PMMA using a micro-milling machine (MPS 2000, Quantum Ltd., United Kingdom). A $100\,\mu$m groove depth ensures milling down into the cladding material and compensates for thickness variations of the core material film. Grooves that are shallower than the film thickness of the core layer would lead to leaky waveguides and therefore to an increase in propagation losses (see Fig. (6.3)).

A pressured-air turbine (Air Turbine Technology, Boca Raton, Florida 33487, USA) was used to obtain rotational speeds of approx. $40\,000\,$rpm. This ensured low surface roughnesses of the milled areas, which were determined to be less than $200\,$nm (see Fig. (6.4)). Water with a small amount of soap was applied to the working area to cool the substrate and the tool.
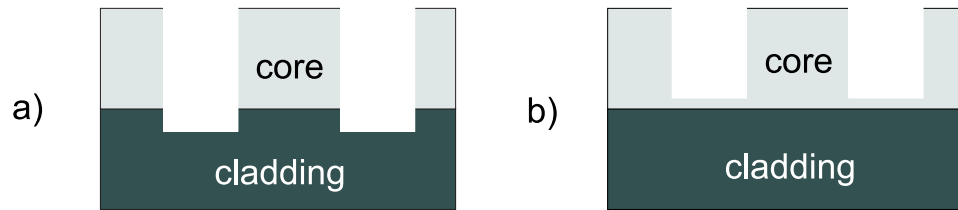
Figure 6.3: (a) Grooves deeper than the core layer's thickness ensure a waveguide surrounded by material with lower refractive index (b) Grooves shallower than the spin-coated layer thickness lead to residual material with the same refractive index as the waveguide and therefore to leaky waveguides

After fabrication, the device was placed in an ultrasonic bath for 30 min to remove small debris and burr from the milling process (Fig. (6.4) shows the edge of a milled waveguide). Optionally, a second PMMA plate can be bonded thermally to cover the milled structures.
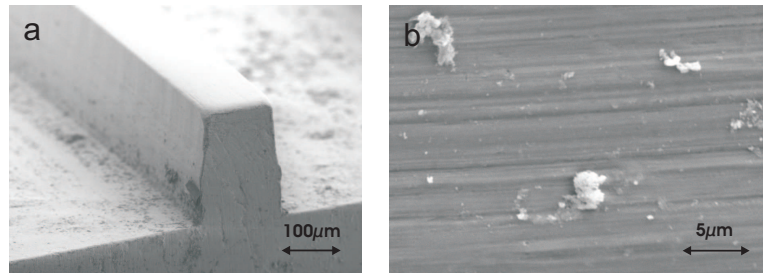
Figure 6.4: (a) SEM image of a milled waveguide, (b) SEM image of a waveguide sidewall. The roughness was estimated to be less than 200 nm.

As mentioned above, micromilling is a relatively time consuming process. As an additional process, we therefore developed a process that enabled us to cast fluidic structures and waveguides in a single fabrication step from a micromilled master (see Fig. (6.6)).

First, PDMS prepolymer was cast onto a master that contained the design as a positive structure. In this work, we used the milled devices mentioned above as a master to be able to directly compare the optical properties between two devices fabricated using these two approaches. The PDMS was then cured for 1 hour at 60 °C. To remove air bubbles, the structure and the PDMS prepolymer were placed in a vacuum chamber for 40 min before curing. Subsequently, the master was released from the cured PDMS to obtain a negative copy. Doped PMMA (80% PMMA, 20% SAN) was poured onto the PDMS copy, which was finally covered with a PMMA plate. The PMMA plate was loaded with a weight that pressed the plate against the PDMS mold, which allowed redundant doped PMMA to flow to the sides. In

our experiments, we found 700 g of weight suitable, which corresponds to approximately 5 000 Pa. Significantly lower pressures resulted in too much residual polymer and eventually in leaky waveguides. Using higher pressures (in the range of 10 000 Pa) led to deformation of the PDMS mold as well as the cast structure.

In Fig. (6.5) the cross sections of two cast waveguides can be seen. To
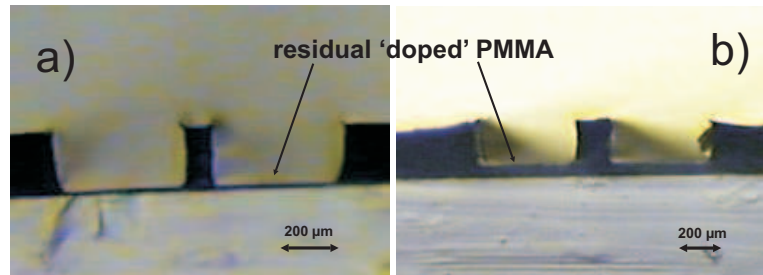
Figure 6.5: Cross sectional view of molded waveguides: different pressures during the fabrication process led to different thicknesses of the residual layer (a) 5 000 Pa, b) 1 000 Pa).

visualize the residual layer, the doped PMMA was dyed with blue ink. Using the 700 g weight, a minimum residual layer thickness of less than $10\,\mu m$ could be achieved. The setup was then left in a fume hood over night to let the solvent evaporate. At this point, we took advantage of the high gas permeability of PDMS, which allowed the solvent to evaporate through the PDMS mold. Gas bubbles generated by evaporation of the solvent, and potentially affecting the forming process, were thus avoided. Finally, the PDMS mold was released and could be reused for another casting process. If desired, a second PMMA plate can be bonded thermally onto the structured layer. The process sequence is summarized in Fig. (6.6).

6.3   Experiments

As mentioned above, to have the ability to integrate waveguides into polymer microsystems, a variation of the refractive index is required. The PMMA was doped with styrene-acrylonitrile copolymer (SAN) to vary its refractive index. Dissolving both polymers turned out to be a time consuming process. On the one hand, the solvent has to have the ability to dissolve both polymers simultaneously and equally well. On the other hand, the evaporation time should be sufficiently long to avoid orange-peel effects as also mentioned by Ramaswamy and Weber [90]. We used anisole (methyl-phenyl-ether) as the solvent, which turned out to dissolve both polymers sufficiently. Further, anisole provides good film qualities due to its relatively high boiling point $(154\,^{\circ}C)$ and the consequently long evaporation time. Using 3-methyl-2-butanone (MIBK) in combination with cyclohexanone and silicone oil, as

	Step 1: micro structuring of positive
	Step 2: casting of PDMS prepolymer onto structured substrate
	Step 3: curing of PDMS and release from positive
	Step 4: casting of polymer with high refractive index onto the PDMS negative
	Step 4: pressing low refractive index PMMA plate onto the liquid polymer using a weight
	Step 4: removing PDMS and thermal bonding of PMMA
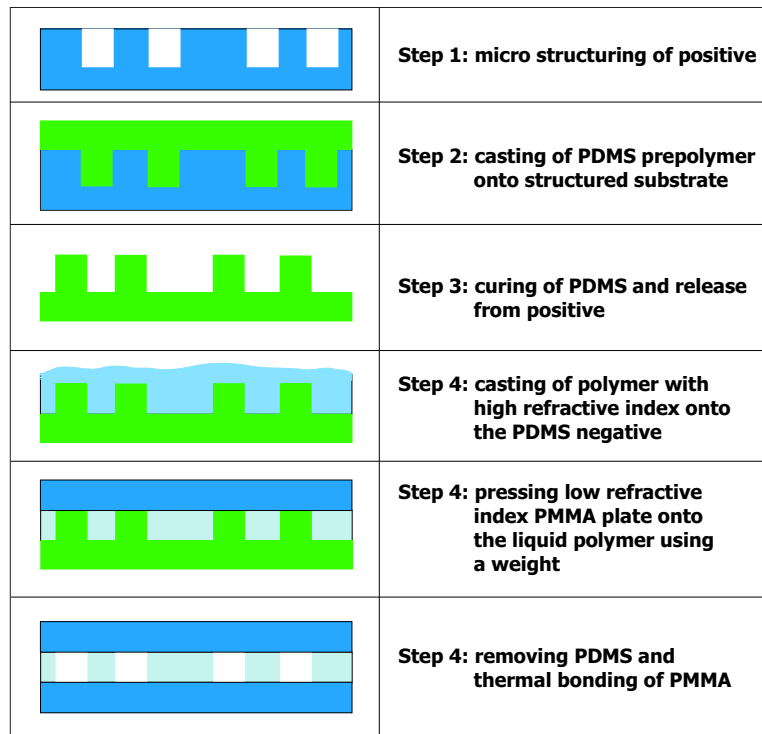
Figure 6.6: Principle of high number fabrication process: first, the desired microsystem is fabricated and a PDMS negative is obtained. A high refractive index polymer in liquid form is then used to fill the negative. This polymer bonds to a low refractive index PMMA plate. Finally a second PMMA plate can be thermally bonded onto the structure as a lid.

mentioned by Ramaswamy and Weber, was not successful for us, because the thermal bonding properties of PMMA dissolved in this solvent were poor in comparison to that dissolved in anisole.

The six different mixing ratios of PMMA and SAN that have been investigated can be seen in Tab. (6.1). To ensure that the PMMA that was used for dissolving and spin-coating was the same as the substrate material, small pellets were cut from the PMMA substrate material. SAN was purchased directly in pellet form (Kostil B366, Polymeri Europa, Italy). The different ratios of polymers were mixed by weight before $60\,\mathrm{ml}$ of solvent ($\varrho = 0.99\,\mathrm{kg/dm^3}$) were added. Mixing the components in different ratios resulted in solutions having different viscosities. A spin-coating curve was determined (Fig. (6.7)) to achieve the same film thickness for each mixture. This is important to be able to compare the different optical losses.

To determine the refractive indices, a thin layer ($\approx 4\,\mu\mathrm{m}$) of every sample was spin-coated onto a silicon wafer. After hardbaking the film, the refractive index was measured with a prism coupler (see Fig. (6.8)). Our mea-

PMMA	SAN
0%(0 g)	100%(30 g)
20%(6 g)	80%(24 g)
40%(12 g)	60%(18 g)
60%(18 g)	40%(12 g)
80%(24 g)	20%(6 g)
100%(30 g)	0%(0 g)

Table 6.1: Volume and weight mixing ratios of PMMA and SAN before dissolving in anisole

.

surements agree well with the results originally published by Ramaswamy and Weber [90]. Based on the preliminary investigations summarized above, for all further work we used PMMA slides with a refractive index of 1.484 and doped PMMA (mixing ratio 80% PMMA and 20% SAN) with a refractive index of 1.499.

To investigate the optical properties of the milled waveguides, the propagation loss was determined. Optical fibers were aligned to the waveguides using xyz-stages and were used to couple light into the waveguides and connect the device to the detector. The transmission spectrum of each waveguide was determined between 380 nm and 850 nm (Spectro 320, Instrument Systems, Munich, Germany). The spectra were then normalized with a reference spectrum of the light source and the so-called total waveguide insertion loss (a, in dB) was calculated using equation 6.1 [91]:

$$a = -10 \log \frac{P_{\text{waveguide}}}{P_{\text{reference}}}, \tag{6.1}$$

where $P_{\text{waveguide}}$ and $P_{\text{reference}}$ are the measured radiative fluxes. A linear fit of the insertion loss versus waveguide length was subsequently calculated to obtain the propagation loss (dB/cm) as a function of the wavelength.

As mentioned above, a fabrication process was developed to fabricate waveguides with an easy and rapid method. To be able to compare the propagation losses from the milled waveguides with the cast waveguides, the milled test structures were used as master tools for the PDMS mold to obtain the same geometry and roughness. After processing, the propagation losses of the cast waveguides were determined as described above.

Additionally, a set of waveguides was fabricated by micromilling grooves into a native PMMA slide, which allowed the estimation of the influence of the doped PMMA on the waveguiding properties.
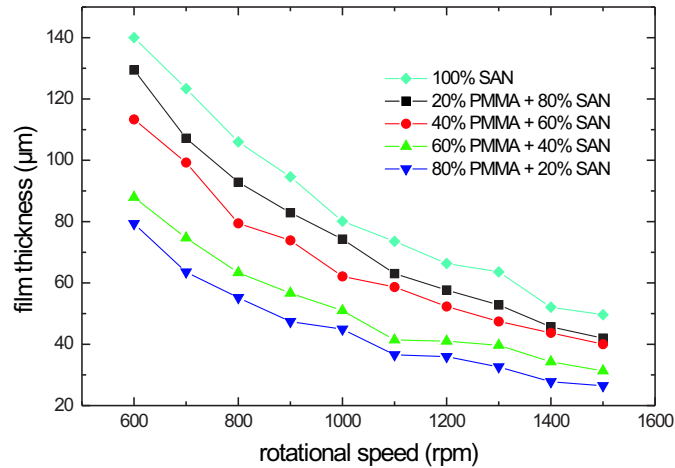
Figure 6.7: Spin-coating curves (rotational speed vs. film thickness) for the different mixing ratios of PMMA and SAN. Error bars are typically smaller than the symbol sizes.

6.4 Results and Discussion

To optimize the signal-to-noise ratio, the optical losses of the waveguides should be as small as possible. This will increase the transmittance and therefore also improve the signal-to-noise ratio. Fig. (6.9) shows the propagation losses of the three waveguide types produced by milling and casting. The waveguides that were milled into the doped PMMA show a propagation loss of around $1\,\mathrm{dB/cm}$ over a wide wavelength range, which is a good performance. At wavelengths smaller than $400\,\mathrm{nm}$ the propagation loss increases rapidly. This behavior can be explained by the different effects causing the propagation losses. While the absorbance of the core material dominates at lower wavelengths ($\lambda < 400\,\mathrm{nm}$), in higher wavelength regions ($\lambda > 400\,\mathrm{nm}$) scattering causes losses at the waveguide surface.

Scattering caused by surface roughness is a major factor when dealing with micromilled waveguides. Parameters such as feed rate, rotational speed of the tool, cooling rate, and glass transition temperature influence the outcome of the fabrication process. Fig. (6.10) visualizes the difference between uncooled processing using a high feed rate ($40\,\mathrm{mm/min}$) versus cooled machining at a lower feed rate ($15\,\mathrm{mm/min}$). Although the surface roughnesses have not been quantified in detail yet, it is possible to conclude that improved machining results are obtained when using low feed rates and cooling.

In comparison to the milled waveguides the cast waveguides show losses in the range of $1-3\,\mathrm{dB/cm}$. The difference in losses between the milled and
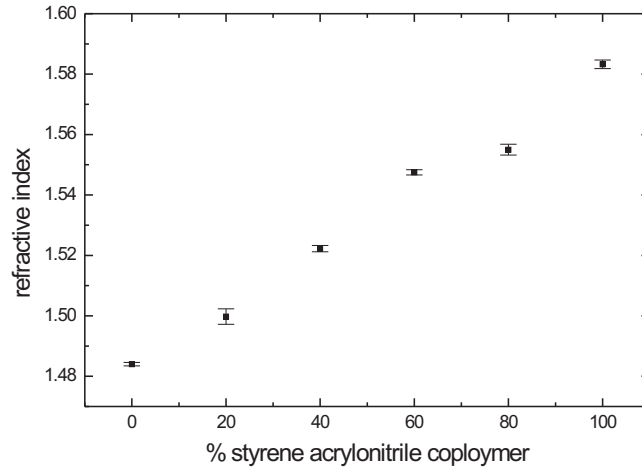
Figure 6.8: Refractive index of PMMA with varying percentage of styrene acrylonitrile copolymer (SAN).

cast waveguides can be explained by the different fabrication methods. For the milled waveguides the doped PMMA is spin-coated and then baked until the solvent is evaporated. In contrast to that, for the molded waveguides, we press the PDMS mold into the still liquid doped PMMA and let the solvent evaporate before we remove the mold.

The presence of the residual layer of doped PMMA seems to have the main impact on the increase of propagation loss. The residual layer causes light to get lost towards the bulk of the microsystem. This assumption is corroborated by the fact that structures that were milled into a native PMMA slide also show a poor guidance of light, with propagation losses in the range of $7 - 10\,\mathrm{dB/cm}$.

Another influence on the quality of waveguides is their thickness. After fabrication of the test structure shown in Fig. (6.2), we measured the length and width of the waveguide. These measurements showed that while the length of the waveguides did not change significantly, the waveguide widths were reduced to between 80 and $90\,\mu\mathrm{m}$. Since the influence of surface roughness increases with decreasing waveguide diameter, this reduction of the width could be one explanation for the larger propagation loss [61]. Additionally, non-uniformity generated by unevenly applied pressure can also play a great role in influencing the quality of the waveguides. Clearly, optimizing the casting process is therefore a primary goal for the future.

Comparing our results with the propagation loss of SU-8 [80], which is often used as waveguide material, shows the advantage of using PMMA. In Fig. (6.9) the propagation losses for doped PMMA and SU-8 waveguides are
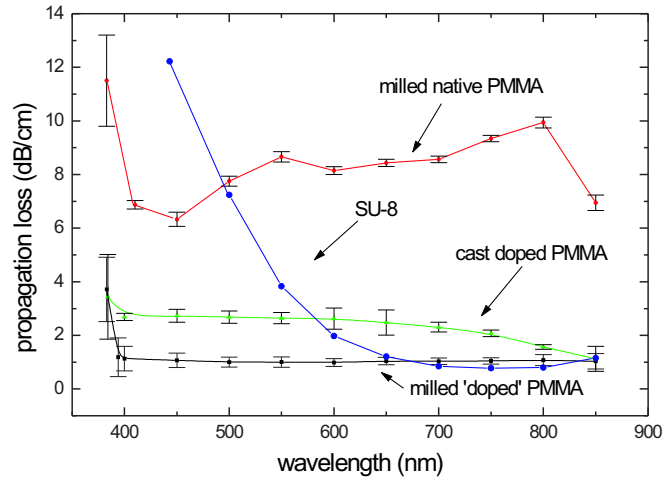
Figure 6.9: Propagation losses of optical waveguides that were milled or cast into doped PMMA. Additionally, the losses of waveguides that were milled into a native PMMA substrate are presented as well. The comparison of PMMA and SU-8 waveguides shows a rapid increase in propagation loss for SU-8 waveguides at wavelengths below 650 nm (original dataset for SU-8 taken from Mogensen *et al.* [80]).

represented in the same graph for comparison. While the losses for SU-8 waveguides increase rapidly at wavelengths below 650 nm the propagation loss for the milled PMMA waveguides remains at around 1 dB/cm down to 400 nm.

Besides effects from scattering, propagation loss is mainly caused by absorption in the waveguide material. Not unlike Joule heating in electrical circuits, guided light can therefore generate heat, which will increase the temperature of the waveguide. If the optical power or absorption is too high, this heat can affect the optical properties or even destroy the waveguide. Increasing the optical power to compensate for the high propagation loss of SU-8 at low wavelengths is therefore not an option.

Generally, the propagation losses of the milled as well as the cast waveguides could be decreased by adding a further process step. Heating the structures up to a temperature close to their glass transition temperatures could minimize the surface roughness. A comparable effect could be achieved by shortly exposing the structure to an organic solvent.

In this work, we used micromilling to prepare the master. To be able to compare the results with the directly milled waveguides, the above men-
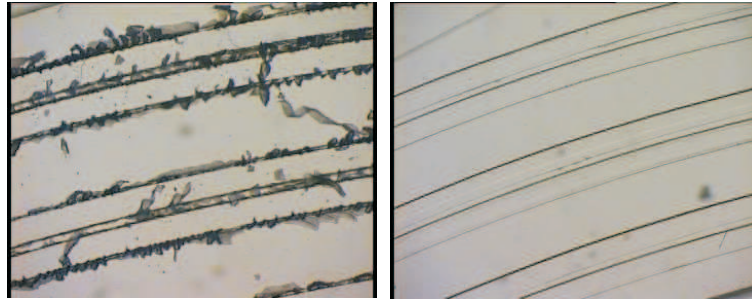
Figure 6.10: 100 μm wide waveguides machined with a high feed rate (40 mm/min) and no cooling (left panel), as supposed to using a lower feed rate (15 mm/min) and cooling (right panel)

tioned test-structures were used as masters for the casting process. However, other fabrication techniques to produce a master structure, like conventional cleanroom processes, are also applicable and would potentially lead to higher quality copies.

6.5   Conclusion

In this study, we have presented two methods of fabricating microsystems with integrated waveguides: one method for flexible and direct fabrication and one method for high number production. The direct fabrication method circumvents the use of photoresists to produce waveguides with high transparency and will therefore be useful in a laboratory environment, while the high number production method could be a valuable tool for mass production of single-use bio/chemical microsystems. Both processes ensure the waveguiding properties using a spin-coated layer of 'doped' dissolved PMMA with increased refractive index onto the native PMMA substrate.

The experiments performed have shown robustness of the design approach and the technology. Low propagation losses were measured ($<$ 1 dB/cm for the milled waveguides and between 1 dB/cm and 3 dB/cm for the cast waveguides) for the entire visual range.

The work developed is based on inexpensive technologies in terms of materials and facilities used and can be applied to a wide choice of thermoplastic polymers.

An application that used the presented approach was fabricated in collaboration with an exchange student from Warsaw Technical University, Dorota Stadnik. Here, two curved parallel waveguides were employed to determine the refractive index of a liquid that was injected into a fluidic channel between the waveguides, as depicted in Fig. (6.11). This application actually uses the roughness of the side walls to allow light to propagate laterally between the waveguides. The approach was used to successfully
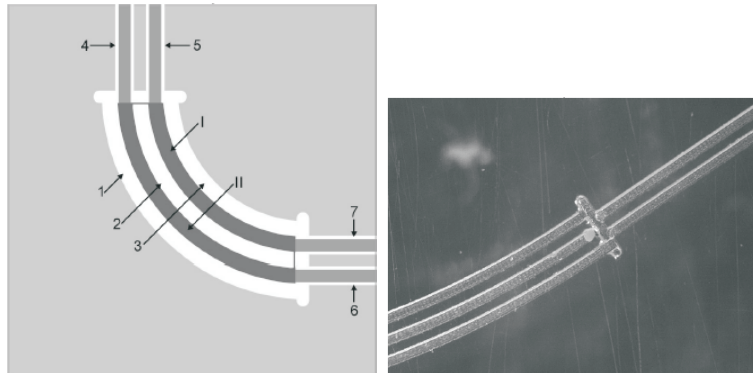
Figure 6.11: Left: Sketch of the coupler: (1,3) micromilled grooves to achieve waveguides, (2) groove as fluidic channel, (4-7) grooves for inserting optical fibers, (I and II) waveguides. Right: Optical photo of the micromilled structure.

determine the concentration of glucose [92] and demonstrates a simple and effective method using integrated optical waveguides.

6.6 Outlook

Although, as demonstrated, rough side walls of waveguides can be advantageous for certain applications, the main focus in the future will be put on reducing this roughness and increase the transmission. However, it is obvious that direct micromilling of optical waveguides is reserved to the research field. For mass production, the presented casting or, furthermore, embossing techniques should be used. While the functional principle was proven during this work, optimization of the procedure will be performed to allow more economical fabrication.

Chapter 7

Bonding

7.1 Introduction

Microsystems possess several advantages as far as chemical analysis is concerned. They allow faster throughput, much reduced sample size and lower cost. It is, however, important that the produced microfluidic systems have a proper sealing to allow a high enough liquid pressure in the system and minimize contamination. Various approaches have been developed to seal microfluidic devices. While bonding methods for conventionally fabricated microsystems have been described a lot [93–95], bonding of polymer microdevices still is a challenge and requires further investigations. There have been a number of reports on different approaches as they have been used for applications, but research on the bonding itself has hardly been conducted. Focusing on polymers, various possibilities to bond two substrates are available, which all show advantages and disadvantages.

In this work, several bonding methods have been employed and investigated with the aim to compare and to apply the optimum technique for the individual applications. In a first section, commonly used techniques employing adhesives are compared and their challenges for polymer-based bio chemical microdevices are discussed. Apart from that, an adhesive bonding approach is presented that allows to join a cleanroom-structured SU-8 layer with a PMMA-lid and, thus, to combine MEMS-based fabrication with conventional machining. In another section, direct thermal bonding is characterized and the bonding strengths and the deformation of the substrate are determined for varying parameters. Furthermore, our experience in producing multi-layer structures is formulated and techniques, such as alignment approaches, are discussed. Finally, a corona discharge enhanced method is presented that allows to decrease the bonding temperature and therefore to minimize the risk of deformation during the bonding process.

7.2 Adhesive bonding

For a limited number of applications the use of adhesives to bond two polymer substrates is a possibility. Bonding of different materials, for instance thermoplastic to thermoset polymers, can be realized using adhesives. Also, varying expansion coefficients between the materials can be compensated to a certain extent, which, for instance, allows to bond a polymer to a glass substrate. The risk of clogging channels or contamination of the systems, however, is high, and therefore the main effort in the field, that describes the use of adhesives, focuses on how the glue is applied to the substrates. Spinning [96, 97], spraying, transfer from a barrel or stamp [98], or some more unique methods have been reported [32].

On the other hand, the core idea of biochemical microsystems is to handle, investigate or treat chemical or biological samples. The concern that one of the constituents of the adhesive could affect the reaction or contaminate the chip always stays in mind. Sealing a channel with an intermediate adhesive layer between lid and substrate covers the entire surface has the consequence that the sample or reagent is in direct contact with the adhesive. Hence, it has to be ensured that the glue is inert and does not dissolve or that its ingredients do not affect the sample. One method to minimize the contact area between sample and adhesive are techniques that apply the adhesive locally [98].

Also, from the constructive point of view, the choice of the proper type of glue is of major importance. The solvent of solvent-based adhesives can affect the substrate material and thereby destroy the device. Thus, the compatibility of the glue and the substrate has to be considered.

Sealing of devices featuring integrated optics requires yet different properties of the glue. To ensure, for example, total internal reflection of integrated waveguides, a lower refractive index of the glue compared to the substrate material is necessary (see Chapter 6). Since the refractive index usually is not listed in the datasheets of commercial adhesives, it is difficult to estimate the applicability of the individual glue.

The use of single or double-sided tape is a good solution for rapid prototyping and quick solutions in the research field [99]. While clogging can chiefly be avoided using this method, contamination, on the other hand, might still be an issue. Although tape is frequently used to seal prototypes, it was not further investigated in this work.

Similarly to the use of tape, lamination is a fast method for prototyping [100]. Here, a foil coated with adhesive is brought into contact with the substrate. Heat is applied while foil and substrate are pressed together, which activates the adhesive and seals the structure. The risk of clogging is also present using this approach. No further investigations on this method were made in this work.

Most thermoplastic polymers can be dissolved by organic solvents. Since

it is a common workshop practice to use solvents, e.g. acetone, to bond, for instance, PMMA together, the use of solvent assisted bonding has also been applied to polymer microdevices. One major disadvantage is the difficulty to apply the solvent without distortion of the structured surface. Some efforts have been made to circumvent these problems [101, 102]. However, because of the manifold problems due to the presence of the solvent, this approach was not pursued in this work.

In the following section, a low-temperature bonding method is described that used contact glue to easily seal cleanroom fabricated devices with a plastic lid. The refractive index of the glue was determined to allow sealing of microoptical devices.

7.2.1 Fabrication and Experiments

Contact glue was diluted with toluene (20 ml glue with 40 ml toluene) and spun onto a PMMA substrate at 4000 rpm, which resulted in an adhesive layer thickness of $\approx 10\,\mu$m. The solvent evaporated immediately after the coating process and gave a sticky surface. The PMMA was then pressed onto the structured substrate (in our case a SU-8 layer containing waveguides) with the coated surface, clamped together and put into a convection oven for 1 hour at 60°C (see Fig. (7.1)a and b).

The described procedure gave a high adhesion and a hermetically sealed structure. No clogging of channels could be observed. The refractive index was determined to be $\approx$1.48 using a prism coupler, which ensured the waveguiding properties of the integrated optical SU-8 waveguides (n=1.59).

It could be observed that after a few days some bonded devices showed partial delamination of the SU-8 layer from the silicon wafer (probably due to failure of the SU-8 processing). To take advantage of this effect the delamination was supported by placing the structure in a low concentrated sodium hydroxide solution over night at ambient temperature. Subsequently, the SU-8 structure could be released without destruction and bonded to a second PMMA lid with adhesive coating (Fig. (7.1)c and d), thus yielding a fully transparent device.

7.2.2 Results and Discussion

This example of using adhesives for permanent sealing utilizes the strong bonding between the materials. Polymer lids that contain standard threads for interconnection can be produced using economic mass fabrication methods and can be directly attached to the microdevice. Further, apart from only sealing of microfluidic systems, functional elements that have been conventionally machined can be combined with the precision of cleanroom structured devices. This combination of economic production and precise fabrication opens new room for various applications.

a)	SU-8 is spun onto an oxidized silicon wafer and subsequently structured with photolithography. Additionally, a thin adhesive layer is spun onto a PMMA substrate.
b)	The PMMA lid is pressed onto the SU-8 layer.
c)	The adhesion between the adhesive layer and the SU-8 is strong enough to release the SU-8 from the silicon wafer.
d)	A second PMMA substrate is pressed onto the other SU-8 side to seal the structure.

Figure 7.1: Flow chart of the adhesive bonding procedure. For simple sealing of an SU-8-silicon structure only steps a) and b) are necessary. To embed SU-8 between two polymer substrates steps c) and d) have to be conducted additionally.

Successful sealing of microstructures could be shown using this approach, as depicted in Fig. (7.2) and Fig. (7.3). The former shows an ammonium detection chip with integrated optical waveguides based on SU-8 fabrication as described in Ch. (5). The device was sealed with a 1.5 mm PMMA lid that contained fluidic interconnections. Fig. (7.3) shows a similar chip type with the SU-8 layer bonded between two PMMA layers. The latter version was interconnected using a side connector as described in Ch. (8).

7.3 Thermal bonding

Bonding itself is a physico-chemical process where polymer chains of two surfaces interact with each other. Thermal bonding offers the possibility of bonding two polymer substrates without using adhesives. To seal a device using thermal bonding, the substrates are pressed together and heated up using a furnace or a heatable press. The high temperature, usually in the range of the glass transition temperature of the polymer, increases the risk of deformation of the substrates. In general, higher temperatures increase the
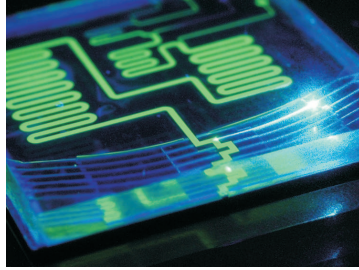
Figure 7.2: PMMA lid bonded to SU-8 layer that was previously spun onto a silicon wafer and structures by photolithography.
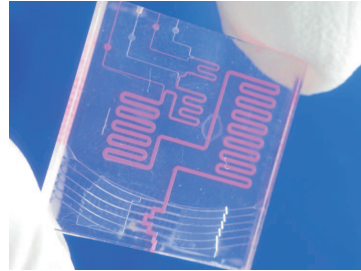
Figure 7.3: The adhesive bonding strength was strong enough to lift-off the SU-8 layer from the silicon (compare to Fig. 7.2)and attach it to a second PMMA substrate.

bonding strength, which is, on the other hand, accompanied by a larger risk deformation. Both, decreasing the bonding temperature or the necessary applied bonding stress can help to minimize the deformation. However, since it is more convenient to determine and control temperature compared to force, the main effort should be put on the reduction of the bonding temperature.

One method that allows to avoid heating the entire device during the bonding process is laser bonding [103]. The beam of an infrared laser is focused on the contact plane of two substrates and scans selectively the areas that should be bonded. Since the light has to permeate through the substrate to selectively heat up the contact area, the absorbance of the light in the contact area has to be several magnitudes larger than in the rest of the material. This is achieved by spinning a thin layer of high absorptive polymer onto the substrate surface prior to structuring. The spun substance can for instance be dissolved substrate material, with small amounts of carbon black added to increase the absorptivity. The advantage of laser bonding is the selective and local heating of the substrates, which allows special applications. Laser bonding is a good alternative to adhesive bonding. It requires, however, dedicated equipment and extra process steps.

Microwave bonding of polymer-based substrates uses the absorbance in a thin metal film. The metal is deposited onto the polymer surface of one substrate before the second substrate is applied. Polymers, such as PMMA, are relatively transparent for microwaves at certain wavelengths, while the metal layer is locally heated when microwave power is absorbed [104]. Depositing the metal layer after structuring the substrate, causes heating of the entire structured surface and can lead to deformation. Furthermore, the surface becomes conductive (e.g. inside the microchannels) and the transparency decreases, which represents a problem for electro osmotic flow and optical detection. Processing the substrate after deposition can cause destruction

of the metal layer and thereby failure of the bonding.

Another possibility that utilizes an intermediate layer is to use substrate material with lower molecular weight [105]. With decreasing molecular weight, the glass transition temperature also decreases and allows to use lower bonding temperatures. While the intermediate layer is heated up to its glass transition temperature this temperature is too low to deform the substrate. To realize the intermediate layer, dissolved polymer is simply spun onto the substrate surface.

7.3.1 Direct Thermal Bonding

Polymer microfluidic systems can be sealed using direct bonding at increased temperatures. The material, heated up to close to its glass transition temperature, becomes soft and the number of free polymer chains at the surface increases. Thermal bonding is therefore preferably used for thermoplastic polymers. Increasing the temperature, on the other hand, increases the risk of deformation during the bonding process, as already mentioned. The deformation can appear as (lid) material that is pressed into a hollow structure (e.g., a channel or cavity) or as straightforward deformation and distortion of the substrate's microstructure.

The most important balancing act for direct bonding is to yield a well bonded seal on top of the produced PMMA system, while, on the other hand, to avoid clogged microchannels within the system. There have been some publication about direct bonding [106–109]. However, these publications did not discuss the sealing of microsystem. Articles about bonding of relatively sensitive microfluidic systems are rarer [110]. This work takes what is known about direct bonding into account and additionally reports on the practical experiences we had with the bonding of PMMA microfluidic systems.

Direct Bonding Technique

Direct bonding or glueless bonding is a technique to put a lid onto a structured microsystem. The two halves are first cleaned to a certain degree and then put on top of each other in a hand-held vice grip, as depicted in Fig. (7.4). The clamped halves are then set into an oven and heated almost to the glass temperature of the used polymer, in this case PMMA. They remain at the temperature for 2 h and are afterwards taken out of the oven and cooled down to room temperature again. After that, they are in principle ready to be used. However, an improved way of directly bonding is to first anneal the bonded microsystem over night as described below.

Annealing

Polymer microdevices can be structured in many ways, for instance by laser ablation, micromilling or embossing. Temperature gradients appearing dur-
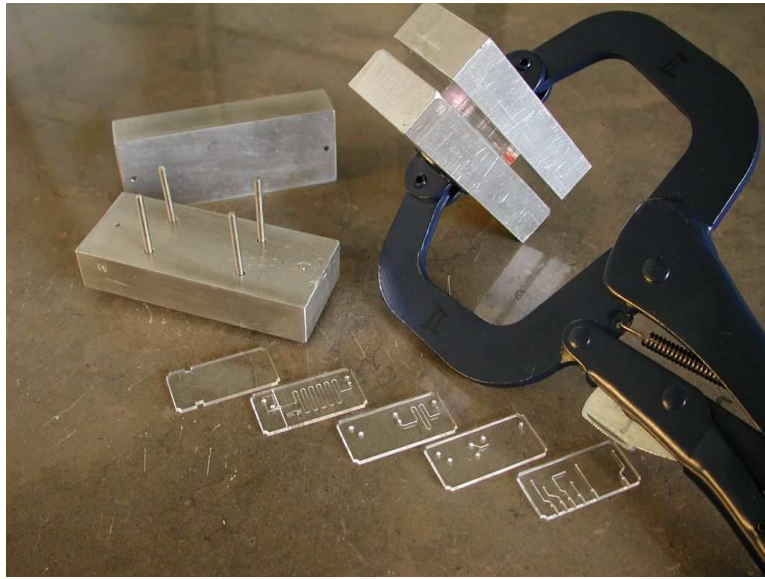
Figure 7.4: The photo displays our direct bonding equipment. In the foreground there are five different PMMA plates that need to be bonded together. To the left side of the photo, a bonding frame can be seen. The five plates are set into the center area between the four pins and held by the pins. In the corners of each plate, a small rounding has been cut to allow the pins to hold the plates. With the lid on top of the pins, the bonding frame is held in place by a vice grip (No.7, Scangrip), shown to the right of the photo. The vice grip had a reproducible setting force, so that always the same force could be used to clamp the PMMA pieces.
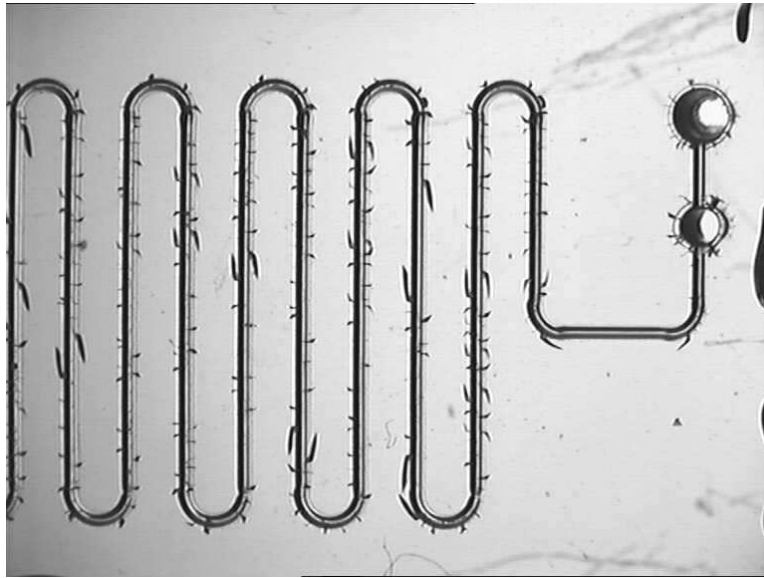
Figure 7.5: The photo shows a microchannel within a PMMA sys-
tem. The microchannel is surrounded by many small cracks that
most often are perpendicular to the channel. These cracks were
produced by not annealing the microsystem and afterwards clean-
ing the system with ethanol. The evaporation of the ethanol caused
the microsystem to contract too suddenly and led to cracks due to
the tensions in the system. Annealing would have balanced these
tensions.

ing these processes cause thermal stress. To produce a durable and insensi-
tive bonding, a machined microsystem should be annealed prior to bonding.
Annealing means, that the two PMMA halves, after structuring, are laid into
an oven overnight at elevated temperatures (but below the glass tempera-
tures) at, for instance, $80\,°C$ and then slowly allowed to cool down cooled
down following a temperature program. In the course of the night, the poly-
mer microsystem's polymer chains slowly relax into states with less tension.

After the chains have relaxed, the bonded microsystem is less sensitive
to other influences, for example less sensitive to being wiped with ethanol
to clean its surafce as shown in Fig. (7.5). Other advantages lie in the
possibility to process the microsystem after bonding, for instance, to drill
additional holes into the system. Every usage of the system will be more
robust after the system has been annealed. An examples in the literature is
the article from Yang *et al.* [111].

The ethanol used in Fig. (7.5) had the purpose to clean the surface from
condensed PMMA, as it appears during laser ablation [86], and to soak the
intermediate surface layer, since PMMA can be dissolved in organic solvents,
such as ethanol, and, more aggressively, in acetone. We found, however, that
no extra soaking and softening with the help of ethanol was necessary, since

the PMMA could also be thermally bonded without ethanol. Thereafter, we only used a low concentrated soap water solution to clean the microsystems.

Distortion-free Polymer Surfaces

Visual inspection is a typical means of observing failure in microfluidic systems. Furthermore, optical detection through transparent lids is a common practice using microsystems in chemistry and biology. Especially in the latter approach, it is vital to have a distortion-free view. Direct contact of the polymer substrates to rough surfaces, such as the metal frame, during bonding should thus be avoided to eliminate embossing of the frame pattern into the polymer. Here, glass as an intermediate layer between substrate and frame can provide assistance.

Force Distribution

When pressing a microsystem together with a bonding frame and a vice grip, as shown in Fig. (7.4), it can be problematic if the exerted forces are not equally distributed on the microsystem halves. In this case, two sheets of a rubber-like material can be of help. The rubber slides, for instance silicone rubber, will distribute the exerted force well due to their elasticity.

A more equal force distribution can be achieved using a dedicated heatable press. However, we chose vice grips to apply the stress to be able to fabricate many devices in parallel. Heating up the entire bonding setup further ensures an equal temperature distribution in contrast to locally heated plates of a press.

Experiments and Results

Prior to discussing the influence of certain parameters on the bonding quality the terminology should be clarified. *Bonding stress* is the mechanical stress applied to the substrates by pressing them together during the *bonding process* (unit: N/mm^2). *Bond or bonding strength* (both used equivalently) is the maximum force a bond of a certain area can withstand before yielding (unit: MPa). As the result of a force being applied to a bonded area bonding strain can be observed.

To examine the quality of the bonding, we built an experimental set-up, where several bonding parameters, such as temperature T and bonding stress p could be changed. The basic materials for the set-up were two PMMA halves, one PMMA slide with a hole of 4 mm in the center, and a second circular piece with a diameter of 16.46 mm, as depicted in Fig. (7.6). By bonding the circular piece centered onto the slide over the through hole, the effective bond area is 2 cm^2.
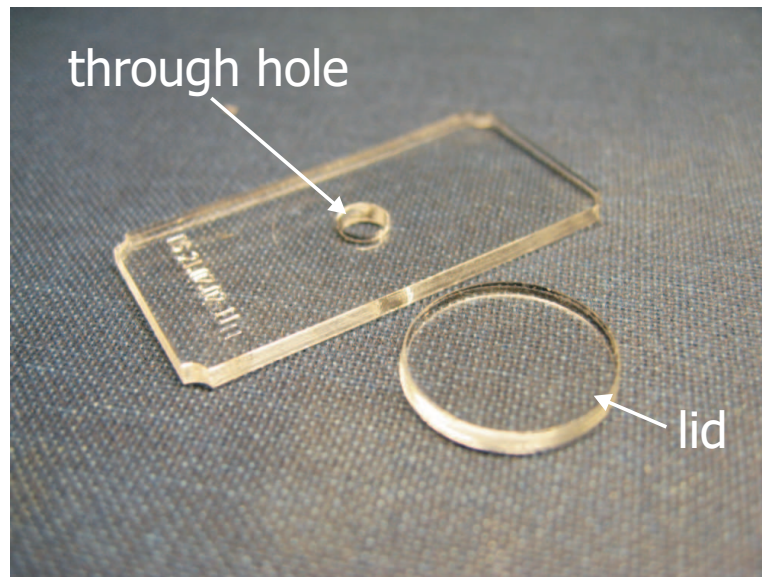
Figure 7.6: The two-part bonding test structure consisted of a 2x4 cm large PMMA slide containing a 4 mm center hole and a circular lid with a $2\,cm^2$ area (ø = 16.46 mm). The thickness of both parts was 1.5 mm

After bonding the two PMMA pieces, the quality of the bond was tested in a bonding frame set-up shown in Fig. (7.7), into which the bonded sample was inserted as drawn in Fig. (7.8)

An attached load cell measured the force that was exerted on a bolt, which pressed on the inside of the sample's circular lid. Using a strain curve, as displayed in Fig. (7.9), the maximum bonding strength was obtained. A force is applied to a small spot, which results in a local deformation. This so called peeling stress is known as unfavorable stress for bondings and is also typical for high pressurized microfluidic channels that are sealed with a lid. In contrast to often used standard pulling tests, our method therefore gives a more realistic estimate of the bonding quality under conditions as encountered in microfluidics systems.

How much the bonding strain of the system changed when varying the bonding stress is shown in Fig. (7.10). The stress of the clamp does not seem to have a great influence on the bonding quality. Rather it seems to be important that there is some kind of clamping action at all, which should be higher than about 0.94 bar.

The change in bonding temperature was tested in another experiment. When the temperature rises between 100 and 120 °C, the bonding strength increases from 5 to $15\,N/mm^2$, as displayed in Fig. (7.11). However, just below 100 °C the quality of the bonding strength dropped from 5 to almost $0\,N/mm^2$. This means that the bonding temperature has a very strong

Figure 7.7: The photo shows our bonding force set-up clamped into a vice. The clamped part held the microsystem being tested, while the cylindrical part next to it on the right could be could be screwed into the holder. To the utmost right was a load cell (ELA-B1E-500N, Entran, Ludwigshafen, Germany), that exerted a certain force on the test system. It was possible to record the forces on-line as shown in Fig. (7.9). The technical drawing in Fig. (7.8) explains the details of this photo.
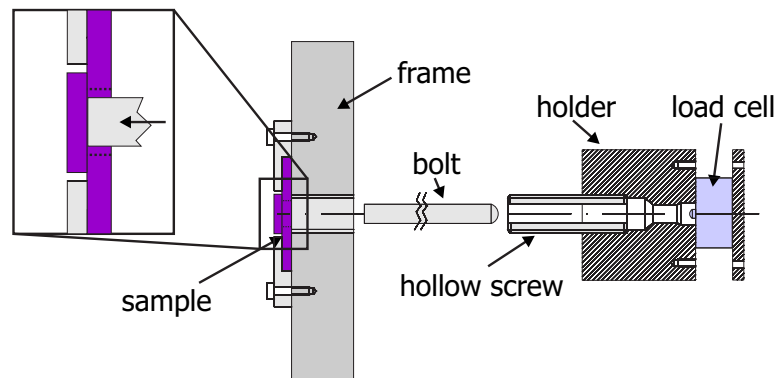
Figure 7.8: The technical drawing shows the details of Fig. (7.7) and depicts the bonding force set-up as a cross-sectional view. The very left shows a test sample inserted into a frame. To the right, a load cell mounted inside a holder with an attached hollow screw is shown. Screwing the entire holder with the screw into the sample frame moves the bolt towards the sample, pressing itself onto the load cell. Further screwing applies a stress through the hole to the sample's lid, as can be seen in the inset. This stress can be determined with the load cell.
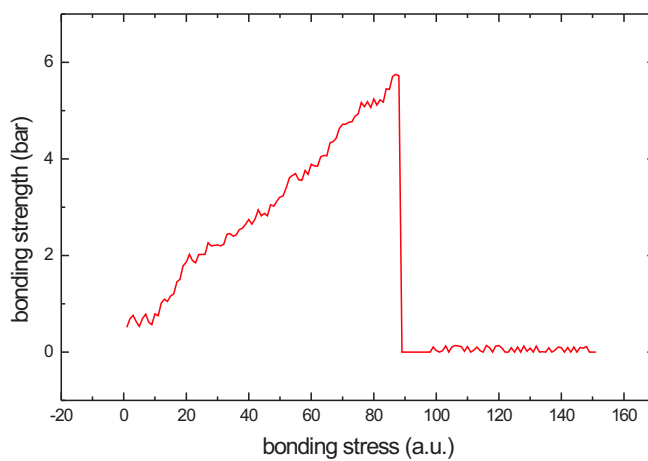
Figure 7.9: This graph shows a typical strain curve recorded by the load cell of Fig. (7.7) and Fig. (7.8). The strain itself is not important to determine the bond strength. In fact, it is the stress, at which the maximum strain is recorded that equals the bonding strength. The graph shows a typical rising load until the circular lid suddenly fell off and the load dropped down to a certain small noise level. The stress scale is arbitrary since the direct output of the load cell is shown, which is a voltage.
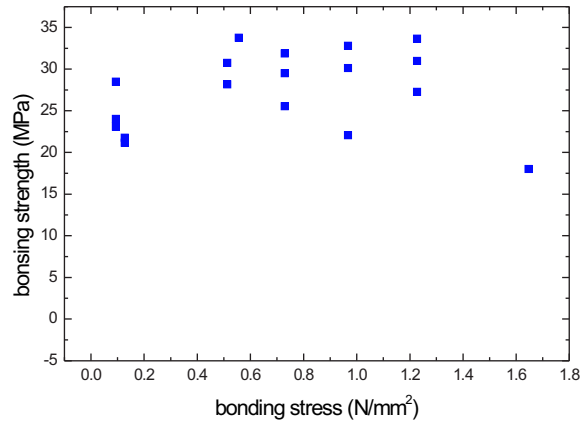
Figure 7.10: The quality of the PMMA bond is shown on the y-axis as the bonding strain, while the x-axis shows the change of the exerted stress during bonding on the circular lid. The temperature was kept constant at $T = 110\,°\mathrm{C}$. Beside s certain variation, all data over $0.4\,\mathrm{N/mm^2}$ show an almost constant bonding quality of about $30\,\mathrm{MPa}$ with some added noise.
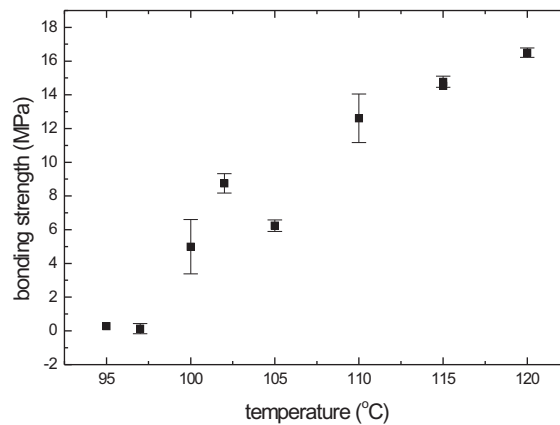
Figure 7.11: The graph shows an increasing bonding strength at elevated temperatures. The stress was kept constant at $0.94\,\mathrm{bar}$. The glass temperature of PMMA is about $105\,°\mathrm{C}$ and lies in the center of the temperature variation. At smaller temperatures, the bonding strain is equal to zero and rising relatively fast at just below $100\,°\mathrm{C}$. To achieve a bond, a certain minimum temperature is required. On the other hand, at elevated temperatures, the bond strength seems to reach a maximum level.
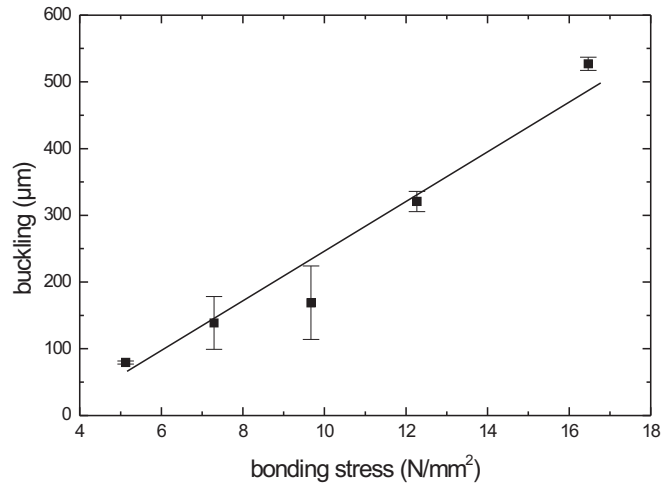
Figure 7.12: The buckling graph makes a statement of how deep the circular lid was extending into the circular hole beneath it at its deepest point. A single microsystem was produced and the bonding stress for the system was measured. The popped off lid of the system was then cut through and it was measured how deep the lid buckled in the hole. For these measurements, we used a microscope with a built-in eyepiece graticule.

influence on the bonding of the two PMMA parts and that the temperature should be just below the glass temperature of the polymer.

Judging from Fig. (7.10) and Fig. (7.11) we conclude that bonding stress is necessary, but the amount of stress is not as important. The stress should not be too high to avoid deforming of the microchannels in the system. At the same time, the bonding temperature is relatively important and should be kept at temperatures just below the glass temperature to keep the form of the microchannels, but also to provide a good bonding. A result that shows how deep the PMMA lid buckled into the opening beneath it is shown in Fig. (7.12). Within the examined region, the buckling into the microchannel is almost linear with the bonding stress. The higher the bonding stress, the deeper the PMMA plate buckled into the central opening. When a polymer sheet buckles into a hole or microchannel, it will eventually clog the underlying space. However, from Fig. (7.10) we remember that the strength was almost independent of the stress. Thus, it would be a good choice to use as little stress as possible to bond a microsystem.

The risk of clogging can further be influenced by the geometry of the structure. Interestingly, when the cavity below the PMMA is open at the sides of the system, then the polymer sheet does not buckle as much into the

system. An explanation of this phenomena can be found in the air inside the closed cavity: during heating the air expands and diffuses into the gap between the, at this point, yet unbonded lid and substrate. After bonding, the device is cooled down and the expanded air is trapped in the gap (can sometimes be seen as small air bubbles). Inside the cavity an underpressure is generated which might deform the still soft polymer. This means that, if possible, the microchannels should have an opening, such as a connector, to the sides to allow possible over- or underpressures to be equalized.

Fig. (7.12) and Fig. (7.10) can be taken together to find a good bonding stress value. From Fig. (7.10) we saw that the bonding stress did not have a great influence on the bonding strain. However, Fig. (7.12) showed that the PMMA lid buckled into the underlying cavity and reduced its volume more and more. From these graphs we conclude that bonding stress values up to 8 bar are good values for the PMMA that we used.

Materials

Although the experimental data were acquired using PMMA samples, thermal bonding was also tested with other polymers. Adjusting the bonding temperature to the particular glass temperature of the individual materials, good bonding qualities could be achieved.

It is, however, relevant to note, that parameters showing good bonding results for a number of experiments are not unalterably valid for the entire polymer type. In fact, it could be observed, that the bonding behavior varied in a wide range for different batches of the same material. Production modifications at the manufacturer side can cause manifold changes of the material's properties and are well known in research. Thus, the present results have rather to be seen as a guidance than a determination of universal values.

Another observed problem were non-sticking coatings deposited onto the polymer surfaces. The purpose of this coatings is to relieve the removal of the protective foils polymer plates are usually provided with. It is obvious that these coatings are not conducive to the bonding process. As a remedy, grinding the surfaces can remove the coating but influences the transparency and is by itself a time consuming procedure. Chemical treatment can cause equal problems as described above. Thorough wiping with a soap water drenched lint-free tissue prior to structuring gave acceptable results in this work. A more sophisticated method is the use of plasma to enhance the bonding, as described further below.

Alignment

In contrast to sealing single substrates, bonding of more than one layer requires precise alignment of the individual structures during the bonding
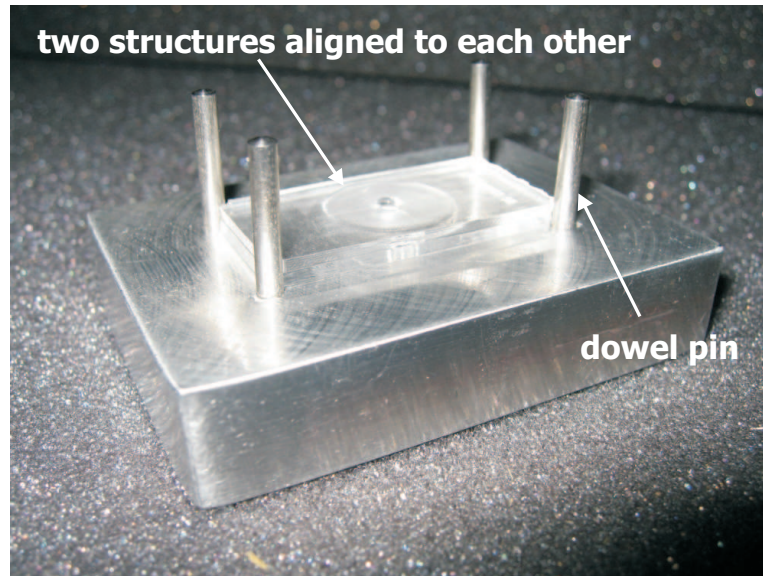
Figure 7.13: Bonding frame with fixed alignment pins. During heating, the polymer expands more than the metal which can lead to buckling of the microstructure.

process. Dowel pins offer a simple way to establish the alignment of the layers with respect to the bonding frame and to themselves, as Fig. (7.13) shows. However, a tight fit during the entire bonding procedure can lead to problems. The bonding frame is usually machined from metal, e.g. aluminium, while the layers consist of polymer. Heating up the setup leads to differential expansion of the materials due to their individual thermal expansion coefficients (aluminium: $23 \cdot 10^{-6} \text{K}^{-1}$, PMMA: $85 \cdot 10^{-6} \text{K}^{-1}$, glass: $4 \dots 8 \cdot 10^{-6} \text{K}^{-1}$). The larger expansion of the polymer results in mechanical stress, deformation and, consequently, in failure of the bonding. This can be avoided by removing the alignment pins after the layers have been fixed in position by the applied external pressure, which requires, however, a more sophisticated bonding frame. The use of dowel pins whose lengths do not exceed the structure's thickness, and thus are not in contact with the frame, is another possibility to prevent problems due to different expansions, as depicted in Fig. (7.14).

7.3.2 Plasma Enhanced Thermal Bonding

As a conclusion from the previous section, the bonding temperature has a major impact on the resulting bonding strength. A temperature close to the glass temperature ensures a high bonding strength but, on the other hand, increases the risk for deformation. It is, however, necessary to apply a certain stress to join the substrates. Consequently, optimizing the bonding
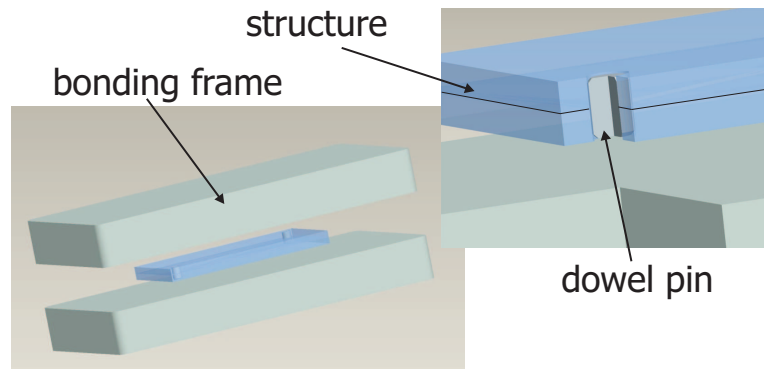
Figure 7.14: Short dowel pins are not in contact with the metal and thus prevent any restriction of the microstructure's expansion.

parameters can be a time consuming process that has to be repeated for each individual material combination. Hence, activating the material's surface to reduce the necessary bonding temperature can help to reduce the number of critical parameters and to simplify the bonding procedure.

In the field of microfluidics, the process of surface activation for bonding purposes is mainly known from silicone (PDMS) devices. Here, the surface is oxidized using, for instance, strong acids [112] or plasma [104, 113–116]. The plasma can be generated using a designated plasma asher [113, 114], a microwave oven [104, 115] or a tesla coil [116]. In this work, the latter approach is investigated since it represents an economic alternative to expensive equipment and can easily be applied in a conventional laboratory. Safety rules, however, have to be considered.

bonding must be simple, just use an oven, clamp it, stress does not matter and temp can be adjusted easily in comparison to force

Activating the substrate surface by oxidation can be a further method to decrease the bonding temperature. A well know example in the field of microfluidic devices is the oxidation of PDMS surfaces to directly bond two substrates. The oxidation is mainly done with oxygen plasmas but acids also can be used.

In this work we are investigating the impact of plasma on the bonding temperature of various polymers using thermal bonding. The plasma is thereby generated by sparks

Setup and Experiments

After proper cleaning of the test structures, the samples were applied to the plasma generated by corona discharge. To create the corona discharge, a chopper circuit in combination with an ignition coil a generated a high voltage of $\approx$60.000 V. The voltage was applied between two electrodes that were fixed inside an insulated chamber, as shown in Fig. (7.15). The chamber
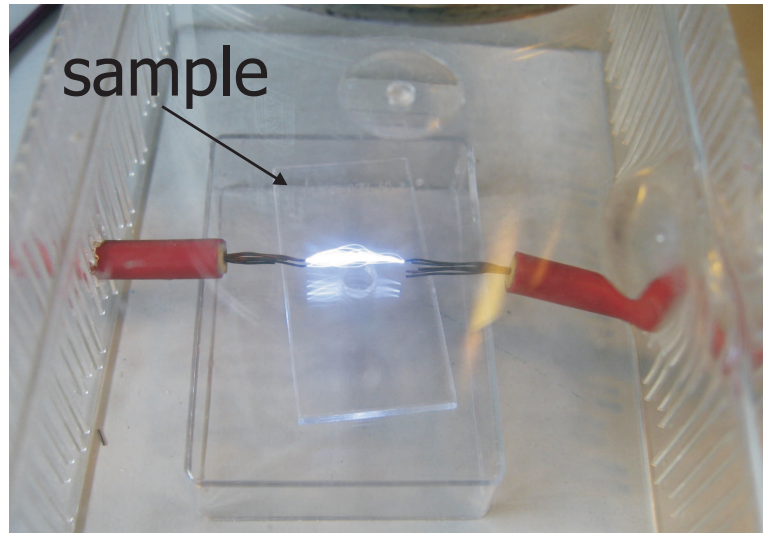
Figure 7.15: Two fixed electrodes inside an insulated chamber provided a corona discharge above the surface of a test structure. The sample was placed onto a small plastic box to lift it up close to the sparks. Moving the chamber with the electrodes allowed to apply the discharge cloud to the sample's entire surface area.

with the electrodes could be moved, which allowed to apply the discharge cloud to the entire surface area of the sample for approximately 10 s. A distance of 5 mm between sparks and substrate surface was observed to be sufficient small for treatment and large enough to avoid thermal impact.

To determine the impact a plasma has on the bonding strength, the setups described in Sec. (7.3.1) were used.

Results and Discussion

The plasma treatment of the sample surface allowed to decrease the bonding temperature from just below the glass transition temperature of approximately 110 °C down to 85 °C achieving equal bonding strengths to those obtained with direct bonding at higher temperatures, as shown in Fig. (7.16) and Fig. (7.11). Since deformation of the polymers at these temperatures is negligible, the applied bonding stress is not longer a critical factor. In fact, a comparably large bonding stress can be used to ensure proper bonding without increasing the risk of deformation. Moreover, the low bonding temperature itself further decreases the risk of deformation and internal stress due to the lower thermal expansion of the polymer.
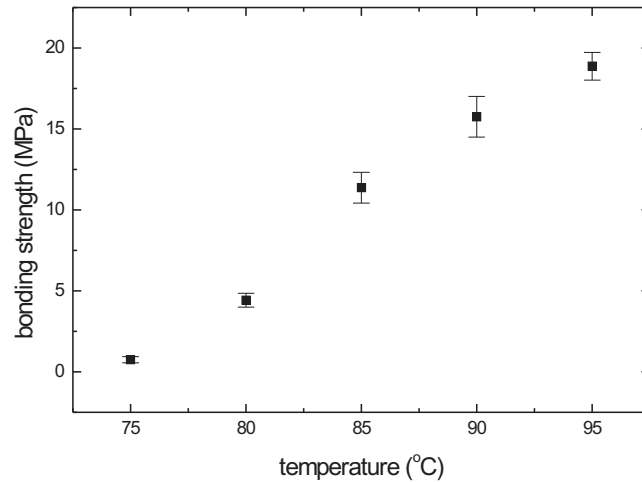
Figure 7.16: Plasma treatment prior to thermal bonding allows a decrease of the bonding temperature by 20 °C achieving bonding strengths in the same range of the strength obtained with direct bonding at higher temperatures (compare to Fig. (7.11)).

7.4 Conclusion

In this chapter we discussed the possibilities to seal polymer-based microfluidic systems. An adhesive bonding method was presented that allows bonding at ambient temperature. Furthermore, this method enables to combine cleanroom fabricated devices with conventionally machined polymer substrates, which ensures economical production.

Direct thermal bonding was investigated and the bonding strengths depending on bonding temperature and bonding stress were obtained using a custom made setup. Additionally, the deformation with respect of these parameters was determined. As a conclusion it can be drawn that with increasing temperature and stress the bonding strength, but, on the other hand, also the risk of deformation increases. At constant temperature, however, an increase of bonding stress does not lead to an improve of bonding strength, but, on the other hand, a certain temperature is required to achieve a bond at all.

To minimize the risk of deformation, a corona discharge treatment of the substrate surface prior to bonding was examined. Using this approach, the required minimum temperature could be reduced by approximately 20 °C obtaining equal strengths as if using the former method at elevated temperatures.

7.5   Outlook

Since more and more microsystems are fabricated in polymers, the investigations that were performed using PMMA will be extended to other plastics.

As shown, the bonding strength depends on various parameters. One goal is to establish a bonding technique that is insensitive to small changes in these parameters, namely bonding stress and bonding temperature. In a first step, this was achieved by the use of a plasma. Subsequently, it is necessary to describe the procedure of the plasma enhanced bonding method more in detail allowing to introduce a recipe that can be reproducibly applied by users.

To approve the use of adhesive bonding methods for lab-on-a-chip devices, a systematic investigation of the impact adhesives have on chemical and biological samples has to be conducted. This will allow to apply specific adhesives resulting in easy sealing of devices without concerns about contamination by the bonding process.

Chapter 8

Fluidic Interconnections

8.1 Introduction

Interfacing microdevices to the macro world is still a challenge. In the case of Lab-on-a-Chip devices, the microsystems may contain electrical, mechanical or fluidic components, for instance. In comparison to electrical contacts, fluidic connections are more problematic. Requirements such as low dead volumes, operation over a wide pressure range, or chemical resistivity are hard to align with an inexpensive and simple design.

Although the main focus in the field of microfluidic devices is on the devices and their various functionalities, a number of solutions for microfluidic interfacing have been developed. An overview of the different approaches has recently been published by Fredrickson and Fan [117].

In general, fluidic interconnections can be divided into permanent and non-permanent connections. In the former approach, adhesives are mainly used to bond thin tubes onto or into holes that have been fabricated into a substrate and are connected to the internal fluidic network. Often, the cross-sectional shape of the channels does not fit or correspond to the shape of the tube, depending on the method that was used to fabricate the channel. This mismatch typically results in a gap. Gluing a tube into place bears the risk of clogging a connection due to glue that is drawn into the gap by capillary forces. Depending on the design, the glue forms cones around the connection tube, and the spatial extent of this glue cone limits the minimum distance between adjacent connections (see Fig. 8.1). As a remedy for the clogging problem, highly viscous glue could be used, but the complexity of the gluing process makes it uneconomical if many connections have to be made. On the other hand, a lot of effort has been put into modifying the shape of the interconnection to allow a better fit and thereby reduce the risk of clogging by adhesives. Gray *et al.* [118] reported on a deep reactive ion etched (DRIE) coupling structure to bond standard capillaries directly to a silicon substrate using adhesives. The The MEMS fabricated fitting structure
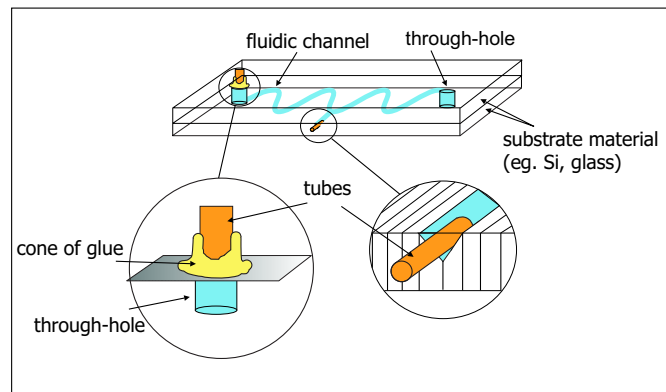
Figure 8.1: Gluing is a commonly used method for fluidic inter-
connection of microstructures. Tubes are glued onto or directly
into through-holes or channels. Using this method involves a high
risk of clogging by glue that is drawn into the channel by capillary
forces.

allowed a direct attachment of capillaries, which were then fixed with ad-
hesives. Further, they combined DRIE and injection molding to fabricate a
press-fit silicon/plastic coupler. In 2001, Meng *et al.* [119] attached capillar-
ies to cleanroom processed coupling structures and bonded these structures
to a substrate using a thermoplastic spray-coating technique. Both groups
used advanced fabrication technologies in combination with glue to achieve
a matching fit to the substrate and cement the interconnection. However,
the risk of clogging prevails. Bings *et al.* [120] directly drilled bottom-flat
holes into the edge of glass substrates to access the channels and then glued
in silica capillaries using thermoplastic adhesive. This method shows an
easy possibility of a direct side interconnection. Yet, there is a high risk
of delamination of the bonded substrates due to strong shear forces, and
clogging of the channels by debris, both resulting from the drilling process.
Puntambekar [121] reported in 2001 on flanging PEEK^{TM} (polyetherether-
ketone) tubes to produce a permanent connection. This method avoids the
use of adhesives. The interconnection, however, is part of the fabrication
sequence of the microfluidic device, which complicates the process.

Non-permanent connections, on the other hand, use a soft intermedi-
ate element in combination with mechanical stress to ensure a sealed con-
nection. Commonly used elements are, for instance, o-rings or membrane
gaskets. In this method, the microstructure with through-holes is pressed
against a holder, which contains connection holes. Tightness is ensured by
o-rings placed between structure and holder (see Fig. 8.2). To keep the o-
rings aligned, grooves can be fabricated around the connection holes. Due
to limited deformation capabilities of the o-rings, it is mandatory that all
grooves have exactly the same depth. In case of more than one connec-
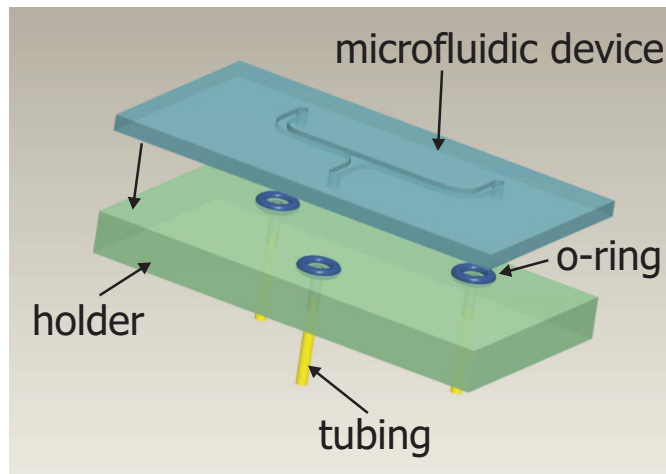
Figure 8.2: O-rings are placed in a concentric groove around the interconnection holes. The microfluidic device is pressed with its through-holes onto the o-rings, which seal the interconnection.

tion this becomes even more important because a varying distance between microstructure and holder would not be compensated for. Further, an asymmetric distribution of o-rings on the holder leads to different pressures applied to the individual o-rings. All these circumstances make the fabrication and operation more difficult.

Nittis *et al.* [122] designed a holder that completely enclosed a fluidic mixing chip and applied a silicone membrane as intermediate sealing element between substrate and standard fittings. However, using a gasket-like sealing over a large area requires a large compression force and therefore a rigid, mechanically stable housing to ensure a tight connection. This, on the other hand, makes it difficult to access the device for optical inspection or detection. The number of applications tolerating this kind of packaging is therefore limited.

Perozziello et al. [123] developed an integrated elastomer connection that allows easy connectivity. Tubes can be plugged directly into the connector and sealing is ensured due to its elastic properties.

Instead of using o-rings or an elastomer membrane, another versatile approach are soft tubes that are pressed against the substrate. Silicone rubber tubes, for instance, are resistant to a broad range of chemicals, to temperatures between -60 and $250\,°C$ and available in various dimensions, with inner diameters smaller than $100\,\mu$m.

The principle of a fluidic side-connector using flexible tubes as sealing elements was patented in 2001 by one of the authors [124]. In 2002, Yang [125] reported on a microfluidic socket prototype for wafer side filling using long silicone tubes that were aligned with a holder.

Since the tube connector was patented in 2001 the field of microfluidics

has undergone a development from purely fundamental research towards more applications, especially in the fields of biology, biomedicine and chemistry. Hence, there is a demand for interconnections to chips in a variety of scientific fields. At the same time, as mentioned above, there are still numerous practical problems with interconnects that probably prevent a faster spreading of the use of microchips in general. We think, therefore, it is very relevant to show an in-depth treatment on the tube connectors, which have been employed in various applications in our lab showing their superior handling capability and performance in everyday use. Furthermore, we examined the tube connector from a theoretical point of view and compared it with other, non-permanent interconnections.

8.2 Design and Fabrication

Since neither gluing nor o-rings are fully satisfactory for rapid and reliable fluidic connections, a different design was examined. The principle is sketched in Fig. 8.3 and uses short pieces of flexible tubing that is available in various dimensions and many different materials. These tube-pieces, which are cut from a long tube, are plugged into a bottom-flat hole. In the center of this hole another hole with a smaller diameter is drilled. This establishes the connection to a standard thread that is cut into the connector from the backside. The length of the tube-piece exceeds the hole's depth so that a small part will protrude out of the hole.

A microsystem with a through-hole that is pressed against the connector will compress the tube about the length of the extension (see Fig. 8.3). Due to its elasticity the tube will seal the connection. In comparison to o-rings the tube is more deformable, which results in a better sealing quality. This also means a better tolerance towards angular misalignment between the microsystem and the holder. In fact, to align device and holder, simple alignment structures (e.g., dowel pins) can be integrated and provide sufficient accuracy.

However, all these principles are applied to devices that are provided with through-holes to allow access to the channel from the top or the bottom of the device. A number of different techniques to prepare these through-holes is used, all with their advantages and disadvantages. Holes in silicon substrates are typically etched, while polymer holes are drilled or laser ablated. Holes in glass substrates are either etched, laser ablated or drilled. Whereas etching produces high quality holes, for a moderate number of holes drilling is a faster process. However, it should be used with care when glass is the substrate to avoid cracking. Laser ablation requires an expensive setup and is not available in every laboratory. Finally, the lid containing through-holes typically needs to be aligned to the structured substrate. Hence, fabrication of through-holes is, dependent on the material, a complicated and time-
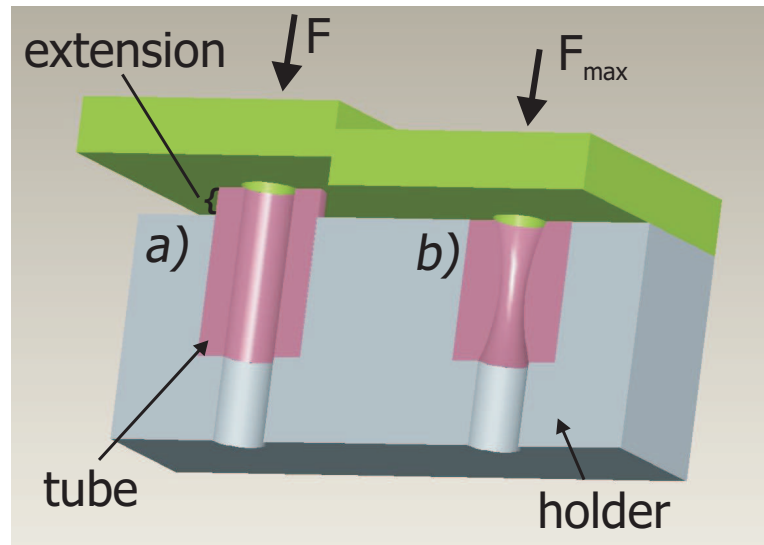
Figure 8.3: Cross-sectional sketch of a simple tube-sealing interconnection: a tube, whose length exceeds the depth of the hole, is inserted into a bottom-flat hole (a). Subsequently, a microfluidic device is pressed onto the tube and establishes a sealed interconnection (b).

consuming process.

One way to avoid through-holes altogether is to make use of the small available sizes and the flexibility of the silicone tubes to directly attach them to the side of a flat microstructure. Channels that are connected to the fluidic network just have to be continued to the edge of the microsystem. After bonding a lid onto the substrate, dicing of the chip will automatically result in side-openings to which the tubes can be connected. Figure 8.4 shows the construction of a side-connector for a flat fluidic microstructure indicating how channel and tube are aligned using the holder. The simple construction of the side connector allows fabrication with conventional mechanical equipment. Furthermore, various standard fittings can be attached by drilling an appropriate thread. For larger number production of the holder, polymer mass production technology, as for instance injection molding, can be applied.

Usage of entire silicone tubes instead of tube pieces, as Yang *et al.* [125] reported, simplifies the fabrication of an holder even more. Cutting of small tube pieces can be avoided and drilling is reduced to simple through-holes containing the tubes. However, fixing the tubes in the holder either leads to a compression of the tubes, or necessitates the use of adhesives. Another disadvantage of long soft tubes is their sensitivity to high pressure, which would lead to an expansion of the soft tubes. This expansion increases the volume and adds a fluidic capacitance (compliance) to the system.
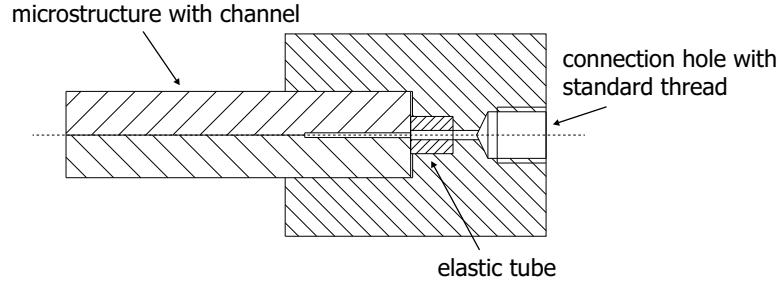
Figure 8.4: Side connector principle with elastomer tubes. For alignment, the microsystem is inserted into a groove and pressed against the tube to achieve sealing. A through hole establishes a connection to a standard fitting.

8.3   Theory

Our objective is to calculate the limits of the proposed connections in term of tightness. When the tube is subjected to a compressive load its length will decrease. The amount of reduction is called total strain (Δl), while the reduction per unit length is called unit strain (ε).

The relation between the unit strain and the total strain is given by

$$\varepsilon = \frac{\Delta l}{l}, \tag{8.1}$$

where l is the initial length of the tube. We apply a load to the tube by pressing a microdevice with its channel opening towards the tube, using a force F (see Fig. 8.5). The maximum load that can be applied to the tube is the load that reduces the tube by l_0, which it the length of the tube's extension. Any additional force is absorbed by the holder and further compression is inhibited since device and holder are in contact. The unit strain of the tube is related to the stress acting onto the tube by the equation

$$\sigma = E\varepsilon, \tag{8.2}$$

where σ is the compressive stress and E is Young's modulus of the silicone tube. Considering that the stress is related to the load given by the following equation

$$\sigma = \frac{F}{A_c}, \tag{8.3}$$

where F is the applied load and A_c is the contact area between the microstructure and the tube defined by

$$A_c = \frac{\pi(d_{out}^2 - d_h^2)}{4}, \tag{8.4}$$
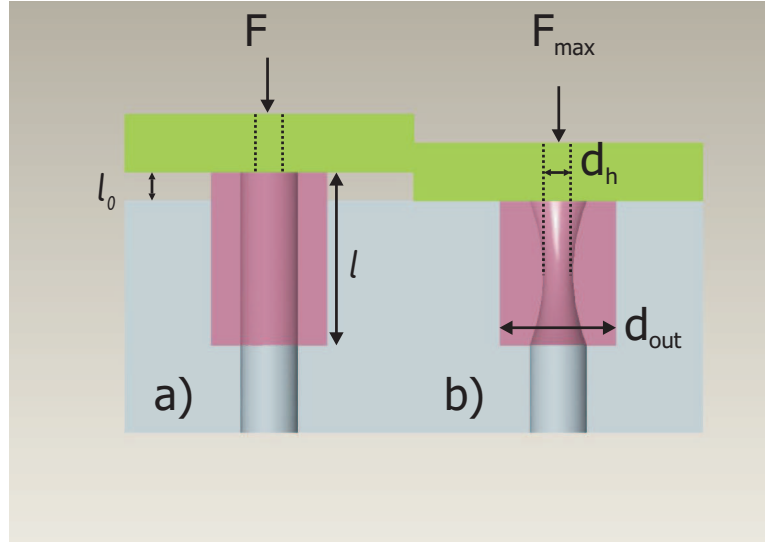
Figure 8.5: A tube with an initial length l (a) is compressed by the maximum applicable force F_{max} about its extension length l_0. l_0 in this case is equal to the total lateral strain Δl.

with d_{out} the outer diameter of the silicone tube and d_h the inner diameter of the microdevice's through-hole, the maximum load $F_{\max}$ applicable to the tube can thus be calculated by

$$F_{\max} = \sigma_{\max} A_c = \varepsilon_{\max} E A_c = \frac{l_0 E A_c}{l}. \tag{8.5}$$

The purpose of a fluidic interconnection is to ensure a sealed contact between the system and the external tube. Of course, to reach a tight contact the pressure of the liquid inside the channel should be the same or smaller than the pressure resulting from the mechanical stress of the sealed connection. From Eq. 8.5 we know that the maximum applicable stress is

$$\sigma_{\max} = \frac{l_0 E}{l}. \tag{8.6}$$

Therefore, the maximum pressure that the liquid may have while still ensuring a sealed connection is

$$p_{\text{liquidmax}} \leq \sigma_{\max} = \frac{l_0 E}{l}. \tag{8.7}$$

The pressure inside a microfluidic channel can be determined by

$$p_{\text{liquid}} = R_{\text{liquid}} Q, \tag{8.8}$$

where R_{fluidic} is the hydraulic resistance and Q is the flow rate [22].
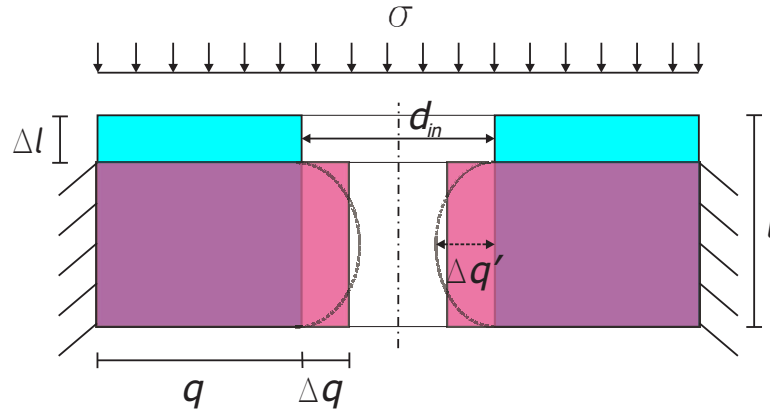
Figure 8.6: An applied stress σ results in a total lateral strain Δq. As a consequence, the tube obstructs further passage once the total lateral strain equals the inner tube diameter. Additionally, a more realistic distribution of the lateral strain is implied by the dashed curvatures.

The hydraulic resistance inside a microfluidic channel with rectangular cross-section depends on its geometry and on the viscosity of the liquid:

$$R = \frac{12\mu L}{wh^3}, \tag{8.9}$$

where L is the length, w the width and h the height of the channel, and μ the viscosity of the liquid.[1]

The internal pressure p_{int} depending on the flow rate Q for a specific channel geometry can then be calculated using

$$p_{\text{int}} = \frac{12\mu L}{wh^3}Q. \tag{8.10}$$

Finally, the above derived relations can be summarized to

$$p_{\text{int}} = \frac{12\mu L}{wh^3}Q < p_{ext} = \frac{F_{max}}{A_c}, \tag{8.11}$$

where A_c is, again, the contact area between connector and device.

Another important consideration concerns the change of the thickness of the tube-wall as a result of the compression of the tube. Fig. 8.6 shows the relation between stress and resulting strain. A load applied to the tube compresses the tube with the initial length l by the total strain Δl. As a consequence of the incompressibility of the elastomeric tube material, the thickness q of the tube-wall will increase by the total lateral strain Δq.

As a result of the tight fit of the tube inside the bottom-flat hole, which prevents any outward expansion, the inner tube diameter d_{in} decreases and

---

[1]Eq. 8.9 is strictly only valid for $w \gg h$

can lead to obstruction of the tube. The relation between lateral strain (ε_l) and axial strain (ε) is

$$\varepsilon_l = -\nu\varepsilon \tag{8.12}$$

with ν the Poisson ratio of the silicone tube.

The total lateral strain, in our case, is equal to the change of thickness of the tube wall Δq.

$$\Delta q = \varepsilon_l q \tag{8.13}$$

where q is the original wall thickness of the tube. Together with Eq. 8.1, we can write

$$\frac{\Delta q}{q} = \nu\varepsilon \Rightarrow \frac{\Delta q}{q} = \nu\frac{\Delta l}{l} \Rightarrow \Delta q = \nu\frac{q\Delta l}{l}. \tag{8.14}$$

Eq. 8.14 shows that a longer tube and a thinner tube wall decrease the risk for obstruction. Regarding the strain, the length of the extension should also be minimized. As mentioned above, however, the applicable hydraulic pressure also depends on the extension length. Therefore, a general rule of thumb for optimized applicable parameters cannot be given, but optimization rather needs to be performed for the individual designs or applications.

In contrast to a simplified rectangular extension geometry as commonly used to derive the theory, the real deformation geometry is more complex and a more detailed treatment is beyond the scope of this work. A more realistic distribution of the lateral strain, however, is a curved profile as depicted by the dashed lines in Fig. 8.6. As a consequence, the total strain is accumulated and increases (denoted $\Delta q'$ in Fig. 8.6). Measurements showed that a safety factor of two in addition to a linear strain calculated from the rectangular model is a sufficient estimate to avoid obstruction.

8.4   Measurements and Results

To be able to compare the tube connector to other connection methods, five different test-chips were developed. Each chip, as schematically shown in Fig. 8.7, consisted of a structured silicon substrate with through-holes. Common MEMS fabrication methods were used to concentrically deposit circular gold-coils around the through-holes onto the substrate surface. Fluidic channels with different geometries and dimensions covering a wide range of fluidic resistances were etched into the backside of the silicon using an advanced silicon etcher (Fig. 8.7b). The channel dimensions for the individual chips and their corresponding hydraulic resistance are listed in Table 8.1. Finally, a glass lid was bonded anodically to the substrate to seal the structure.

	chip 1-6	chip 7-9	chip 10-12	chip13-15	chip 0, 16
channel length (μm)	12	105	105	12	12
channel height (μm)	0.5	0.5	0.25	0.25	0.15
channel width (μm)	100	100	100	100	100
resistance (Pa s/m^3)	2.59E+11	2.53E+12	5.05E+12	5.77E+11	9.62E+11

Table 8.1: Geometric dimensions of the microchannels for the five chip types and their hydraulic resistances (calculations based on Eq. 8.10).

PDMS gasket	**o-ring**	**silicone tube**
length: 20 mm	outer radius: 1.75 mm	outer radius: 0.7 mm
width: 10 mm	inner radius: 1.25 mm	inner radius: 0.3 mm
thickness: 0.42 mm		thickness: 1.22 mm
area: 200 mm^2	**area: 4.71 mm^2**	**area: 1.25 mm^2**

Table 8.2: Dimensions of the different interconnection types. The contact area is used to calculate the stress that has to be applied to achieve a tight sealing

The chip was then inserted into a holder that provided different interconnection types. In this work, we compared o-rings and a PDMS-gasket to silicone tubes. Syringe pumps forced liquid through the chips at various flow rates. To counterbalance the internal pressure calculated from these flow rates using Eq. 8.10, an external stress of the same magnitude was applied to the interconnections. A spring in combination with four screws was used to generate the stress, as depicted in Fig. 8.8. Fastening the four screws resulted in compression of the spring and therefore higher stress applied to the interconnection. Information on the applied stress could be obtained via an integrated force sensor and taking the contact areas of the different interconnections into consideration. Table 8.2 shows the dimensions and the resulting contact areas of the different interconnection types that were tested.

After adjustment of the external stress to balance the internal pressure, the flow rate was increased until leakage was observed. A leakage at the connector-chip-junction was detected by measuring the electrical conductance between adjacent coils. As liquid an aqueous soap solution was used, which, in case of leakage, passed over the coils and immediately resulted in an increased conductance. The distance of 100 μm between the individual coils ensured a high sensitivity even for small leakage rates.

The symbols in Fig. 8.9 show the pressure at which the connections failed and leakage was detected. For each testchip design, corresponding to different pressure ranges, all connection types were tested. Even though different pressure ranges were investigated only the pressures where leakage
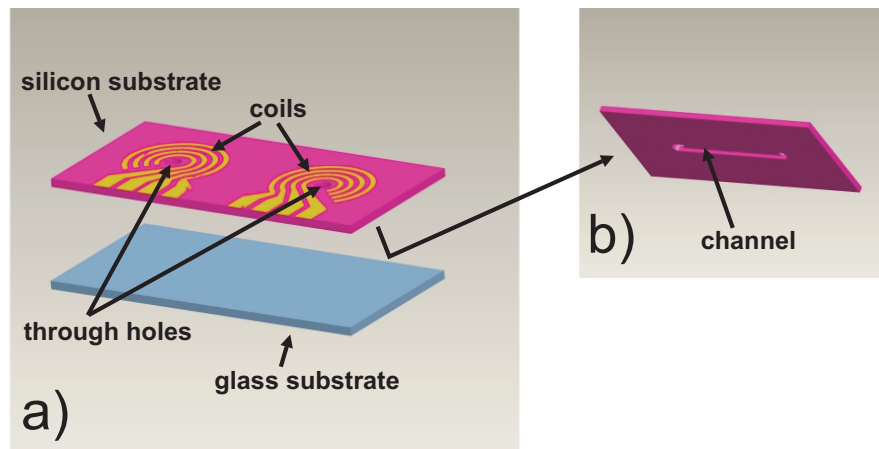
Figure 8.7: Concentric coils around the through-holes were used to measure the conductance and thus detect leakage of the interconnections (a). Channels with different dimensions etched into the backside of the silicon allowed measurements for various fluidic resistances (b).

was first detected for the different connectors are displayed in Fig. 8.9. These pressures are just slightly above the maximum achievable pressures, which cannot be measured directly. What can be seen in Fig. 8.9 is that the theoretical predictions, represented by the lines, are matched nicely by the measured values.

Furthermore, the measurements show that the silicone tubes ensured a sealed contact even at high pressures. No leakage was detected using silicone tubes and applied pressures of up to 1.23 MPa. Meanwhile, o-rings provide a seal until a pressure of 0.14 MPa is reached, whereas PDMS gaskets start leaking already at pressures of 0.01 MPa. In the case of gaskets, the large contact area between the chip and the interconnection requires a high external force to ensure that the external pressure is higher than the internal pressure of the chip, as dictated by Eq. 8.5. This, on the other hand, might deform the package and cause leakage. The silicone tubes, however, show the advantage that they, to a certain extent, can compensate deformation of the package. In fact, the tubes follow deflections of the package maintaining an adherent contact to the chip, while the o-rings seem to suffer from any inhomogeneous distribution of the stress inside the package and a deformation of the structure. A side connector offers the same feasibility with regard to sealing if the applied parameters are equal to those of a through hole connector. The displayed results therefore are also fully valid for side interconnections.
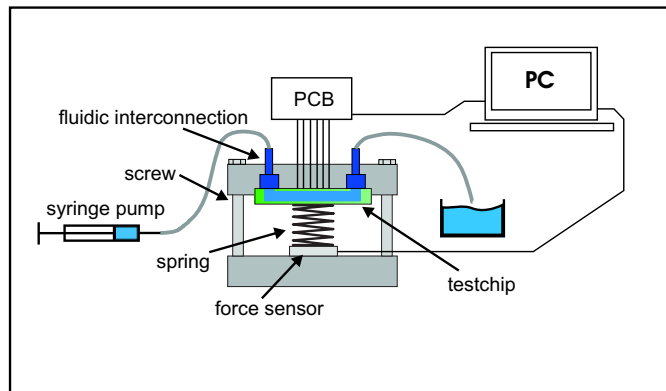
Figure 8.8: Schematic view of the experimental setup: test chips are fitted to different types of interconnections. To be able to measure the stress applied to the different interconnections, a force sensor in combination with a spring and four tightening screws are used.
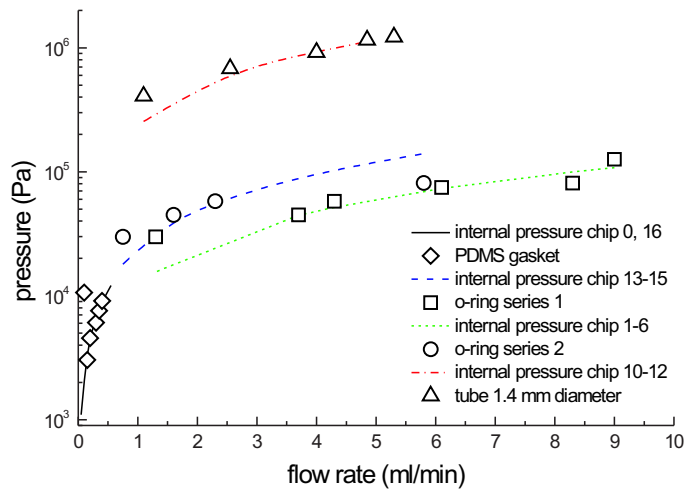
Figure 8.9: The above graph shows the theoretical prediction compared to the measured values for three different types of interconnections: o-rings, PDMS gaskets and tubes. The lines represent the calculated values of the internal pressure for different channel geometries. The datapoints (symbols) represent the maximum measured pressure at which leakage was first detected from the interconnection. For the o-rings two sets of data for different series of test-chips are displayed.

8.5   Conclusion

In this chapter, we presented a fluidic interconnection that allows to fluidically access channels via commonly used through holes as well as via a side connector. A theoretical model was developed that estimated the maximum sealing pressure of various connection types. Further, we designed a test setup to determine the maximum sealing pressure at multiple flow-rates to be able to compare the results with the theoretical predictions. Finally, we showed that the sealing qualities of the tube connectors are superior to those of the other tested interconnections.

8.6   Outlook

Although the presented interconnection represents a straightforward approach some remarks will be made on future topics. Based on the elastomeric tube, a removable, self-adhering connector will be designed that is attached to the microfluidic device. The challenge of this design is to evacuate a chamber inside the connector itself and to use this vacuum to keep the connector in position. Even though this approach is rather a new application than an improvement of the above presented topic, several aspects are taken from the tube connector principle.

Chapter 9

Integration

9.1 The Aim of Integration

The aim of miniaturization was already discussed in Ch. (1). The advantages that can be achieved by integrating multiple functionalities into a single device are accompanied by a high complexity. The problems that can occur based on this complexity are in general expressed by an incompatibility of fabrication methods. The various employed principles that were developed over the years in fluidic handling, detection or sensing showed already as discrete functionalities challenges and were difficult to achieve. Consequently, the focus was put on the development of individual functions and integration issues were neglected and received a low priority. As a result, research groups used many different technologies for fabrication that often are not compatible among each other.

As mentioned earlier, this work tries to assess at this point to develop components with respect to compatibility and integration. In this chapter two applications are presented that use the elements and approaches developed during this project and demonstrate their practical use and capabilities.

9.2 Application Example 1: Berthie - A Polymer Microfluidic Analysis System for the Detection of Ammonia

At the beginning of this PhD project, a microsystem to detect ammonia in aqueous solutions was designed using a colorimetric reaction, the Berthelot reaction.

The concentration of ammonia in water is an important parameter when judging water quality. Building a micro-total-analysis system for ammonia measurements should make a more continuous and widespread control of

ammonia levels in water possible.

The system was fabricated using a one-step photolithographic process as described in Ch. (5) in combination with two different bonding approaches as presented in Ch. (7).
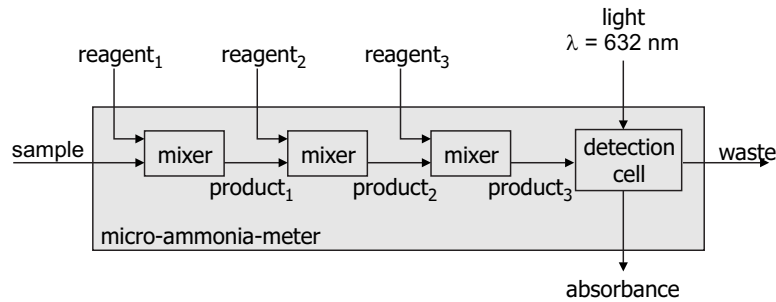
Figure 9.1: Reaction model of the Berthelot reaction: three reagents are successively mixed with the sample and result in a color change of the liquid if ammonia is present, which subsequently can be detected by absorption measurements.

In the microfluidic device, ammonia is detected with a colorimetric method. Ammonia reacts with several reagents to form a blue dye, which in turn is detected by optical absorption measurements. The sequence of necessary reactions is known as the Berthelot reaction, as schematically shown in Fig. (9.1).

Fig. (9.3) shows two versions of the device. The left picture depicts a photolithographically structured SU-8 layer on a silicon substrate that is sealed with a polymer lid. In the right photograph the SU-8 layer is embedded between two PMMA layer using the method described in Ch. (7).

Although the level of integration is relatively low and external devices are required to actually perform analysis, this example shows the combination of fluidics and optics integrated in a single device. Furthermore, simple processes are applied to fabricate the system that prove the individual working principle and compatibility of the used approaches.

inlets for
reagents and
sample

absorbance
cells

mixer waveguides
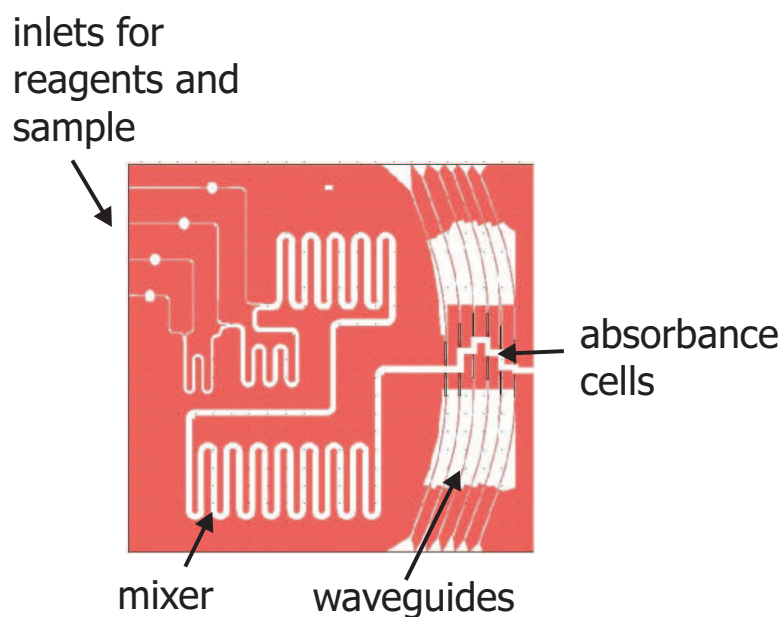
Figure 9.2: Mask design of the Berthelot reaction chip. After the reagents and the sample are introduced into the corresponding inlets mixing is conducted by diffusion in meanders before waveguides provide absorbance detection. The different absorbance cells are for optimizing the optical path length.
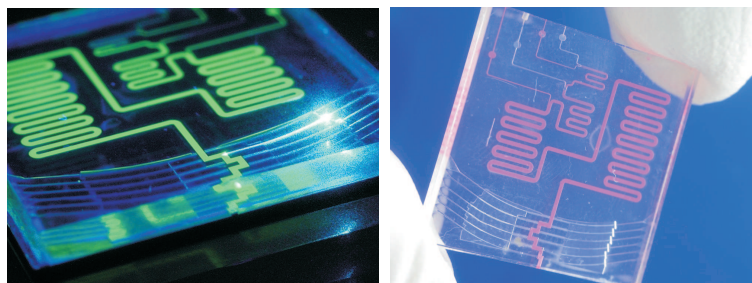
Figure 9.3: Two versions of the Berthie chip. Left: SU-8 on silicon sealed with polymer lid, right: SU-8 embedded between two PMMA layer.

9.3 Application Example 2: BIO**X**TAS- An Integrated Small Angle X-ray Scattering Analysis Chip for Protein Analysis

Proteins are dynamic macromolecules that can undergo conformational changes or form complexes with other biological molecules. Elucidation of these suprastructural features lies at the heart of an understanding of the structure:function relationship [126, 127]. Still, such features are diffi-

cult to investigate using established methods for structural characterization. One reason is that in order to get a comprehensive picture it is necessary to examine the macromolecules under many different solution conditions, which today is very demanding both in terms of time and sample consumption. Here, we describe the development of a system, the so-called bioXtas, combining microfluidics for high-throughput screening of a large solution parameter space while using minute amounts of rare biomacromolecules, and small-angle x-ray scattering (SAXS) as the tool for elucidating suprastructural features and detecting experimental conditions defining borderlines between suprastructural states (see Fig. (9.4) for a conceptual overview). Such a system also has the potential to enable screening of, e.g., formulation of bio-drugs and solubilization of membrane proteins. Thus, rational navigation in the multidimensional experimental space in becomes possible allowing pinpointing of structurally and functionally relevant areas of investigation, borders between various functional states, or structurally stable experimental windows of potentially labile biological systems. Ultimately, the bioXtas system enables time-resolved studies of biological processes, using already established microfluidic techniques [128, 129] in combination with our high-throughput screening.
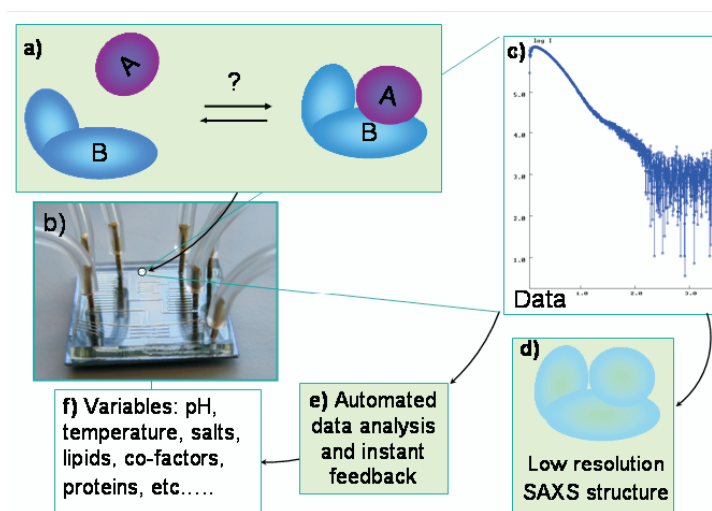
Figure 9.4: Basic principle. A macromolecular biological system of unknown structure (a) is analyzed in the μTAS (b). SAXS data (c) is collected via X-ray exposure through the 200-800 nl analysis chamber. The solution structure of the macromolecular system is determined from the SAXS data (d), and automated data analysis and instant feedback (e) defines the experimental setup (f) for the following analysis.

A microfluidic chip was designed that features an integrated X-ray transparent sample channel (200 nl internal volume) and online mixing of liquids. The device was fabricated in polystyrene using double-sided micromilling and was sealed applying a plasma enhanced bonding method (see Ch. (7)). The chip was fixed onto a holder that was provided with fluidic interconnections allowing easy access of liquid and a sealed connection even in vacuum, as depicted in Fig. (9.5).

First successful protein measurements have been performed using a synchrotron X-ray source (MaxLab, Lund, Sweden). Online change of the buffer concentration determining structural changes of the protein have been conducted. An example of a 3D view of a protein generated from the data collected with the BIOXTAS chip can be seen in Fig. (9.6).
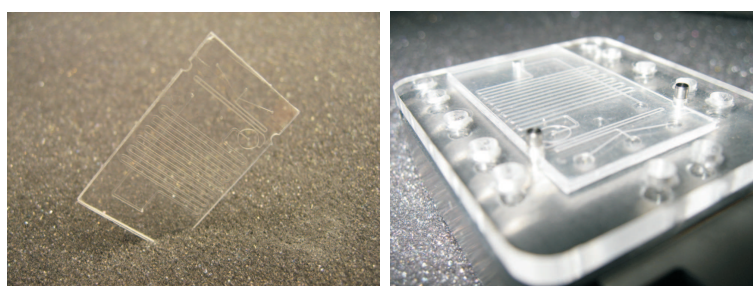
Figure 9.5: BIOXTAS chip fabricated by micromilling and sealed with plasma-enhanced thermal bonding (left) and chip placed aligned inside a holder for application inside a vacuum chamber.

9.4 Conclusion

Both examples show the high impact miniaturization has on chemical and biological analyses. The Berthie chip combines fluidic handling with optical detection and allows rapid determination of ammonia concentration consuming only a fraction of the sample volume conventional analyses would require.

The BIOXTAS chip provides a promising platform for the analysis of protein structures. The novelty is that structural changes can be determined in real-time under changing conditions. The first step is made and the experimental procedure was proven.
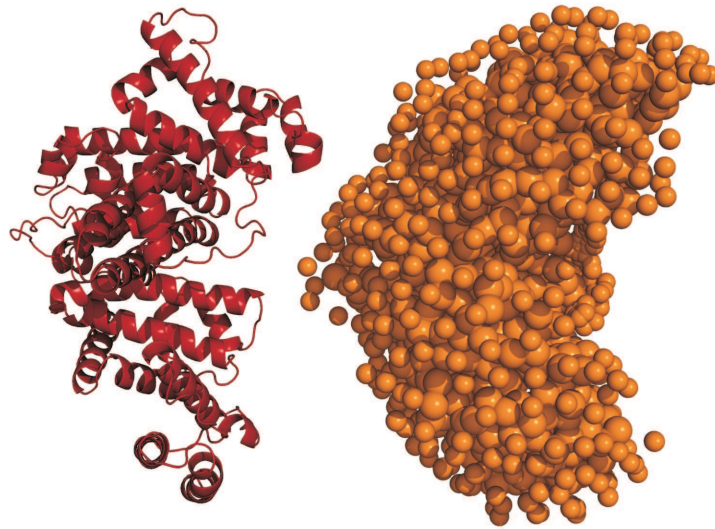
Figure 9.6: Structural view of a BSA proteine (Bovine Serum Albumine). Left: illustration from literature, right: produced from the data measured with the described BIOXTAS chip (courtesy of Bente Vestergaard, DFU).

Chapter 10

Conclusion

In this work, various components and principles to establish integrated lab-on-a-chip systems were developed and investigated.

In-plane detection cells with integrated waveguides could alleviate the limitations with respect to sensitivity that were based on short optical pathlengths and the relatively small amount of optical power coupled into the fluidic channels. Geometrical shaping of the waveguide-channel interface including tapers and lenses helped increase the amount of optical power that was utilized for measurements. A simple analytical model was compared to experimental data demonstrating the optimization of signal-to-noise ratios as a function of the pathlength using different integrated collimator and lens structures. Furthermore, two novel methods for fabrication of microfluidic systems with integrated optical waveguides were developed. Direct micromilling enabled us to fabricate $100\,\mu\mathrm{m}$ wide optical waveguides. Propagation losses of less than $1\,\mathrm{dB/cm}$ could be achieved throughout the entire visual range down to a wavelength of $400\,\mathrm{nm}$. A casting process amenable to high number production of such devices was furthermore investigated.

For fluidic handling, a novel, inexpensive polymer-based valve approach was presented that allows the combination of a check valve's rectifying properties with the possibility to actively control the flow rate in the forward (open) direction. Experimental characterization showed good alignment with a simple theoretical model. Moreover, two check valves together with an actuator were combined to a micropump that showed promising potential in first tests.

Beside that, a newly developed active valve approach showed high integrational capabilities and enables to easily distribute liquid on the microscale level. Although full characterization of the device could not be completed during this project, preliminary results are promising.

For packaging of microfluidic devices, an interconnection that allows to fluidically access channels via commonly used through holes as well as via a side connector is presented. A theoretical model was developed that esti-

mated the maximum sealing pressure of various connection types. Finally, we showed that the sealing qualities of the tube connectors are superior to those of other tested interconnection types.

Several polymer bonding methods were investigated and optimized. An adhesive based bonding method was invented that allowed combining conventionally structured polymer lids with cleanroom fabricated features. The strength of thermal and plasma enhanced thermal bonds were furthermore quantified depending on various parameters.

All developed components or functionalities can be produced using conventional polymer fabrication methods and the individual functions can be utilized to operate as discrete elements. Their compatibility, however, allows to combine these elements individually and furthermore their integration into a single device. Consequently, lab-on-a-chip systems can be economically produced that contain all necessary components to provide manifold functions and analysis.

Chapter 11

A Vision for the Near Future

Even though several components were presented during this work that allow easy integration and fabrication, the limited time did not allow to perform the actual fabrication of an integrated device. However, the required elements and methods are available at the end of this thesis and, in fact, the realization of an integrated μTAS has already been started while finishing this report. Apart from the optimization of the individual components, as described earlier in the corresponding chapters, thus the fabrication of a monolithic platform is a challenge and great improvements compared to hybrid devices are expected.

The development of the bioXtas application, as described in Ch. (9), will be continued and the impact that the integration of the presented elements have on the performance of the device will be demonstrated. The integration of micropumps directly onto chip level will minimize the required sample volume to a level that never before has been applied to small angle x-ray analyses of proteins. The compliance of the system will be dramatically reduced and consequently the response time of the system will be decreased. This allows rapid change of conditions and real time analyses of protein structures under these changing conditions.

The simplicity of the tunable check valve motivates to use the device to continuously control and fine tune the flow-rates. However, further investigations are necessary to estimate if, for instance, the pulses generated by the micropump can be eliminated using this approach.

The active microvalve based on the hydraulic principle will, after successful adaption to the integrated platform, allow to control the distribution of liquids inside a compact microfluidic device. Hence, the grade of automation is increased and a first step towards high throughput screening of bio-chemical samples is made.

Optical waveguides will be used in the bioXtas application to detect concentration changes or, in two phase liquid systems, to identify phase changes and provide an active feedback to allow a closed loop control.

Apart from demonstrating what integration offers for bio-chemical analysis, a second focus will be put on the optimization of the fabrication processes. The presented methods were developed aiming at simple procedures and compatibility. The proven casting of waveguides already gave a taste of how mass production techniques can substitute a rapid prototyping method used in research. In general, all micromilled structures can be produced using casting, embossing or molding technologies. It is therefore reasonable, in a next step, to employ these methods to prove the possibilities of high integrated, economically produced lab-on-a-chip devices.

Furthermore, the developed elements can be used as discrete components. Providing a sufficient packaging enables to establish individual parts, not unlike those known from electronics. An expandable toolbox that allows easy breadboard-like connection of the parts and building adaptable circuits represents a flexible solution for the research field as well as for certain industrial applications.

Appendix A

Apparatus and Materials

A.1 Passive microvalve

To obtain the detection limit of the flow measurements, the flow determined by the pressure measurements was compared with a theoretical value. To do this, a certain pressure was applied to the system. The flow was then measured with the setup for a certain time. The volume that passed the system was determined by measuring the column length of the liquid inside a tube with a known inner diameter that was mounted behind the outlet. The volume divided by the time gave an additional value for the flow-rate that could be compared with the directly measured flow-rate.
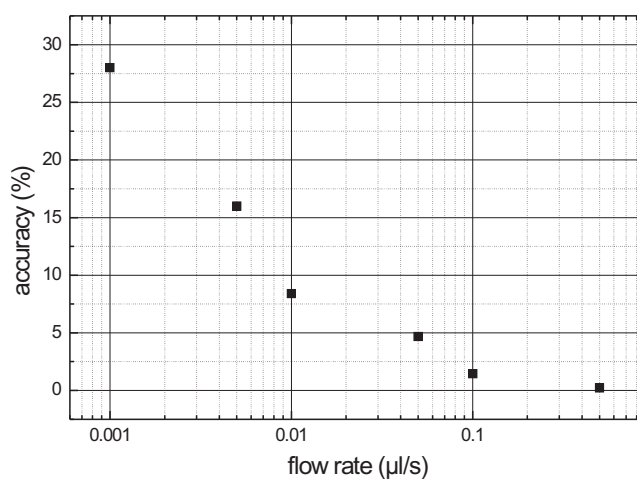
Figure A.1: Accuracy of flow measurements depends on the measurement range.

Appendix B

Micromilling of fluidic devices

B.1 Introduction

In the course of this project, micromilling was established as a versatile tool for structuring of microdevices at the Department of Micro and Nanotechnology, MIC. A lot of effort was put into setting up and modifying the machine and optimizing the parameters to obtain the necessary precision for microfabrication. Although a scientific investigation of the micromilling process itself was not subject of this work, this section accounts for the time that was invested to establish micromilling for rapid prototyping of microfluidic devices.

Although a lot of MEMS devices require cleanroom facilities to fabricate them, recently a trend towards alternative fabrication methods and materials can be seen. Especially in the field of lab-on-a-chip systems the demand for single-use devices requires economical production. In a lot of cases the accuracy that can be obtained in the cleanroom is not necessary for microfluidic devices. Many of these systems contain only passive elements such as single microchannels, reaction chambers or mixing meanders and are far from being complicated devices. Using cleanroom processes to fabricate channels in the $100\,\mu$m range is exaggerated and not economical. Furthermore, in research often multiple changes in the design of the prototypes are necessary and design changes applied to photolithography are time consuming processes.

Several groups showed the advantages that laser ablation has as a rapid prototyping tool in the field of microtechnology. Micromilling represents another technology that has the capability to realize prototypes and small volume production, also in the research field. Even though it is a common method for fabrication of embossing tools, it still is treated stepmotherly and has the reputation to be too "workshop-like". Micromilling offers the

capability of quick design changes, allows direct three-dimensional machining and represents an economic solution for many applications. With tools available in the range of a few micrometers and drives that have an accuracy in the sub-micrometer range, it is possible to directly produce precise prototypes for many applications. Apart from that, the material choice is not limited to one material group but ranges from metals over polymers to glass.

The aim of this work is not to dispute the potential of cleanroom work or any other well established fabrication method, but to demonstrate an interesting alternative for the microtechnology area.

With this section we would like to give an overview of the capabilities micromilling can contribute to the field of micromachining in general and to the field of lab-on-a-chip systems in particular. We will give a short introduction into the used terminology and an overview over the available technology. Subsequently, we discuss the software that is necessary to control the machines and finally we will show how to use a micro-milling machine to obtain the desired structures.

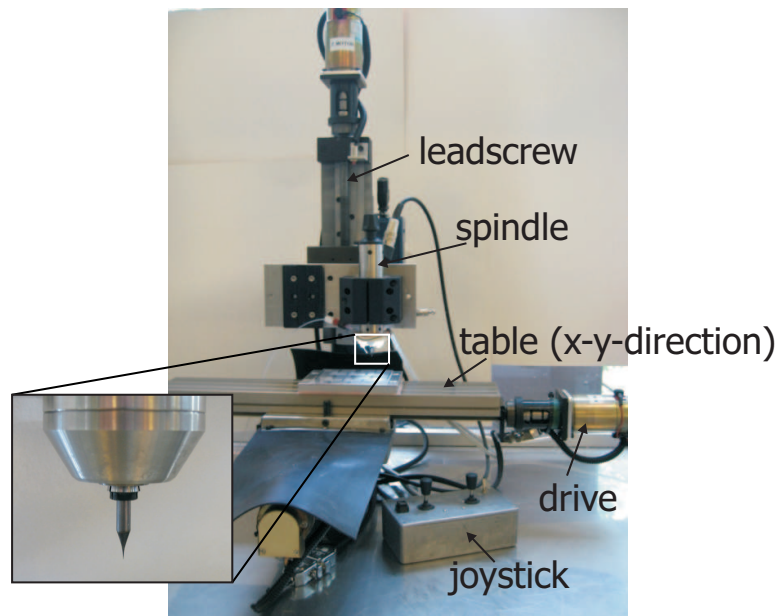## B.2 The machine and the tools

B.2.1 The Machine

Figure B.1: Modified commercially available CNC milling machine.

Fig. (B.1) shows a photo of a micromilling machine with the related

terms used in this project. The main parts are the x-y-table, the z-axis and the spindle. The axes are usually driven by motors attached to leads crews. In general, two types of motors are available, steppers and servos. Stepper motors have the advantage that they can be easily controlled by a computer. Servos, on the other hand, need additional encoders to obtain their angular position. These encoders, however, can be used for feedback control of the position to establish a closed loop and thereby increase the accuracy. The high velocity servos offer is, in contrast to industrial applications, not of great importance in micromachining due to the small path lengths.

Discussing micromilling, the first question is the accuracy that can be reached, and, in the microtechnology field, what the minimum feature size is that can be realized. The minimum width of a directly milled channel depends, first and foremost, on the diameter of the used milling-tool. However, the fabrication of deep channels, for instance, is divided into multiple steps, cutting a certain amount deeper with each step. A great repeatability is therefore important to guarantee the same cutting contour for each step and thereby the smallest possible channel width.

The minimum width of a free-standing ridge, on the other hand, depends on the precision of the machine itself. Excentricity and vibration of the tool have a great impact on the possible dimensions of thin structures.

The Leadscrew

To transform the rotational movement from the motors to a linear movement of the x-, y- or z-axis, leadscrews are used. Standard models use metal leadscrews in combination with a brass or polymer leadscrew nut. Although lubricants can be used to minimize friction and wear, the use of this technique leads to increasing clearance. The clearance between the nut and the leadscrew can be adjusted to a certain extent by fastening the nut, which is, again, associated with higher abrasion.

All clearances in the drive mechanism lead to so-called backlash. The backlash becomes important at direction changes of the leadscrews and leads to geometry errors in the fabricated features. Especially curvatures are difficult to reproduce smoothly with systems suffering from backlash.

Linear ball-screw units can prevent this phenomenon and offer long, tolerance-free life time. However, the pitch of ball-screw units is larger in comparison to the pitch of conventional leadscrews. This results in lower resolution per rotation. Another method to compensate the backlash are two oppositely screwed nuts that induce a force against each other. The flanks are tolerance-free on both sides of this counternut. However, increased friction and ,as a result, a higher abrasion are the disadvantage of this method.
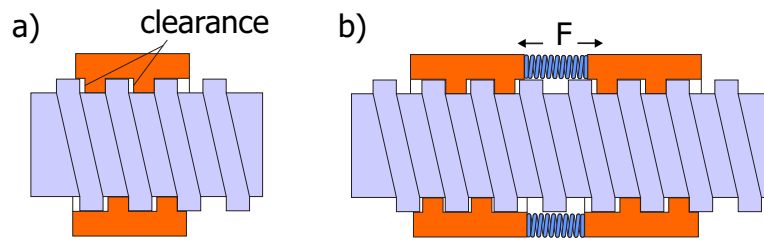
Figure B.2: a) due to wear a certain clearance can be found between the threads of the screw and nut. If the leadscrew changes its direction, this clearance results in a backlash of the nut. b) two nuts are screwed oppositely to each other onto the leadscrew establishing a force between the nuts thereby compensating the backlash using the counternut principle.
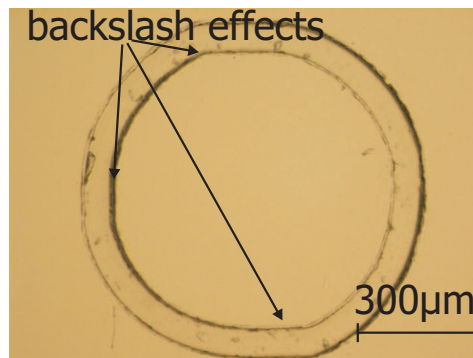
Figure B.3: The consequences of backlash can be clearly seen cutting round geometries: at the dead centers of the circular movement, which coincides with the direction change of the x and y axes, the milling tool cuts a straight instead of a curved contour.

The Spindle

Since the tool diameters are very small, high rotational velocities are necessary to perform sufficient cutting speeds, which is where conventional electro-motors reach their limit. Attached gears can increase the speed but also add vibrational components that should be avoided to not destruct the tools or the structures. High speed spindles were therefore developed, not unlike those used by dentists to bother the patient with their characteristic sounds. These spindles, which avoid the use of any additional gear, can be divided into two major groups based on their drive principle. High frequency spindles are driven by a high frequent current, while air turbines use a pressured air flow. Both principles allow rotational speeds larger than 100000 rpm and are available with maintenance-free bearings. While usually air turbines are usually more economical, high frequency spindles allow for continuous variable speed and also torque control. The spindle's concen-

tricity defines the smoothness of the cut and is therefore not less important than the precision of the linear stages. Further, a non-concentric spindle axis increases the width of the tool path cut into a material and leads to higher wear or even destruction of the tools. Therefore, also precisely machined collets and chucks are essential. Also, just small eccentricities lead, at high rotational speeds, to oscillations that might destroy the tool.

Commonly, two mechanisms are used to fasten the tool in the spindle. While the first approach uses coupling nuts, which have to be fastened with appropriate wrenches, the second method allows to fasten the tool with a central screw without the need of additional tools.

B.2.2 The Tools

Micromilling tools are available from various manufacturers down to diameters below $5\,\mu$m. Fig. (B.4) shows impressively the small available tool dimensions. The tools differ in geometry, grade and coatings depending on the applications and materials they can machine. While the most commonly used tool geometries are end-mills that cut rectangular grooves, ball-end mills result in hemispherical channels. The latter type is, for instance, also used for 3D milling of round shapes. Apart from that, manifold variations are available. For further information, we refer to the appropriate manufacturer catalogues.

For milling of polymers, a tool with a low number of teeth (for instance 2) should be used to allow easy removal of chips and heat.
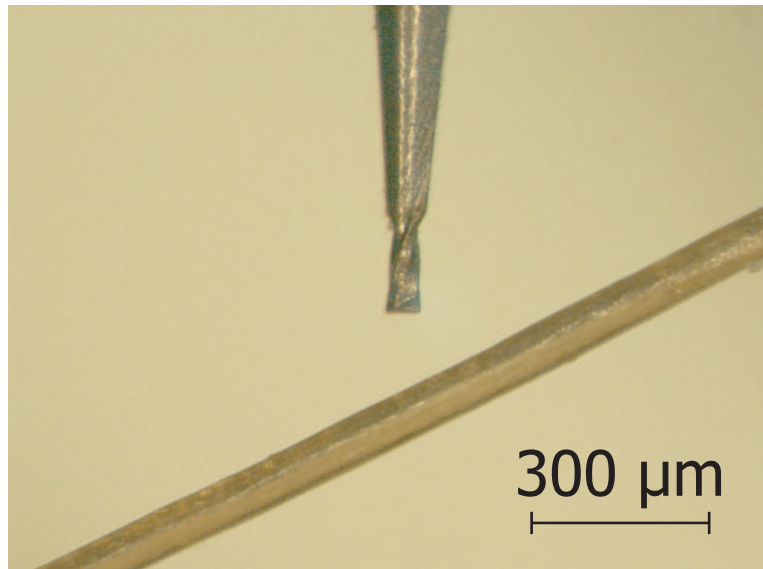
Figure B.4: $50\,\mu$m end-mill compared to the a human hair.

B.2.3 The Parameters

Milling is a machining process that cuts material with geometrically defined cutting edges.
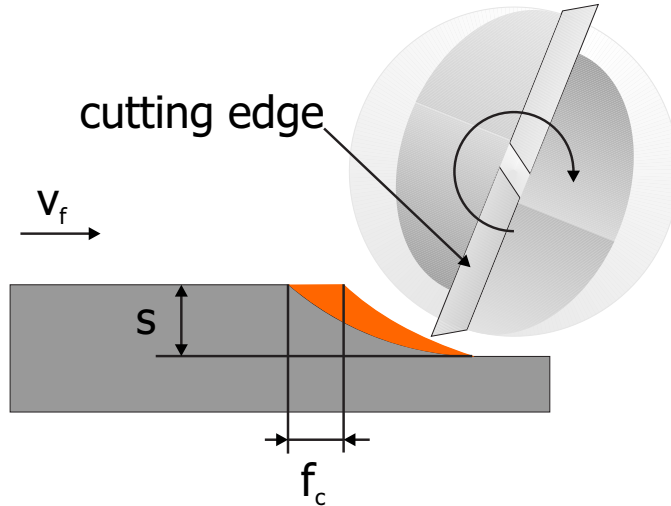
Figure B.5: Principle of the milling procedure: the rotating end-mill moves relative to the workpiece with the feed-rate v_f. The cutting feed f_c describes the amount of material one cutting edge cuts away per rotation.

The main parameters that have to be set for the milling process are the rotational velocity of the spindle n, called spindle-speed, the translational velocity v_f of the milling tool in x- and y-direction, called feed-rate, and finally the plunge-rate that describes the velocity of the tool in z-direction.

To determine these parameters another value, the feed f, is introduced. The feed per revolution is defined by:

$$f = f_c c, \tag{B.1}$$

with f_c the feed per cutter and c the number of cutters per tool. The values for f_c are depending on the tool diameter, the tool material and the substrate material and can be looked up in tables. However, the tables only give an estimate and for optimum results these might have to be adapted to the individual setup.

Another characteristic value is the cutting speed v_c of the tool in certain materials, which can also be found in tables. The relation between the revolution velocity of the tool n and the cutting speed is defined as:

$$n = \frac{v_c}{\pi d}, \tag{B.2}$$

with d the diameter of the tool.

material	v_c	plunge ratio (x diameter)	f_c (% of tool diameter)
low alloyed steel	40...100	0.05...0.1	0.3...1
highly alloyed steel	30...60	0.05...0.1	0.3...1
copper alloy (brass, etc.)	120...160	0.04...0.1	0.3...1
aluminum alloy	140...260	0.06...0.12	0.5...2
polymers	240...260	0.1...0.15	0.7...3

Table B.1: Feed-rates for movements in the x-y plane. For plunge-rates, however, v_c has to be reduced by a factor between 50 and 90%, depending on the number of tooth and the materials

The feed rate v_f of the tool can then be derived from:

$$v_f = nf. \tag{B.3}$$

Inserting B.1 and B.2 we can conclude:

$$v_f = nf = cf_c\frac{v_c}{\pi d}. \tag{B.4}$$

For "macro" milling machines tables exist listing recommended values for various materials, which, however, cannot directly be applied to the micro world. Mainly due to temperature influences the parameter values have to be decreased when working in the micro range.

The values listed in Tab. (B.2.3) are, in general, for guidance. Various parameters influence the actual settings and optimization has to be conducted individually. Considering, for instance, the listed cutting velocity v_c, small tool diameters require a high rotational speed. The possible spindle speed therefore is a major limiting factor. Generated heat, on the other hand, is another disadvantage of high rotational speed, which is discussed further below.

B.3   The Software

To realize a structure from idea to the real device, a 3-step software process is necessary. This means that three software levels are used to go from the design to the machining process.

First, the desired geometry is drawn in a CAD (Computer Aided Design) program. This geometry is then translated into a CAM (Computer Aided Machining) software, in which the designated parameters are configured. The CAM software generates a standardized code, the so called g-code, that

has been developed to automatically control machines. The g-code is read by a software that controls the machine. The controller software allows further to manually control the machine and adapt the parameters manually that were set in the CAM process. Further, modern controller softwares allow a software-based backlash compensation. Although this is not a replacement for a precise linear drive, in a certain range, this can be used for adjustment.

B.4 The Micromilling Procedure

The theory of micromilling is described elsewhere and is not covered in this work. Rather some more unique techniques are discussed that further facilitate the use of micromilling and address the fabrication of multilayer microfluidic structures.

B.4.1 Fixing Substrates

Mounting thin substrates with small dimensions onto the x-y table constitutes an ordinary problem during operation. Clamping jaws as commonly used in conventional machining do not allow structuring of the entire substrate surface. Furthermore, jaws tend to bend a substrate or even deform it due to the large applied forces. Since in micromilling the occurring lateral forces on the substrate that are generated by the cutting process are low due to the small tools, a good alternative to jaws are vacuum chucks or double sided adhesive tapes. Using the latter approach, however, a homogeneous layer thickness has to be ensured to allow accurate milling in the x-y-plane.

B.4.2 Double Sided Structuring

Double sided structuring of substrates requires an alignment approach. In the following, an attempt is describes that was often used during this work.

Onto the milling machine table, a support polymer plate was mounted. Onto this plate, the substrate was fixed using removable double-sided tape. After structuring the first side, two alignment holes (diameter 2 mm) were drilled through the substrate into the support plate before the substrate was removed. Two dowel pins were then inserted into the holes of the support and the substrate was mounted again upside down. It has to be noted that the alignment holes have to be symmetric to the axis the substrate is rotated around. During structuring of the second substrate side, the dowel pins are removed again. This method allowed precise aligned double sided structuring.

B.4.3 Cooling

Similar to industrial milling, also in micromachining the substrates have to be cooled during the milling process. The high rotational speed generates heat that is applied locally and has to be transported away from the machining area. The used materials, e.g. polymers, often have a lower heat conductance in comparison to metals so that the removal of thermal energy has to be supported. Apart from the adequate settings of the spindle speed and feed-rate, the choice of a proper coolant is of major importance. In industrial metal fabrication, often harsh chemicals are used that show excellent cooling properties and prevent corrosion. Since for our cases the substrate material often is a polymer, these chemicals should be omitted. Instead, aqueous solutions with added soap showed good properties. The result of an insufficiently cooled tool is depicted in Fig. (B.6).
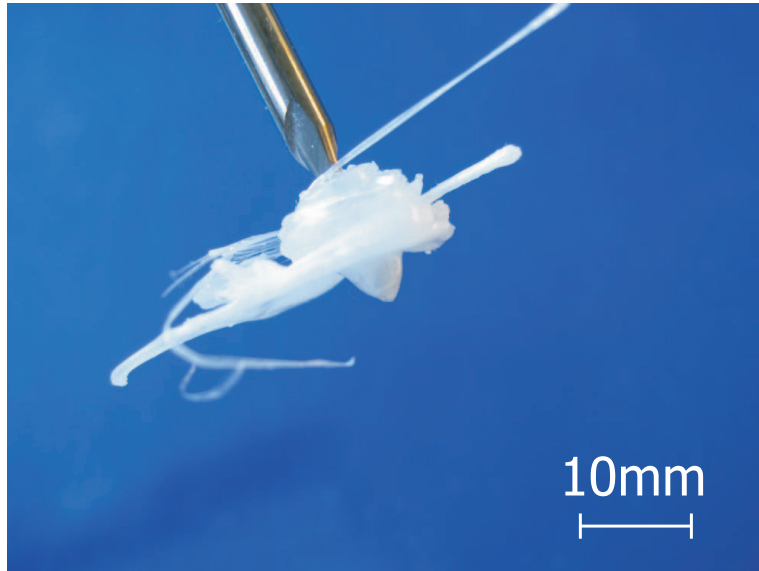
Figure B.6: Polymer (polystyrene) melted during the milling process due to insufficient cooling.

B.4.4 Material

In this project, in particular the following polymers were structured using micromilling: polymethylmathacrylate (PMMA), polystyrene (PS), polyvinylchloride (PVC), polycarbonate (PC) and teflon.

In general, it was observed, that the less ductile a polymer was, the better was its machinability. Especially the generation of burr is less significant for a brittle polymer than for soft plastics. The fact that a lot of polymers contain softeners to increase impact resistance, i.e., by increasing

their ductility, has thus to be considered. Another factor is the glass transition temperatures of the material. Polymers with low glass temperature tended to melt during the milling process, which, in some cases, even could not be avoided using proper cooling. In particular, PMMA and PS showed good machinability, while PC and PVC showed unsatisfactory machinabilities. Teflon generated burr, but was otherwise reasonably well structurable by micromilling.

B.5 Conclusion

This section gave an overview of milling applied to the field of microtechnology. During the work, it was shown that micromilling offers the capability to structure substrates in the micrometer range. Optimizing the milling parameters, precise geometries can be achieved and it is even possible to rapidly prototype optical elements. This very flexible fabrication method was further used to manufacture the majority of the devices designed in this thesis and often first made it possible to investigate all the different approaches.

Appendix C

Publications

C.1 Peer-reviewed Papers

- "A fast and reliable way to establish fluidic interconnections to planar microchips", **D. Snakenborg**, G. Perozziello, O. Geschke and J. P. Kutter, submitted to *Journal of Micromechanics and Microengineering*

- "Direct milling and casting of polymer-based optical waveguides for improved transparancy in the visible range", **D. Snakenborg**, G. Perozziello, H. Klank, O. Geschke and J. P. Kutter, *Journal of Micromechanics and Microengineering*, **16**, 2006, 375-381

- "AC electroosmotic pump with bubble-free palladium electrodes and rectifying polymer membrane valves", A. Brask, **D. Snakenborg**, J. P. Kutter and H. Bruus, *Lab-on-a-chip*, 2006

- "Lab-on-a-chip with integrated optical transducers", S. Balslev, A.M. Jorgensen, B. Bilenberg, K.B. Mogensen, **D. Snakenborg**, O. Geschke, J.P. Kutter, A. Kristensen, *Lab-on-a-chip.*, 2006, **1**, 213 - 217

- "Microstructure Fabrication with a CO_2 Laser System", **D. Snakenborg**, Henning Klank and Jörg P. Kutter, *Journal of Micromechanics and Microengineering*, **14**, 2004, 182-189

- "Measurements of scattered light on a microchip flow cytometer with integrated polymer-based optical elements", Z. Wang, J. El-Ali, M. Engelund, T. Gorsæd, I.R. Perch-Nielsen, K. B. Mogensen, **D. Snakenborg**, J.P. Kutter, A. Wolff, Lab-on-a-chip, **4**, 2004, 372-377

C.2 Conference Contributions

- "Polymer microvalves with pre-stressed membranes for tunable flow-pressure characteristics", **D. Snakenborg**, H. Klank and J. P. Kutter, Oral presentation to be given at μTAS, November 5-9, 2006, Tokyo, Japan

- "A fluidic motherboard including fluidic and optical interconnections, having modular functionality for optical analysis in microfluidic systems", G. Perozziello, **D. Snakenborg**, Z. Zhang, J. P. Kutter, K. F. Jensen and O. Geschke, Oral presentation to be given at μTAS, November 5-9, 2006, Tokyo, Japan

- "SAXS in a μTAS - a new approach to structure: function studies of biological macromolecules", B. Vestergaard, L. Arleth, **D. Snakenborg**, K. Toft, J. Jacobsen, J. M. Flink, M. Gajhede and J. P. Kutter, Poster presentation to be given at μTAS, November 5-9, 2006, Tokyo, Japan

- "Micromilling as a fabrication method for miniaturized analytical systems", D. Stadnik, **D. Snakenborg**, J. P. Kutter, A. Dybko, Oral presentation given at the 9-th Scientific Conference, Optoelectronic and Electronic Sensors COE 2006, Kraków - Zakopane June 19-22, 2006

- "Novel, fast and flexible methods for fabrication of polymer-based optical waveguides", **D. Snakenborg**, G. Perozziello, O. Geschke and J. P. Kutter, *μTAS 2005*, October 9-13, 2005, Boston, USA

- "Optical connector plugs for multiplexed and simultaneous detection purposes in microfluidic systems", G. Perozziello, Zhiyu Zhang, **D. Snakenborg**, J. P. Kutter, K. F. Jensen and O. Geschke, *μTAS 2005*, October 9-13, 2005, Boston, USA

- "Integration of fluidic, optical and thermal elements to realize Lab-on-a-Chip systems for analysis of ammonia in aqueous samples" **D. Snakenborg**, Henning Klank and Jörg P. Kutter, *LabAutomation conference*, San Jose, California, Jan 30 - Feb 3, 2005

- "Biochemical Assays in Microsystems via Bead Velocity Measurements using Integrated Waveguide Arrays", Henning Klank, Thorbjørn Andersen, Klaus B. Mogensen, Fredrik Eriksson, **D. Snakenborg** and Jörg P. Kutter, *MicroScale Bioseparations (MSB) 2005*, New Orleans, LA, USA, Feb 13-17, 2005

- "Integration of Optical and Fluidic Elements on Microsystems: Challenges, Benefits and Applications", J. P. Kutter, K. B. Mogensen,

D. Snakenborg, F. Eriksson, Ó. Gústafsson, H. Klank, *ISMM 2004*, November 24-26, 2004, Takamatsu, Japan

- "μTAS with Integrated Optical Transducers", S. Balslev, B. Bilenberg, O. Geschke, A. M. Jorgensen, A. Kristensen, J. P. Kutter, K. B. Mogensen, **D. Snakenborg**, μTAS 2004, September 26-30, 2004, Malmö, Sweden

- "Microsystems with Integrated Optical Elements for Chemical and Bio/chemical Applications", K. B. Mogensen, F. Eriksson, **D. Snakenborg**, Ó. Gústafsson, R. P. H. Nikolajsen, H. Klank, J. P. Kutter, *MNE 2004*, September 19-23, 2004, Rotterdam, The Netherlands

- "Integration of optics and microfluidics for a lab-on-a-chip system" A. M. Jorgensen, S. Balslev, B. Bilenberg, O. Geschke, A. Kristensen, J. P. Kutter, K. B. Mogensen, **D. Snakenborg**, *Pittcon 2004*, March 7 - 12, 2004, Chicago, Illinois

- "Multilayer PMMA Microfluidic Systems for Ammonia Detection", H. Klank, **D Snakenborg**, R. P. H. Nikolajsen and J. P.Kutter, *MINIT*, Potsdam, Germany, 3-4 December 2003

- "Optimization of Signal-to-Noise Ratio in Absorbance Detection by Integration of Microoptical Components", **D. Snakenborg**, K. B. Mogensen and J. P. Kutter, *The 7th International Conference on Miniaturized Chemical and Biochemical Analysis Systems (μTAS 2003)*, Squaw Valley, California, 5-9 October 2003, 841-844

- "Combining separation functionality and integrated optical detection on microfabricated devices", invited oral presentation Jörg P. Kutter, Klaus B. Mogensen, **D. Snakenborg**, Nickolaj J. Petersen and Rikke P.H. Nikolajsen Analysdagarna, Gothenburg, Sweden, June, 2003

- "Rapid Production of Multilayer Plastic Microfluidic Systems", Henning Klank, **D. Snakenborg**, Oliver Geschke, Jörg P. Kutter, *LabAutomation 2003*, Palm Springs, USA, February, 2003

Bibliography

[1] A. Manz, N. Graber, and H. Widmer, "Miniaturized total chemical analysis systems. a novel concept for chemical sensing," *Sensors and Actuators, B: Chemical*, vol. B1, no. 1, pp. 244–248, 1990.

[2] D. Laser and J. Santiago, "A review of micropumps," *Journal of Micromechanics and Microengineering*, vol. 14, no. 6, pp. R35–R64, 2004.

[3] P. Woias, "Micropumps - summarizing the first two decades," *Proceedings of SPIE - The International Society for Optical Engineering*, vol. 4560, pp. 39–52, 2001.

[4] W. O. Kwang and H. A. Chong, "A review of microvalves," *Journal of Micromechanics and Microengineering*, vol. 16, no. 5, p. R13, 2006.

[5] J. P. Kutter and Y. Fintschenko, *Separation Methods in Microanalytical Systems*. CRC Press, 2005.

[6] E. Verpoorte, "Chip vision - optics for microchips," *Lab Chip*, vol. 3, pp. 42N–52N, 2003.

[7] O. Rotting, W. Ropke, H. Becker, and C. Gartner, "Polymer microfabrication technologies," *Microsystem Technologies*, vol. 8, no. 1, pp. 32–36, 2002.

[8] A. de Mello, "Plastic fantastic?," *Lab-on-a-chip*, vol. 2, pp. 31N–36N, 2002.

[9] S. Quake and A. Scherer, "From micro- to nanofabrication with soft materials," *Science*, vol. 290, no. 5496, pp. 1536–1540, 2000.

[10] H. Andersson and A. van den Berg, "Microfluidic devices for cellomics: a review," *Sensors and Actuators B: Chemical*, vol. 92, no. 3, pp. 315–325, 2003.

[11] S. Mouradian, "Lab-on-a-chip: applications in proteomics," *Current Opinion in Chemical Biology*, vol. 6, no. 1, pp. 51–56, 2002.

[12] N. Lion, T. Rohner, L. Dayon, I. Arnaud, E. Damoc, N. Youhnovski, Z.-Y. Wu, C. Roussel, J. Josserand, H. Jensen, J. Rossier, M. Przybylski, and H. Girault, "Microfluidic systems in proteomics," *Electrophoresis*, vol. 24, no. 21, pp. 3533–3562, 2003.

[13] J. Rossier, F. Reymond, and P. Michel, "Polymer microfluidic chips for electrochemical and biochemical analyses," *Electrophoresis*, vol. 23, no. 6, pp. 858–67, 2002.

[14] U. Bilitewski, M. Genrich, S. Kadow, and G. Mersal, "Biochemical analysis with microfluidic systems," *Analytical and Bioanalytical Chemistry*, vol. 377, pp. 556–569, 2003.

[15] A. de Mello and R. Wootton, "But what is it good for? applications of microrector technology for the fine chemical industry," *Lab-on-a-chip*, vol. 2, pp. 7N–13N, 2002.

[16] A. v. d. Berg and T. S. J. Lammerink, "Micro total analysis systems: Microfluidic aspects, integration concept and applications," *Topics in Current Chemistry*, vol. 194, pp. 21–50, 1998.

[17] S. Büttgenbach and C. Robohm, "Microflow devices for miniaturized chemical analysis systems," *Proceedings of SPIE - The International Society for Optical Engineering*, vol. 3539, pp. 51–61, 1998.

[18] M. Elwenspoek, T. Lammerink, R. Miyake, and J. Fluitman, "Towards integrated microliquid handling systems," *Journal of Micromechanics and Microengineering*, vol. 4, no. 4, pp. 227–245, 1994.

[19] H. Becker and L. E. Locascio, "Polymer microfluidic devices," *Talanta*, vol. 56, no. 2, pp. 267 – 287, 2002.

[20] D. C. Duffy, J. C. McDonald, O. J. Schueller, and G. M. Whitesides, "Rapid prototyping of microfluidic systems in poly(dimethylsiloxane)," *Analytical Chemistry*, vol. 70, no. 23, pp. 4974–4984, 1998.

[21] M. Alonso-Amigo, "Polymer microfabrication for microarrays, microreactors and microfluidics," *Journal of the Association for Laboratory Automation*, vol. 5, no. 6, pp. 96–101, 2000.

[22] O. Geschke, H. Klank, and P. Tellemann, *Microsystem Engineering of Lab-on-a-Chip Devices*. Wiley-VCH, 2004.

[23] B. Li, Q. Chen, D.-G. Lee, J. Woolman, and G. Carman, "Development of large flow rate, robust, passive micro check valves for compact piezoelectrically actuated pumps," *Sensors and Actuators A: Physical*, vol. 117, no. 2, pp. 325–330, 2005.

[24] D. Bien, S. Mitchell, and H. Gamble, "Fabrication and characterization of a micromachined passive valve," *Journal of Micromechanics and Microengineering*, vol. 13, no. 5, pp. 557–562, 2003.

[25] M. Hu, H. Du, S.-F. Ling, Y. Fu, Q. Chen, L. Chow, and B. Li, "A silicon-on-insulator based micro check valve," *Journal of Micromechanics and Microengineering*, vol. 14, no. 3, pp. 382–387, 2004.

[26] N.-T. Nguyen, T.-Q. Truong, K.-K. Wong, S.-S. Ho, and C. Lee-Ngo Low, "Micro check valves for integration into polymeric microfluidic devices," *Journal of Micromechanics and Microengineering*, vol. 14, no. 1, pp. 69–75, 2004.

[27] G.-H. Feng and E. S. Kim, "Micropump based on pzt unimorph and one-way parylene valves," *Journal of Micromechanics and Microengineering*, vol. 14, no. 4, pp. 429–435, 2004.

[28] T.-Q. Truong and N.-T. Nguyen, "A polymeric piezoelectric micropump based on lamination technology," *Journal of Micromechanics and Microengineering*, vol. 14, no. 4, pp. 632–638, 2004.

[29] M. Carrozza, N. Croce, B. Magnani, and P. Dario, "A piezoelectric-driven stereolithography-fabricated micropump," *Journal of Micromechanics and Microengineering*, vol. 5, no. 2, pp. 177–9, 1995.

[30] E. F. J. Hasselbrink, T. J. Shepodd, and J. E. Rehm, "High-pressure microfluidic control in lab-on-a-chip devices using mobile polymer monoliths," *Analytical Chemistry - Columbus*, vol. 74, no. 19, pp. 4913–4918, 2002.

[31] B. J. Kirby, D. S. Reichmuth, R. F. Renzi, T. J. Shepodd, and B. J. Wiedenman, "Microfluidic routing of aqueous and organic flows at high pressures: fabrication and characterization of integrated polymer microvalve elements," *Lab on a Chip*, vol. 5, no. 2, pp. 184–190, 2005.

[32] W. Schomburg, R. Ahrens, W. Bacher, C. Goll, S. Meinzer, and A. Quinte, "Amanda - low-cost production of microfluidic devices," *Sensors and Actuators A: Physical*, vol. 70, no. 1-2, pp. 153–158, 1998.

[33] T. Rogge, Z. Rummler, and W. K. Schomburg, "Polymer micro valve with a hydraulic piezo-drive fabricated by the amanda process," *Sensors and Actuators, A: Physical*, vol. 110, no. 1, pp. 206–212, 2004.

[34] S. Bohm and P. Bergveld, "A plastic micropump constructed with conventional techniques and materials," *Sensors and Actuators A: Physical*, vol. 77, no. 3, pp. 223–228, 1999.

[35] S. Santra, P. Holloway, and C. D. Batich, "Fabrication and testing of a magnetically actuated micropump," *Sensors and Actuators B: Chemical*, vol. 87, no. 2, pp. 358–364, 2002.

[36] L. Tian, W. Wang, X. Liu, X. Wang, and Z. Bao, "The pdms micro valve driven by pzt piezoelectric actuator on the silicon wafer," *MEMS, MOEMS, and Micromachining II and Proceedings of SPIE - The International Society for Optical Engineering*, vol. 6186, 2006.

[37] W. C. Young and R. G. Budynas, *Roark's Formulas For Stress and Strain.* McGraw-Hill, 7th ed., 2002.

[38] N. Tas, T. Lammerink, J. Berenschot, M. Elwenspoek, and A. Van Den Berg, "Scaling behaviour of pressure-driven micro-hydraulic systems," *2002 International Conference on Modeling and Simulation of Microsystems - MSM 2002 and 2002 International Conference on Modeling and Simulation of Microsystems - MSM 2002*, pp. 174–177, 2002.

[39] J. N. Lee, C. Park, and G. M. Whitesides, "Solvent compatibility of poly(dimethylsiloxane)-based microfluidic devices," *Analytical Chemistry*, vol. 75, no. 23, pp. 6544–6554, 2003.

[40] N.-T. Nguyen and T.-Q. Truong, "A fully polymeric micropump with piezoelectric actuator," *Sensors and Actuators B: Chemical*, vol. 97, no. 1, pp. 137–143, 2004.

[41] E. Meng, X.-Q. Wang, H. Mak, and Y.-C. Tai, "A check-valved silicone diaphragm pump," *Micro Electro Mechanical Systems, 2000. MEMS 2000. The Thirteenth Annual International Conference on*, pp. 62 –67, 2000.

[42] C. Schabmueller, M. Koch, M. Mokhtari, A. Evans, A. Brunnschweiler, and H. Sehr, "Self-aligning gas/liquid micropump," *Journal of Micromechanics and Microengineering*, vol. 12, no. 4, pp. 420–424, 2002.

[43] K.-P. Kamper, J. Dopper, W. Ehrfeld, and S. Oberbeck, "A self-filling low-cost membrane micropump," *Micro Electro Mechanical Systems, 1998. MEMS 98. Proceedings., The Eleventh Annual International Workshop on*, pp. 432 –437, 1998.

[44] J. Schonfeld, "Analogy of hydraulic, mechanical, acoustic and electric systems," *Applied Scientific Research, Section B (Electrophysics, Acoustics, Optics, Mathematical Methods)*, vol. 3, no. 6, 1954.

[45] M. Richter, R. Linnemann, and P. Woias, "Robust design of gas and liquid micropumps," *Sensors and Actuators A: Physical*, vol. 68, no. 1-3, pp. 480–486, 1998.

[46] R. Zengerle and M. Richter, "Simulation of microfluid systems," *Journal of Micromechanics and Microengineering*, vol. 4, no. 4, pp. 192–204, 1994.

[47] T. Gerlach, M. Schuenemann, and H. Wurmus, "A new micropump principle of the reciprocating type using pyramidic micro flowchannels as passive valves," *Journal of Micromechanics and Microengineering*, vol. 5, no. 2, pp. 199–201, 1995.

[48] T. Bourouina and J.-P. Grandchamp, "Modeling micropumps with electrical equivalent networks," *Journal of Micromechanics and Microengineering*, vol. 6, no. 4, pp. 398–404, 1996.

[49] H. S. Khoo, K.-K. Liu, and F.-G. Tseng, "Characterization of the mechanical properties of microscale elastomeric membranes," *Measurement Science and Technology*, vol. 16, no. 3, pp. 653–658, 2005.

[50] M. Unger, H.-P. Chou, T. Thorsen, A. Scherer, and S. Queke, "Monolithic microfabricated valves and pumps by multilayer soft lithography," *Science*, vol. 288, no. 5463, pp. 113–116, 2000.

[51] J. Y. Baek, J. Y. Park, J. I. Ju, T. S. Lee, and S. H. Lee, "A pneumatically controllable flexible and polymeric microfluidic valve fabricated via in situ development," *Journal of Micromechanics and Microengineering*, vol. 15, no. 5, pp. 1015–1020, 2005.

[52] O. Ohman and H. Elderstig, "A pneumatically actuated micro valve with a silicone rubber membrane for integration with fluid-handling systems," *Solid-State Sensors and Actuators, 1995 and Eurosensors IX.. Transducers '95. The 8th International Conference on*, vol. 2, pp. 284 –286, 1995.

[53] A. Young, T. Bloomstein, and S. Palmacci, "Contoured elastic-membrane microvalves for microfluidic network integration," *Journal of Biomechanical Engineering, Transactions of the ASME*, vol. 121, no. 1, pp. 2–6, 1999.

[54] D. Sadler, T. Liakopoulos, J. Cropp, C. Ahn, and H. Henderson, "Prototype microvalve using a new magnetic microactuator," *Proceedings of SPIE - The International Society for Optical Engineering*, vol. 3515, pp. 46–52, 1998.

[55] C. Goll, W. Bacher, B. Bustgens, D. Maas, R. Ruprecht, and W. Schomburg, "An electrostatically actuated polymer microvalve equipped with a movable membrane electrode," *Journal of Micromechanics and Microengineering*, vol. 7, no. 3, pp. 224–6, 1997.

[56] V. Namasivayam, R. H. Liu, B. Towe, and P. Grodzinski, "Design of a self-contained 3d microvalve in pdms," in *Transducers Eurosensors XV*, 2001.

[57] T. Rogge, Z. Rummler, and W. Schomburg, "Polymer micro valve with a hydraulic piezo-drive fabricated by the amanda process," *Sensors and Actuators A: Physical*, vol. 110, no. 1-3, pp. 206–212, 2004.

[58] P. Gravesen, J. Branebjerg, and O. Jensen, "Microfluidics-a review," *Journal of Micromechanics and Microengineering*, vol. 3, no. 4, pp. 168–82, 1993.

[59] F. Pedrotti and L. Pedrotti, "Introduction to optics," 1993.

[60] R. Jenny, "Fundamentals of fiber optics,"

[61] A. W. Snyder and J. D. Love, "Optical waveguide theory," *Institute of Advanced Studies, Australian National University*, 1991.

[62] K. B. Mogensen, J. El-Ali, A. Wolff, and J. P. Kutter, "Integration of polymer waveguides for optical detection in microfabricated chemical analysis systems," *Applied Optics*, vol. 42, no. 19, pp. 4072–4079, 2003.

[63] E. Verpoorte, A. Manz, H. Ludi, A. Bruno, F. Maystre, B. Krattiger, H. Widmer, B. van der Schoot, and N. de Rooij, "A silicon flow cell for optical detection in miniaturized total chemical analysis systems," *Sensors and Actuators B (Chemical)*, vol. B6, no. 1-3, pp. 66–70, 1992.

[64] G. W. Ewing, *Instrumental Methods of Chemical Analysis*. McGraw-Hill, fifth ed., 1985.

[65] P. S. Jensen, J. Bak, and S. Andersson-Engels, "Influence of temperature on water and aqueous glucose absorption spectra in the near- and mid-infrared regions at physiologically relevant temperatures," *Applied Spectroscopy*, vol. 57, no. 1, pp. 28–36, 2003.

[66] S. Y. Venyaminov and F. G. Prendergast, "Water (H_2O and D_2O) molar absorptivity in the 1000-4000 cm^{-1} range and quantitative infrared spectroscopy of aqueous solutions," *Analytical Biochemistry*, vol. 248, no. 2, pp. 234–245, 1997.

[67] K. B. Mogensen, J. El-Ali, A. Wolff, and J. P. Kutter, "Integration of polymer waveguides for optical detection in microfabricated chemical analysis systems," *Applied Optics*, vol. 42, no. 19, pp. 4072–4079, 2003.

[68] Micro-Chem, 1254 Chestnut Street, Newton, MA 02464, *Nano SU-8 2000 Negative Tone Photoresists Formulations 25-75*, 2000.

[69] Z. Wang, J. El-Ali, M. Engelund, T. Gotsæd, I. R. Perch-Nielsen, K. B. Mogensen, D. Snakenborg, J. P. Kutter, and A. Wolff, "Measurements of scattered light on a microchip flow cytometer with integrated polymer based optical elements," *Lab on a chip*, vol. 4, 2004. Advance article.

[70] K. B. Mogensen, H. Klank, and J. P. Kutter, "Recent developments in detection for microfluidic systems," *Electrophoresis - An International Journal*, vol. 25, no. 21, pp. 3498–3512, 2004.

[71] S. Krawczyk, "Discussion on optical integration in lab-on-a-chip microsystems for medical diagnostics," *Physica Status Solidi C*, vol. 0, no. 3, pp. 998–1012, 2003.

[72] K. B. Mogensen, N. J. Petersen, J. Hübner, and J. P. Kutter, "Monolithic integration of optical waveguides for absorbance detection in microfabricated electrophoresis devices," *Electrophoresis*, vol. 22, pp. 3930–3938, 2001.

[73] O. Rötting, W. Röpke, H. Becker, and C. Gärtner, "Polymer microfabrication technologies," *Microsystem Technologies*, vol. 8, no. 1, pp. 32–36, 2002.

[74] V. Piotter, N. Holstein, K. Plewa, R. Ruprecht, and J. Hausselt, "Replication of micro components by different variants of injection molding," *Microsystem Technologies*, vol. 10, no. 6-7, pp. 547–551, 2004.

[75] L. J. Kricka, P. Fortina, N. J. Panaro, P. Wilding, G. Alonso-Amigo, and H. Becker, "Fabrication of plastic microchips by hot embossing," *Lab on a Chip*, vol. 2, no. 1, pp. 1–4, 2002.

[76] L. Martynova, L. E. Locascio, M. Gaitan, G. W. Kramer, R. G. Christensen, and W. A. MacCrehan, "Fabrication of plastic microfluid channels by imprinting methods," *Analytical Chemistry*, vol. 69, pp. 4783–4790, 1997.

[77] A. Guber, M. Heckele, D. Herrmann, A. Muslija, V. Saile, L. Eichhorn, T. Gietzelt, W. Hoffmann, P. Hauser, J. Tanyanyiwa, A. Gerlach, N. Gottschlich, and G. Knebel, "Microfluidic lab-on-a-chip systems based on polymers-fabrication and application," *Chemical Engineering Journal*, vol. 101, no. 1-3, pp. 447–453, 2004.

[78] H. Becker and U. Heim, "Silicon as tool material for polymer hot embossing," *Micro Electro Mechanical Systems, 1999. MEMS '99. Twelfth IEEE International Conference on*, pp. 228 –231, 1999.

[79] H. Becker and C. Gartner, "Polymer based micro-reactors," *Reviews in Molecular Biotechnology*, vol. 82, no. 2, pp. 89–99, 2001.

[80] K. B. Mogensen, J. El-Ali, A. Wolff, and J. P. Kutter, "Integration of polymer waveguides for optical detection in microfabricated chemical analysis systems," *Applied Optics*, vol. 42, pp. 4072–4079, 2003.

[81] Z. Wang, J. El-Ali, M. Engelund, T. Gotsaed, I. R. Perch-Nielsen, K. B. Mogensen, D. Snakenborg, J. P. Kutter, and A. Wolff, "Measurements of scattered light on a microchip flow cytometer with integrated polymer based optical elements," *Lab on a Chip*, vol. 4, no. 4, pp. 372–377, 2004.

[82] J. Ruano, M. Aguirregabiria, M. Tijero, M. Arroyo, J. Garcia, J. Berganzo, I. Aramburu, F. Blanco, and K. Mayora, "Monolithic integration of microfluidic channels and optical waveguides using a photodefinable epoxy," *Micro Electro Mechanical Systems, 2004. 17th IEEE International Conference on. (MEMS)*, pp. 121–124, 2004.

[83] C.-H. Lin, G.-B. Lee, S.-H. Chen, and G.-L. Chang, "Micro capillary electrophoresis chips integrated with buried su-8/sog optical waveguides for bio-analytical applications," *Sensors and Actuators A: Physical*, vol. 107, no. 2, pp. 125–131, 2003.

[84] Q. Kou, I. Yesilyurt, V. Studer, M. Belotti, E. Cambril, and Y. Chen, "On-chip optical components and microfluidic systems," *Microelectronic Engineering*, vol. 73-74, pp. 876–880, 2004.

[85] O. J. Schueller, X.-M. Zhao, G. M. Whitesides, S. P. Smith, and M. Prentiss, "Fabrication of liquid-core waveguides by soft lithography," *Advanced Materials*, vol. 11, no. 1, pp. 37–41, 1999.

[86] D. Snakenborg, H. Klank, and J. Kutter, "Microstructure fabrication with a CO_2 laser system," *Journal of Micromechanics and Microengineering*, vol. 14, no. 2, pp. 182–9, 2004.

[87] A. Rainelli, R. Stratz, K. Schweizer, and P. Hauser, "Miniature flow-injection analysis manifold created by micromilling," *Talanta*, vol. 61, no. 5, pp. 659 – 665, 2003.

[88] M. Takacs, B. Vero, and I. Meszaros, "Micromilling of metallic materials," *Journal of Materials Processing Technology*, vol. 138, no. 1-3, pp. 152–155, 2003.

[89] X.-M. Zhao, S. Smith, M. Prentiss, and G. Whitesides, "Fabrication of waveguide couplers using microtransfer molding," *Lasers and Electro-Optics, 1997. CLEO '97., Summaries of Papers Presented at the Conference on*, vol. 11, pp. 22 –23, 1997.

[90] V. Ramaswamy and H. Weber, "Low-loss polymer films with adjustable refractive index," *Applied Optics*, vol. 12, no. 7, pp. 1581–3, 1973.

[91] B. E. A. Saleh and M. C. Teich, *Fundamentals of Photonics.* John Wiley & Sons, 1991.

[92] D. Stadnik, D. Snakenborg, J. P. Kutter, and A. Dybko, "Micromilling as a fabrication method for miniaturized analytical systems," in *9-th Scientific Conference, Optoelectronic and Electronic Sensors COE*, 2006.

[93] S. Weichel, R. De Reus, and M. Lindahl, "Silicon-to-silicon wafer bonding using evaporated glass," *Sensors and Actuators A: Physical*, vol. 70, no. 1-2, pp. 179–184, 1998.

[94] M. Despont, H. Gross, F. Arrouy, C. Stebler, and U. Staufer, "Fabrication of a silicon-pyrex-silicon stack by a.c. anodic bonding," *Sensors and Actuators A: Physical*, vol. 55, no. 2-3, pp. 219–224, 1996.

[95] A. Berthold, L. Nicola, P. Sarro, and M. Vellekoop, "Glass-to-glass anodic bonding with standard ic technology thin films as intermediate layers," *Sensors and Actuators A: Physical*, vol. 82, no. 1-3, pp. 224–228, 2000.

[96] J. Oberhammer, F. Niklaus, and G. Stemme, "Sealing of adhesive bonded devices on wafer level," *Sensors and Actuators A: Physical*, vol. 110, no. 1-3, pp. 407–412, 2004.

[97] F. Niklaus, H. Andersson, P. Enoksson, and G. Stemme, "Low temperature full wafer adhesive bonding of structured wafers," *Sensors and Actuators A: Physical*, vol. 92, no. 1-3, pp. 235–241, 2001.

[98] S. Satyanarayana, R. Karnik, and A. Majumdar, "Stamp-and-stick room-temperature bonding technique for microdevices," *Microelectromechanical Systems, Journal of*, vol. 14, no. 2, pp. 392–399, 2005.

[99] L. Song, T. Liu, D. Liang, D. Fang, and B. Chu, "Editorial - separation of double-stranded dna fragments by capillary electrophoresis in interpenetrating networks of polyacrylamide and polyvinylpyrrolidone," *Electrophoresis - An International Journal*, vol. 22, no. 17, pp. 3688–3698, 2001.

[100] R. M. McCormick, R. J. Nelson, M. Goretty Alonso-Amigo, D. J. Benvegnu, and H. H. Hooper, "Microchannel electrophoretic separations of dna in injection-molded plastic substrates," *Analytical Chemistry - Columbus*, vol. 69, no. 14, pp. 2626–2630, 1997.

[101] L. Brown, T. Koerner, J. H. Horton, and R. D. Oleschuk, "Fabrication and characterization of poly(methylmethacrylate) microfluidic devices bonded using surface modifications and solvents," *Lab on a Chip*, vol. 6, no. 1, pp. 66–73, 2006.

[102] L. J. Kricka, P. Fortina, N. J. Panaro, P. Wilding, G. Alonso-Amigo, and H. Becker, "Fabrication of plastic microchips by hot embossing," *Lab on a Chip*, vol. 2, no. 1, pp. 1–4, 2002.

[103] J. Lai, X. Chen, X. Wang, X. Yi, and S. Liu, "Laser bonding and packaging of plastic microfluidic chips," *Electronic Packaging Technology Proceedings, 2003. ICEPT2003. Fifth International Conference on*, pp. 168–171, 2003.

[104] K. F. Lei, W. J. Li, N. Budraa, and J. Mai, "Microwave bonding of polymer-based substrates for micro/nano fluidic applications," *TRANSDUCERS, Solid-State Sensors, Actuators and Microsystems, 12th Innational Conference on, 2003*, vol. 2, pp. 1335–1338, 2003.

[105] J. Li and D. Chen, "Low-temperature thermal bonding of pmma microfluidic chips," *Analytical Letters*, vol. 38, pp. 1127–1136, 2005.

[106] G. A. C. M. Spierings and J. Haisma, "Direct bonding of organic materials," *Applied Physics Letters*, vol. 64, no. 24, pp. 3246–3248, 1994.

[107] J. Haisma, G. A. C. M. Spierings, T. M. Michelsen, and C. L. Adema, "Surface preparation and phenomenological aspects of direct bonding," *Philips J. Res.*, vol. 49, pp. 23–46, 1995.

[108] J. Haisma, G. A. Spierings, and T. M. Michielsen, "Frameworks for direct bonding," *Philips Journal of Research*, vol. 49, no. 1-2, pp. 11–21, 1995.

[109] J. Haisma and G. Spierings, "Contact bonding, including direct-bonding in a historical and recent context of materials science and technology, physics and chemistry historical review in a broader scope and comparative outlook," *Materials Science and Engineering: R: Reports*, vol. R37, no. 1-2, pp. 1–60, 2002.

[110] T. Velten, H. Ruf, D. Barrow, N. Aspragathos, P. Lazarou, E. Jung, C. Malek, M. Richter, J. Kruckow, and M. Wackerle, "Packaging of bio-MEMS: strategies, technologies, and applications," *Advanced Packaging, IEEE Transactions on*, vol. 28, no. 4, pp. 533–546, 2005.

[111] Y. Yang, C. Li, J. Kameoka, K. H. Lee, and H. G. Craighead, "A polymeric microchip with integrated tips and in situ polymerized mono-

lith for electrospray mass spectrometry," *Lab on a Chip*, vol. 5, no. 8, pp. 869–876, 2005.

[112] G. Y. Choi, J. F. Kang, A. Ulman, W. Zurawsky, and C. Fleischer, "Acid-base interaction in the adhesion between two solid surfaces," *Langmuir*, vol. 15, no. 26, pp. 8783–8786, 1999.

[113] Z. Wu, N. Xanthopoulos, F. Reymond, J. S. Rossier, and H. H. Girault, "Editorial - polymer microchips bonded by o2-plasma activation," *Electrophoresis - An International Journal*, vol. 23, no. 5, pp. 782–790, 2002.

[114] B.-H. Jo, L. Van Lerberghe, K. Motsegood, and D. Beebe, "Three-dimensional micro-channel fabrication in polydimethylsiloxane (pdms) elastomer," *Microelectromechanical Systems, Journal of*, vol. 9, no. 1, pp. 76 –81, 2000.

[115] A. Y. N. Hui, G. Wang, B. Lin, and W.-T. Chan, "Microwave plasma treatment of polymer surface for irreversible sealing of microfluidic devices," *Lab on a Chip*, vol. 5, no. 10, pp. 1173–1177, 2005.

[116] J. Kim and M. Chaudhury, "Corona-discharge-induced hydrophobicity loss and recovery of silicones," *Electrical Insulation and Dielectric Phenomena, 1999 Annual Report Conference on*, vol. 2, pp. 703 –706 vol.2, 1999.

[117] C. K. Fredrickson and Z. H. Fan, "Macro-to-micro interfaces for microfluidic devices," *Lab on a Chip*, vol. 4, no. 6, pp. 526–533, 2004.

[118] B. Gray, N. Mourlas, K. Williams, and G. Kovacs, "Novel interconnection technologies for integrated microfluidic systems," *Sensors and Actuators A: Physical*, vol. 77, no. 1, pp. 57–65, 1999.

[119] E. Meng, S. Wu, and Y.-C. Tai, "Silicon couplers for microfluidic applications," *Fresenius' Journal of Analytical Chemistry*, vol. 371, no. 2, pp. 270–275, 2001.

[120] N. H. Bings, C. Wang, C. D. Skinner, C. L. Colyer, P. Thibault, and D. J. Harrison, "Microfluidic devices connected to fused-silica capillaries with minimal dead volume," *Analytical Chemistry - Columbus*, vol. 71, no. 15, pp. 3292–3296, 1999.

[121] A. Puntambekar and C. H. Ahn, "Self-aligning microfluidic interconnects for glass- and plastic-based microfluidic systems," *Journal of Micromechanics and Microengineering*, vol. 12, no. 1, pp. 35–40, 2002.

[122] V. Nittis, R. Fortt, C. H. Legge, and A. J. de Mello, "A high-pressure interconnect for chemical microsystem applications," *Lab on a Chip*, vol. 1, no. 2, pp. 148–152, 2001.

[123] G. Perozziello, M. F. Jensen, J. E. McCormack, F. Bundgaard, and O. Geschke, "Plug'n pump fluidic interconnection," in *Proceedings of μTAS*, vol. 2, pp. 575–577, RSC, 2004.

[124] D. Snakenborg, "Filling unit for flat microstructure," *German patent, pat.no. DE10140633-A1*, 2003.

[125] Z. Yang and R. Maeda, "A world-to-chip socket for microfluidic prototype development," *Electrophoresis*, vol. 23, no. 20, pp. 3474–8, 2002.

[126] M. G. Clarey, J. P. Erzberger, P. Grob, A. E. Leschziner, J. M. Berger, E. Nogales, and M. Botchan, "Nucleotide-dependent conformational changes in the dnaa-like core of the origin recognition complex," *Nature Structural and Molecular Biology*, vol. 13, no. 8, pp. 684–690, 2006.

[127] K. Lindorff-Larsen, R. B. Best, M. A. DePristo, C. M. Dobson, and M. Vendruscolo, "Simultaneous determination of protein structure and dynamics," *Nature*, vol. 433, no. 7022, pp. 128–132, 2005.

[128] L. Pollack, M. W. Tate, N. C. Darnton, J. B. Knight, S. M. Gruner, W. A. Eaton, and R. H. Austin, "Biological sciences - biophysics - compactness of the denatured state of a fast-folding protein measured by submillisecond small-angle x-ray scattering," *Proceedings of the National Academy of Sciences of the USA*, vol. 96, no. 18, pp. 10115–10117, 1999.

[129] R. Barrett, J.-B. Salmon, M. Faucon, J. Lopez, G. Cristobal, F. Destremaut, A. Dodge, P. Guillot, P. Laval, and C. Masselon, "X-ray microfocussing combined with microfluidics for on-chip x-ray scattering measurements," *Lab on a Chip*, vol. 6, no. 4, pp. 494–499, 2006.